ANNUAL REVIEWS

Annual Review of Astronomy and Astrophysics

Spatially Resolved Spectroscopic Properties of Low-Redshift Star-Forming Galaxies

Sebastián F. Sánchez

Instituto de Astronomía, Universidad Nacional Autónoma de México, Ciudad Universitaria, C.P. 04510, México, D.F., Mexico; email: sfsanchez@astro.unam.mx

Annu. Rev. Astron. Astrophys. 2020. 58:99–155

First published as a Review in Advance on May 26, 2020

The *Annual Review of Astronomy and Astrophysics* is online at astro.annualreviews.org

https://doi.org/10.1146/annurev-astro-012120-013326

Keywords

galaxies: evolution, star formation, resolved properties, fundamental parameters, techniques: imaging spectroscopy

Abstract

I review the spatially resolved spectroscopic properties of low-redshift star-forming galaxies (and their retired counterparts) using results from the most recent optical integral field spectroscopy galaxy surveys. First, I briefly summarize the global spectroscopic properties of these galaxies, discussing the main ionization processes and the global relations described by the star-formation rates, gas-phase oxygen abundances, and average properties of their stellar populations (age and metallicity) in comparison with the stellar mass. Second, I present the local distribution of the ionizing processes down to kiloparsec scales, and I show how the global scaling relations found using integrated parameters (like the star-formation main sequence, mass–metallicity relation, and Schmidt–Kennicutt law) have local/resolved counterparts, with the global ones being, for the most part, just integrated/average versions of the local ones. I discuss the local/resolved star-formation histories (SFHs) and chemical-enrichment histories and their implications on the inside-out growth of galaxies. Third, I present the radial distributions of the surface densities of the properties explored globally and how they depend on the integrated galaxy properties.

In conclusion, I find that the evolution of galaxies is mostly governed by local processes but clearly affected by global ones:

- Many global scaling relations present resolved counterparts (verified down to kiloparsec scales) that can explain them as well as the observed radial gradients in galaxies.
- These relations are consequences of the local SFHs, the narrow range of the depletion times, and a local metal enrichment.
- Deviations from these relations are due to dynamical and mixing processes, local exchange of gas (inflows, outflows, and fountains), depletion time differences, and/or differences in the resolved SFHs.
- Ionization happens at local scales that may be driven by different physical processes, and it cannot be clearly understood using purely integrated quantities. The dominant ionization in galaxies has a stellar origin.

Contents

1. INTRODUCTION

The formation of stars from gas is one of the physical processes that contributes more deeply to shape our Universe. Without the ignition of the thermonuclear reactions that power stars, it would be impossible to conceive our physical world. There would be no chemical elements besides hydrogen and helium (and traces of lithium), no complex chemical compounds, no rocky planets, and no life. Therefore, the study of the conditions required to form stars is of key importance to understanding our existence. The birth of stars is governed by detailed physical laws, and given some particular conditions of gas density, pressure, and metallicity, their ignition is triggered (e.g., Bonnell et al. 1998). However, when large stellar populations are considered ($M_* \sim 10^4$ $M_\odot$), star formation (SF) is regulated by statistical laws that correlate with the main observed properties, like the neutral gas density and the star-formation rate (SFR), averaged over hundreds of parsecs

or kiloparsecs scales across the galaxies (e.g., Kennicutt 1998b). In this context it is relevant to understand whether these laws are the same for all galaxy types or depend on either local (kiloparsec scales or the scale of molecular clouds) or global properties of the galaxies in which SF happens.

All galaxies formed stars in early cosmological times, and in general the SFR was higher in the past both in individual galaxies (e.g., Heavens et al. 2004, Speagle et al. 2014) and averaged over the entire population (e.g., Madau & Dickinson 2014). However, at low redshift and at least up to $z \sim 1$, galaxies present a clear bimodality regarding their SFRs: (*a*) those that are more actively forming stars [defined broadly as star-forming galaxies (SFGs)], and (*b*) those that present little or no star-forming activity [defined broadly as passive, quenched, or retired galaxies (RGs); e.g., Stasińska et al. (2008)]. These two groups are well separated in different diagrams that compare either the current SFR or proxies of the age of the stellar population with the integrated stellar mass or absolute magnitude, like the SFR versus mass diagram (SFR–M_*, e.g., Renzini & Peng 2015), the color–magnitude diagram (e.g., Bell et al. 2004), or the D4000–mass diagram (e.g., Blanton & Moustakas 2009; where D4000 is an age tracer). In addition, this bimodality is strongly correlated with the morphological, structural, and dynamical properties of the galaxies (e.g., Drory & Fisher 2007, Blanton & Moustakas 2009, Graham et al. 2018). In general, SFGs are late-type galaxies (LTGs) and disk dominated (e.g., Brinchmann et al. 2004), whereas RGs are usually early type and bulge dominated (e.g., Drory & Fisher 2007). Additionally, we know that the masses of early-type galaxies at low redshift have grown by at least a factor of two in the past ∼8 Gyr (e.g., Bell et al. 2006); however, they show little or no significant SF during the same time period (e.g., López Fernández et al. 2018, Sánchez et al. 2019a). This implies that there should be a population of galaxies transitioning from SFGs to RGs. This event may last only a few gigayears, and it involves profound morphological and structural transformation of those galaxies, as well as dramatic aging of their average stellar populations. Broadly speaking, this process is known as quenching or rapid halting of SF activity (e.g., Casado et al. 2015, Saintonge et al. 2016). Beside that dramatic process, current SFGs have steadily decreased their SFRs along the same time period, showing slightly older stellar populations on average—it is a smooth process generally known as aging (e.g., Casado et al. 2015).

Our understanding of nearby galaxies and their evolution has deeply improved since the advent of large imaging surveys with the addition of single-fiber spectroscopy for a lower number of objects [e.g., Sloan Digital Sky Survey (SDSS), York et al. (2000); Galaxy and Mass Assembly survey (GAMA), Driver et al. (2009)]. These surveys provide us with multiband imaging and photometry of millions of galaxies and spectroscopy for hundreds of thousands of them. The main results produced by these massive data sets were reviewed by Blanton & Moustakas (2009), who described in detail the physical properties of these galaxies, including their global distributions in luminosity, stellar population, and molecular and atomic gas and their corresponding mass/luminosity functions, for different environments. Despite the huge amount of information and the step forward introduced by these surveys, they posed a severe limitation: They do not provide resolved spectroscopic information. Galaxies have long been known to be spatially extended objects, with observed properties that vary across their optical extent (e.g., Hubble 1926, 1936). Many of these properties vary systematically as a function of position relative to the galaxy center, and radial gradients have been studied for decades in both the gas and stellar population content (e.g., Pagel & Edmunds 1981, Peletier 1989). Therefore, characterizing galaxies by single-aperture spectra or spatially resolved multiband photometry imposes severe limitations in both describing their properties and understanding the evolution that shaped them.

This is particularly important in (*a*) the study of the variation of the physical properties of the interstellar medium (ISM), (*b*) the detailed understanding of the composition of the

Star forming galaxies (SFGs): galaxies that are more actively forming stars

Retired galaxies (RGs): galaxies that present little or no star-forming activity

Interstellar medium (ISM): gas and dust within a galaxy distributed among and beyond stars

stellar populations across the optical extension of galaxies, and (*c*) the analysis of the kinematic properties and dynamical state of galaxies. Properly addressing these issues requires spatially resolved spectroscopic information that includes a substantial fraction of the optical extension of galaxies for a large, well-defined, statistically significant sample that covers the widest range of galaxy populations in different properties (e.g., masses, colors, morphologies, etc.). The advent of wide-field and multiplexed integral field units (IFUs) in the past decade has allowed us to perform these studies in an efficient way, making it possible to observe large samples of galaxies and leading to the first generation of optical integral field spectroscopy (IFS) galaxy surveys (IFS-GSs).

Integral field units (IFUs): a device attached to a spectrograph that allows for obtaining several spectra simultaneously of different contiguous locations in the sky

Integral field spectroscopy (IFS): technique that allows obtaining spectra using an IFU

Integral Field Spectroscopy Galaxy Surveys (IFS-GSs): large program to acquire IFS data over a well-defined and statistically representative sample of galaxies

Effective radius (R_e): galactocentric distance at which half of the total flux intensity of a galaxy in a certain photometric band is encircled

In this review, I summarize our current knowledge of the spatially resolved spectroscopic properties of low-redshift galaxies on the basis of the results of the most recent IFS-GS. I focus on SFGs, although I also present the properties of their retired counterparts, as a necessity to discuss our knowledge about what triggers and halts SF. This review is therefore focused on the cycle of birth, evolution, and death of stars from a statistical point of view. I summarize the main results on the distributions of stellar populations and properties of the ionized ISM and their interconnections. First, I present the main global properties of galaxies and focus on those aspects to later present the spatial distributions of the same properties. Finally, I present the local scaling laws that we think rule the SF and enrichment processes in galaxies. I do not address in this review the morphological and photometric properties of galaxies or any results that could be derived using only photometric or integrated spectroscopic data (see Blanton & Moustakas 2009 for a review on the topic). The kinematic properties and the dynamical stage of galaxies are also not addressed (see Cappellari 2016 for a review on this topic). For a more detailed exploration of the emission-line properties of galaxies, I refer the reader to the recent review by Kewley et al. (2019).

2. DATA

The results shown in this review are extracted from the most recently published analysis on IFS-GS data. Instead of using published figures, I recreate the results based on a compilation of IFS data sets that combine data from four different surveys: AMUSING++ (Galbany et al. 2016), CALIFA (Sánchez et al. 2012a), MaNGA (Bundy et al. 2015), and SAMI (Croom et al. 2012). It is beyond the scope of this article to review in detail the different IFS-GSs. Nevertheless, I present a summary of their properties in Appendix A, describing the number of galaxies sampled by each survey and the differences in spatial and spectral resolution. Despite the big differences in the nature of these surveys, particularly in terms of the covered area for the sampled galaxies and the spatial and spectral resolution, all of them provide spatially resolved spectroscopic information for statistically significant and large samples of galaxies mostly located at $z \sim 0.01$–0.06. All together, the adopted compilation comprises 8,177 galaxies. That is, so far, the largest compilation of IFS data. A summary of the properties of this compilation is included in Appendix A and distributed in **Supplemental Figures 1–8**.[1]

Supplemental Material >

In this review, I use this full sample to describe global properties when required. To present the spatially resolved or radial properties, I selected a subset of this sample comprising only those galaxies/datacubes having stellar masses within 10^6–10^{13} $M_\odot$ and redshift ranges of $0.005 < z < 0.05$ and fulfilling the following criteria: (*a*) the IFS data cover at least 1.5 R_e of the galaxy; (*b*) the galaxy is well resolved [meaning the effective radius (R_e) is larger than 5 arcsec, since most of the IFS-GSs have a typical spatial resolution of FWHM $\sim$ 2.5 arcsec]; (*c*) the galaxy is not highly

[1]Materials in addition to **Supplemental Figures 1–8** are also available at **http://ifs.astroscu.unam.mx/ARAA/**.

inclined (i.e., ellipticity, $\epsilon < 0.75$); and (*d*) the field of view (FoV) of the IFS data covers at least 25 arcsec projected in the sky (i.e., sampling at least 2.5 R_e). This subsample comprises 1,494 galaxies with the best compromise between spatial resolution and sampled IFS data (the sharing among the considered IFS-GSs is listed in **Table 1**). To homogenize the data set as much as possible, I make use of the data products provided by the same analysis pipeline, `Pipe3D` (Sánchez et al. 2016a,b). This pipeline extracts the main spectroscopic properties of the galaxies, integrated-, radial-, and spaxel-wise, including: (*a*) the composition and kinematic properties of the stellar population, providing the star-formation histories (SFH) and chemical-enrichment histories (ChEHs), and main average/integrated properties (stellar mass, age, [Z/H], dust attenuation),[2] together with the velocity and velocity dispersion; (*b*) the main properties of several emission lines within the considered wavelength range (flux, velocity, velocity dispersion, and equivalent width); (*c*) a set of high-order physical parameters, like the ISM oxygen abundance derived using different calibrators, the dust attenuation, estimations of molecular gas content, etc. Full details of the delivered products are provided in some recent articles [e.g., Ibarra-Medel et al. 2016, 2019; Sánchez et al. 2018]. `Pipe3D` is just one of the different pipeline/tools developed in recent years with the goal of analyzing IFS data (e.g., `PyCASSO`, `LZIFU`, `MaNGA DAP`; Ho et al. 2016, de Amorim et al. 2017, Belfiore et al. 2019b, respectively). In most cases, this pipeline produces the same or very similar results to those published in the reviewed articles (based in many cases on the tools listed above or similar ones). Cases of significant differences or lacking consensus are highlighted as much as possible.

Spaxel (spatial pixel): originally the spatial sampling element of an IFU or an IFS datacube

AGN (active galactic nucleus): a compact region in a galaxy's center powered by the gas accretion of a supermassive black hole, with a blue and hard ionizing spectrum

Post–asymptotic giant branch (post-AGB): low- and intermediate-mass stars in their final evolution period, going rapidly from the AGB toward the white dwarf phase

HOLMES (hot low-mass evolved stars): stars mostly in the post-AGB or white dwarf phase

3. GLOBAL PROPERTIES OF GALAXIES

Recent reviews dealing with the description of the current knowledge of the integrated/global properties of galaxies in the near Universe are based mostly on single-aperture spectroscopic data combined with broad-band imaging photometry (e.g., Blanton & Moustakas 2009). In this section, I summarize the main integrated properties and relations that are relevant for the main scope of this review, i.e., the local/resolved properties and relations.

3.1. What Ionizes Gas in Galaxies?

The ISM in galaxies is observed in the optical range by the emission lines produced by either recombination or radiative de-excitation of collisionally excited levels. To produce emission lines, the gas should be first ionized by high-energy photons (of at least 13.6 eV) emitted by either stars (young and old) or active galactic nuclei (AGNs; e.g., Osterbrock 1989), or generated by the energy dissipation in a shock front traveling through the ISM (e.g., Veilleux & Osterbrock 1987, Veilleux et al. 2005). All four different sources of ionization may be present in a single galaxy: (*a*) regions ionized by young OB stars residing in HII regions (Strömgren 1939), associated with star-forming areas (like spiral arms; e.g., Baldwin et al. 1981); (*b*) regions ionized by old stars, post-AGB stars, or HOLMES (e.g., Binette et al. 1994, Flores-Fajardo et al. 2011), associated with retired regions in galaxies (e.g., Singh et al. 2013, Gomes et al. 2016a); (*c*) AGN ionization, mostly concentrated in the central regions (e.g., Husemann et al. 2010, 2014; although the extension depends on the AGN luminosity); and (*d*) shock ionization, driven by either AGN or SF outflows (e.g., Heckman et al. 1990, Bland-Hawthorn 1995, López-Cobá et al. 2017b), or driven by low-density gas (e.g., Dopita et al. 1996, Kehrig et al. 2012, Cheung et al. 2016). Because the source of ionization is always local, and not global, it is always misleading to describe the ionized gas of a galaxy by

[2] A Salpeter (1955) IMF was also adopted here.

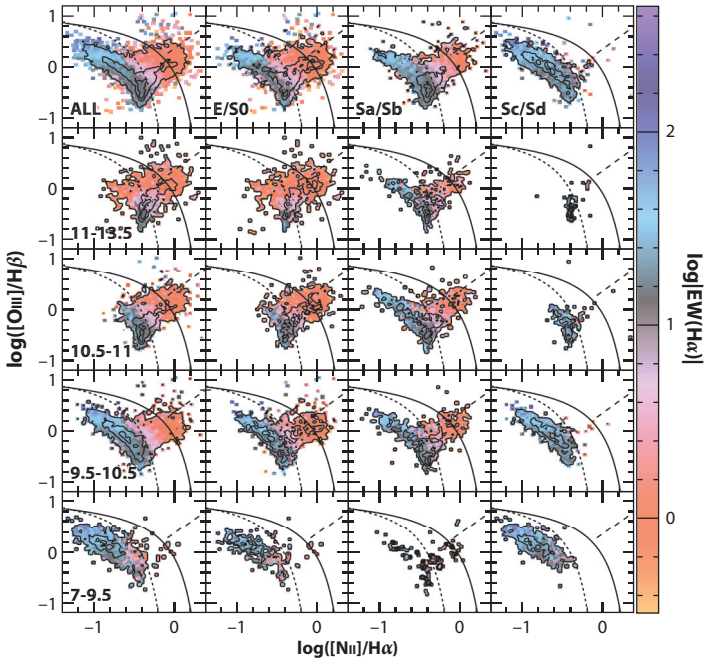

Figure 1

Distribution showing the classical [OIII]/Hβ versus [NII]/Hα diagnostic diagram, known as the BPT (Baldwin et al. 1981) diagram, where each of the 8,177 galaxies included in the adopted compilation contributes as a single point. Color-coding indicates the average equivalent width of Hα across the field of view of each datacube in decimal logarithm scale. Contours represent the density of galaxies, with contours indicating 95%, 50%, and 10% of the points. In all panels, the solid line represents the location of the Kewley et al. (2001) boundary line, with the separation between Seyferts and LINERs indicated by a dashed line. Finally, the dotted line represents the location of the Kauffmann et al. (2003) demarcation line. The full sample is shown in the upper-left panel, and subsequent panels show a subsample of galaxies segregated by morphology (from *left* to *right*) and stellar mass (from *top* to *bottom*), with the covered ranges labeled in the top- and left-most panels. Abbreviation: BPT, Baldwin–Phillips–Terlevich; LINERS, low-ionization nuclear emission-line regions.

average or integrated properties. A galaxy is never only an SFG, an RG, an AGN, or an outflow. A galaxy may present, locally, star-forming and/or post-AGB ionization, and it may host an AGN and exhibit outflows that are able to ionize the gas via shocks. Therefore, the classification for the source of ionization in a galaxy should be local and may require spatially resolved information of the emission-line diagnostics. Furthermore, as postulated by different authors (e.g., Stasińska et al. 2008, Cid Fernandes et al. 2010, Papaderos et al. 2013, Sánchez et al. 2014, Lacerda et al. 2018), classification may require some knowledge of the properties of the underlying stellar population and even the spatial distribution of the ionized gas structure (e.g., López-Cobá et al. 2019). Based on all those results, I present a practical scheme for classifying the ionization in Appendix B.

Figure 1 shows the BPT (Baldwin–Phillips–Terlevich; Baldwin et al. 1981) diagram for the global [OIII/Hβ] and [NII]/Hα line ratios, averaged along the entire FoV of the IFU data for each galaxy. The plot is color-coded by the average EW(Hα) [i.e., equivalent width (Hα)] of each galaxy. I present the distribution for the full compilation of galaxies adopted in this review, segregated by both mass and morphology in the different panels. Thus, each galaxy contributes as a single point in each panel, and it is characterized by a single pair of the considered line ratios (like in Kauffmann

et al. 2003). In addition, I include the classical demarcation lines that are usually adopted to classify the main ionizing processes (Kewley et al. 2001, Kauffmann et al. 2003). Line ratios on the left side of the figure, with high EW(Hα), are usually associated with ionization by young stars, and therefore are related to SF processes (HII regions). In contrast, the right side of the figure (above the considered demarcation lines) is associated with hard ionization that could be due to AGNs or shocks (high EWs) or ionization by old stars (e.g., post-AGBs, with low EWs).

Although it is clear that ionization has a local nature, there are clear trends between the global properties of galaxies (e.g., stellar mass, morphology, etc.) and the dominant ionizing source (e.g., Kauffmann et al. 2003). This is shown in **Figure 1**: More massive/early-type galaxies show a stronger contribution of ionization due to old stars, whereas less massive/later-type galaxies have a stronger presence of ionization due to young stars. This reflects the known evolution of galaxies, because more massive/early-type galaxies formed stars earlier in the cosmological time (e.g., Pérez-González et al. 2008, Thomas et al. 2010, González Delgado et al. 2014b), and therefore they have a larger fraction of old stars (e.g., González Delgado et al. 2016). Finally, AGNs are more frequently found in massive galaxies, either early-type galaxies (e.g., Kauffmann et al. 2003) or early spirals (e.g., Schawinski et al. 2010, Sánchez et al. 2018). A more detailed discussion on the ionization processes in galaxies and the use of emission lines to explore their evolution was recently presented by Kewley et al. (2019).

HII regions: gas clouds in the ISM ionized by individual or a cluster of young OB stars

Star-formation main sequence (SFMS): tight log-linear correlation between the integrated SFR and the M_* for SFGs

3.2. SFR–M_* Diagram and the Star-Formation Law

SFGs are those in which the main ionizing source is the vast presence of OB stars, directly connected with recent SF due to their short lifetimes (e.g., Pozzetti et al. 2010). On the contrary, RGs are those with a lack of ionized gas or with gas ionized by old stars and in which there is little (e.g., Gomes et al. 2016b) or no SF (e.g., Stasińska et al. 2008, Cid Fernandes et al. 2010). In general, there are no galaxies (or very few) where the ionization is dominated by shocks induced by outflows in the considered redshift range (e.g., López-Cobá et al. 2019). An interesting counterexample is the case of the filamentary or biconical ionized gas detected in weak AGNs and radio galaxies (already observed using narrow-band images in cD galaxies decades ago, e.g., M87; Jarvis 1990). Kehrig et al. (2012), using CALIFA data, first proposed that the ionization in these structures (and indeed across all the optical extensions of these galaxies) is dominated by shocks. Cheung et al. (2016) proposed them as a new type of objects (named red geysers), and their connection with radio sources was revisited recently by Roy et al. (2018). However, those galaxies comprise less than 4% of the total elliptical ones (i.e., less than 1% of the total galaxy population), as shown by López-Cobá et al. (2020). Finally, AGN ionization may dominate the integrated properties of the emission lines in galaxies, particularly at the central regions. Thus, some galaxies are classified as AGNs, although AGN hosts is a better term (e.g., Kauffmann et al. 2003).

When the SFR derived using the dust-corrected Hα luminosity of a galaxy (or any other SFR estimator like UV or FIR luminosities; e.g., Catalán-Torrecilla et al. 2015) is plotted along the stellar mass (M_*), the two populations of SFGs and RGs are clearly distinguished [and indeed well separated by the average value of the EW(Hα), with 3–6 Å being a clear boundary; e.g., Stasińska et al. 2008]. This is clearly demonstrated in **Figure 2**, where I present the SFR–M_* diagram for the galaxies in the current compilation.

The distribution of SFGs is well characterized by a log-linear, tight relation, observed between the SFR and M_*. This relation, known as the star-formation main sequence (SFMS) of galaxies, has been well studied using both single-aperture and IFS data at low redshift (e.g., Brinchmann et al. 2004, Daddi et al. 2007, Elbaz et al. 2007, Noeske et al. 2007, Catalán-Torrecilla et al. 2015, Gavazzi et al. 2015, Renzini & Peng 2015, Cano-Díaz et al. 2016, Sánchez et al. 2018). In general,

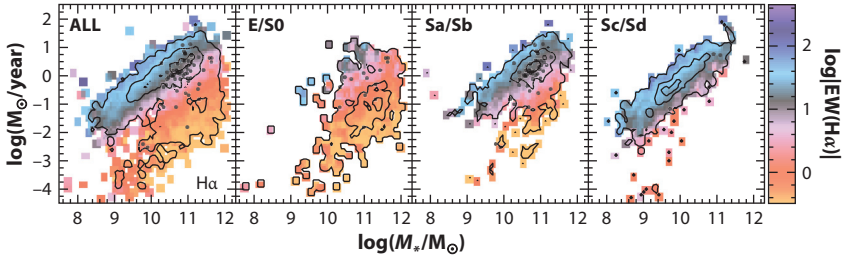

Figure 2

SFR–M_* diagram for all the galaxies included in the integral field spectroscopy compilation presented in this review (*far-left panel*), and subsequent panels show different subgroups segregated by morphology, from more early types to more late types, from left to right. All panels represent the distribution adopting the SFR estimated based on the dust-corrected integrated Hα luminosity following Sánchez et al. (2018). In each panel, the contours correspond to the density of points, with each contour including 95%, 50%, and 10% of the points. In all panels, the decimal logarithm of the equivalent width of Hα is color-coded, following the same code as that shown in **Figure 1**. Finally, the green circles in each panel show the location of the optically selected AGNs (as selected in Sánchez et al. 2018). Abbreviation: SFR, star-formation rate.

the SFMS has a scatter of ∼0.2–0.3 dex in SFR at any redshift, with a slope slightly smaller than one at low redshift, ∼0.8 dex/log(M_*). The SFMS presents a clear evolution in the zero point that increases with redshift (e.g., Speagle et al. 2014, Rodríguez-Puebla et al. 2016). By contrast, RGs are distributed well below the SFMS, following a loose relation with the M_* (or a cloud), broadly corresponding to the location expected for an EW(Hα) ∼ 1 Å (e.g., Stasińska et al. 2008). In between the two groups, there is an area with a much lower number density of galaxies, known as the green valley (GV). Galaxies in the GV (or GVGs) are considered in transit between SFGs and RGs, and their limited number has been interpreted as a consequence of a fast process transforming the former to the latter (e.g., Bell et al. 2004, Faber et al. 2007, Schiminovich et al. 2007). More recently, AGN hosts were found located in the GV of the SFR–M_* diagram (e.g., Torres-Papaqui et al. 2012, Schawinski et al. 2014, Cano-Díaz et al. 2016, Sánchez et al. 2018), as shown in **Figure 2**. Actually, their distribution is spread from the SFMS toward the RGs cloud, covering mostly the GV, and sharing many properties with GVGs (e.g., Sánchez et al. 2018). This result suggests that there is a connection (or coevolution) between the AGN activity and the quenching of SF in galaxies.

The key ingredient of SF is cold gas, from which stars are formed (see, e.g., Kennicutt & Evans 2012, Krumholz et al. 2012). Indeed, Schmidt (1959) already suggested a relation between the SFR and the interstellar gas volume density. This relation was later observed as a relation between the surface densities of both quantities, and it is known as the Schmidt–Kennicutt (SK) or SF law (Kennicutt 1998a). This relation is maintained at kiloparsec scales only for the molecular gas (e.g., Kennicutt et al. 2007, Bigiel et al. 2008, Leroy et al. 2013, and references therein). It is beyond the scope of this review to explore in detail the global SK law and the detailed connection of cold gas with the SF process. However, for the sake of understanding the local processes described later, I should indicate that RGs present a clear deficit of both atomic and molecular gas (e.g., Saintonge et al. 2016, Calette et al. 2018). Thus, the lack of cold gas seems to be the primary reason for the limited SFR (if any). How this deficit of gas is connected to the presence of an AGN is a topic of study, with both heating and removal being the main explanations invoked through the so-called negative feedback (e.g., Silk 1997). Indeed, there are other possible sources of low gas content, related to gas interactions, harassment, and stripping more related to external processes

(e.g., Poggianti et al. 2017). Finally some galaxies may have consumed all the available gas in the surrounding intergalactic medium, but this is far less probable (e.g., Tumlinson et al. 2017).

However, even for the same amount of cold gas, galaxies may present a different star-formation efficiency, SFE = SFR / M_{gas} (e.g., Saintonge et al. 2011), or different scaling factors between the two parameters involved in the SK law (e.g., Elmegreen et al. 2007). Indeed, Colombo et al. (2018) show that SF is less efficient in more early-type galaxies, aside from the fact that they have less molecular gas. In summary, the lack of gas is the primary driver for the halting of SF, but a secondary cause involves a decline in the SFE.

3.3. Gas Phase Mass–Metallicity Relation

Metals are produced as a result of the thermonuclear reactions that make stars shine and during their supernova explosion phases (when it happens).[3] After their deaths (and during their lifetimes too, e.g., Yates et al. 2012), metals are expelled to the ISM, polluting it and enriching the next generations of stars. Therefore, the metal content in the ISM is a tracer of the previous generations of stars, modulated by the gas inflow, outflow, and depletion processes. Oxygen is particularly interesting, being the most abundant metallic element (and the most frequent element after H and He; e.g., Peimbert et al. 2007). Being an α element, it is expelled mostly by core-collapsed supernovae (SNe) generated by the death of short-lived massive stars, and therefore its relative enrichment is tightly related to last SF events. Consequently, it is both a tracer of the overall chemical evolution of galaxies, being a by-product of SF, and a local proxy of how different the SF activity is. It is also modulated by the inflow/outflow of gas in different regions within a galaxy: Gas infalling toward a galaxy is generally more pristine (less metal rich), and gas that is outflowing is generally metal rich (polluting the gas halo).

Averaged across the optical extension of a galaxy, the oxygen abundance correlates with the integrated stellar mass. This relation, known as the MZ-relation or MZR (mass–metallicity relation; although a more correct name should be the M_*–O/H relation), connects the two main products of SF integrated along cosmic time. Known for decades (e.g., Vila-Costas & Edmunds 1992), it was originally expressed also as a luminosity–O/H relation (e.g., Garnett 2002). Tremonti et al. (2004) made the first systematic exploration of this relation using a statistically large and significant sample of galaxies, showing that the two parameters exhibit a tight relation, with a dispersion lower than ∼0.1 dex, covering more than four orders of magnitude in M_*. More recent analysis reduces this scatter to ∼0.05 dex (e.g., Barrera-Ballesteros et al. 2017). **Figure 3** shows the distribution along the M_*–O/H diagram for the full sample of galaxies considered in this review, using a particular calibrator. The shape of the MZR is clearly shown. A full exploration of the differences reported when using different calibrators was discussed by Kewley & Ellison (2008), and more recently revisited by Barrera-Ballesteros et al. (2017), Sánchez et al. (2017, 2019b), and Curti et al. (2019). The MZR presents an almost linear regime for $M_* < 10^{10}$ $M_\odot$, flattening in the range of 10^{10}–$10^{10.5}$ $M_\odot$, and reaching a plateau for more massive galaxies. The extension of the linear regime, i.e., the location of the M_* knee, and the actual asymptotic value depend on the adopted calibrator or procedure used to measure the oxygen abundance (e.g., Barrera-Ballesteros et al. 2017), and the initial mass function (IMF; Salpeter 1955) adopted in the derivation of M_*.[2] However, the shape is almost universal both in the nearby Universe (e.g., Kewley & Ellison 2008; Sánchez et al. 2017, 2019b) and at different redshifts (e.g., Erb et al. 2006, Erb 2008, Henry et al. 2013, Salim et al. 2015). It is worth noticing here that this relation is not very well explored at very low masses, and some authors have reported a change in the slope of flattening in the very

[3] Apart from traces of primordial Li and maybe Be produced in the Big Bang nucleosynthesis.

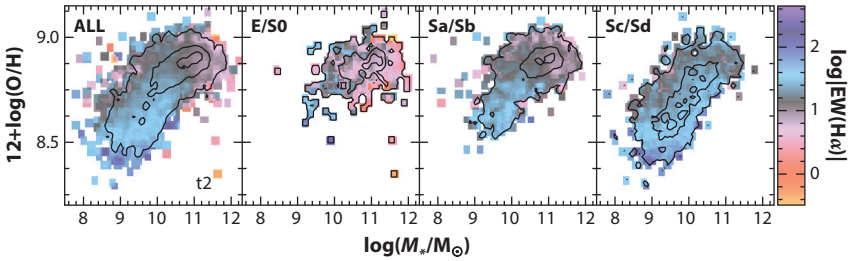

Figure 3

Gas-phase MZR for the collection of integral field spectroscopy–observed galaxies considered in this review with abundances measured at the effective radius (~4,600 galaxies). All panels correspond to the MZR derived using the *t2* calibrator (defined in Sánchez et al. 2019b). The left-most panel shows the distribution for all the galaxies, with similar distributions segregated by morphology shown in subsequent panels, from earlier types to later ones from left to right. Like in **Figure 2**, the distributions are shown as density contours, with contours indicating 95%, 50%, and 10% of the points. Finally, the color indicates the mean value of the EW(Hα) for all galaxies contributing to each point in the distribution, following the same code as that shown in **Figure 1**. Abbreviation: MZR, mass–metallicity relation.

low-mass regime (~10^{6-8} $M_\odot$), which should be confirmed in future explorations (e.g., Blanc et al. 2019, Sánchez et al. 2019b).

At low stellar masses the linear relation between the two parameters is interpreted as a direct consequence of the SFH in galaxies, which is dominated at this regime by a consistent growth of both parameters as integrals of the SFR (modulated by the effective yield in the case of O/H). This regime of the relation indicates that the evolution does not depart too much from that predicted by a closed-box model (e.g., Pilyugin et al. 2007). However, I should note here that a pure closed-box model is known to be unable to reproduce the metallicity distribution of stars even in the Solar Neighborhood (e.g., Pagel & Patchett 1975); this is long-standing result known as the G-dwarf problem (e.g., McWilliam 1997). This is just one of a plethora of observations that the simple closed-box model is unable to reproduce. Furthermore, open models, including both inflows and outflows, can of course reproduce the observed linear trend too, if they compensate for each other (e.g., Trayford & Schaye 2019). However, it is the simplest model that reproduces the linear regime of the MZR.

Larger discrepancies are found in the asymptotic regime, in which an increase in the stellar mass does not produce a significant increase in the oxygen abundance. Tremonti et al. (2004) already interpreted this flattening as a result of galactic outflows that regulate the oxygen abundance (by removing metal-rich gas from galaxies). Different studies support this interpretation (e.g., Davé et al. 2011, Lilly et al. 2013, Belfiore et al. 2016, Weinberg et al. 2017). An alternative interpretation is that gas inflow can produce a similar shape for the MZR (e.g., Sánchez Almeida et al. 2014), with the asymptotic value being a natural consequence of the maximum amount of oxygen that can be produced by stars, i.e., the yield. Pilyugin et al. (2007) already showed that the observed asymptotic value is compatible with the yield predicted by a closed-box model for a gas fraction $f_{\rm gas} \sim 5$–10%, assuming a value of the oxygen abundance derived using calibrators anchored to the direct method. However, recent studies indicate that gas outflows are still required to reproduce the observed shape (e.g., Barrera-Ballesteros et al. 2018). I should stress here that the dominant process driving the outflows must be different in different stellar mass regimes: SFR-driven ones would be far more important at low stellar masses, whereas AGN-driven ones should dominate the high stellar mass range.

More controversial is the presence of a secondary relation between the MZR and the SFR (once removed, the primary relation is between O/H and M_*). In most cases it is described as a trend in which galaxies with larger SFRs at a fixed mass present a lower metallicity. Ellison et al. (2008) first reported the existence of this secondary relation, which was later proposed as (*a*) a modification of the stellar mass by a parameter that includes both this mass and the SFR (known as the fundamental mass–metallicity relation or FMR; e.g., Mannucci et al. 2010), (*b*) a fundamental plane involving the three parameters (known as the mass–metallicity–SFR fundamental plane; e.g., Lara-López et al. 2010), or (*c*) a dependence of the residuals of the primary relation with the SFR or the sSFR (specific SFR; e.g., Salim et al. 2014). Both galaxy inflows and outflows have been proposed to explain the secondary relation (e.g., Sánchez Almeida & Sánchez-Menguiano 2019). The existence of this secondary relation has been questioned by studies based on IFS data (e.g., Sánchez et al. 2013, 2018, 2019b; Barrera-Ballesteros et al. 2017), contrary to most of the previous studies based on single-aperture spectroscopic surveys (e.g., the Sloan Digital Sky Survey or SDSS). In some cases, the existence or not of the FMR depends on the interpretation of the data, as shown by the reanalysis of the IFS data presented by Salim et al. (2014) and Cresci et al. (2019). For most of the studies that claim that there is no FMR, the main parameter used to determine its presence or absence is the significant reduction of the global dispersion of the residual with respect to the average relation when introducing the secondary relation (e.g., figure 9 of Sánchez et al. 2019b). However, for those claiming there is an FMR, the main argument is the difference in the shape of the MZR for different ranges of SFR.[4] It is beyond the scope of this review to enter into this discussion, which has been addressed in more detail recently by Maiolino & Mannucci (2019). Nevertheless, following Barrera-Ballesteros et al. (2017), I note that with the current compilation of data no decrease is appreciated in the dispersion around the MZR when introducing a possible secondary relation with the SFR.

3.4. Age and Metallicity Distributions in Galaxies

Galaxies present a clear bimodal distribution in many different properties that are likely physically connected. In particular, they present a clear bimodality in the SFR–M_* diagram discussed in Section 3.2, which is directly connected with the morphological segregation between early- and LTGs already introduced by Hubble (1926). This bimodality has been more frequently explored using color–magnitude diagrams (CMDs; e.g., Strateva et al. 2001, Bell et al. 2003, Blanton et al. 2003), with early-type galaxies/RGs located along a well-defined region known as the red sequence, and LTGs/SFGs distributed in the so-called blue cloud (as nicely reviewed by Blanton & Moustakas 2009). A more physically motivated version of the CMD is the light-weighted age–M_* diagram, in which galaxies clearly show a sharp bimodal distribution [e.g., Gallazzi et al. 2005, 2008; Sánchez et al. 2018]. This diagram shows that early-type galaxies (E/S0) are strongly dominated by a very old stellar population of ∼10 Gyr having a narrow distribution of ages. This is a direct consequence of a SFH dominated by a strong burst at early cosmological times (e.g., Panter et al. 2003, Thomas et al. 2005, García-Benito et al. 2017), which is frequently modeled with a single burst of SF. On the contrary, late-type spirals (Sc/Sd) contain a considerable fraction of old stars, of similar or slightly lower ages, but with a substantial amount of stars younger than 1 Gyr, and a much wider range of stellar ages. Again, this indicates a smoother evolution (e.g., López Fernández et al. 2016, García-Benito et al. 2017, Sánchez et al. 2019a) and a wider variety of SFHs (e.g., Ibarra-Medel et al. 2016). As expected, early-type spirals (Sa/Sb) present mixed behavior. Their oldest populations have ages similar to those of the early-type galaxies. However,

[4]See Curti et al. (2019) for a counterexample.

they contain a considerable fraction of young stellar populations too, with ages similar to those of the late-type spirals.

Contrary to the global stellar age, stellar metallicity ($[Z/H]_*$) does not show any clear evidence of a bimodal distribution, showing a smooth relation with M_* (e.g., Gallazzi et al. 2005, Panter et al. 2008, Vale Asari et al. 2009, González Delgado et al. 2014a, Sánchez et al. 2018). Stellar metallicity is a by-product of the SF process. However, contrary to the gas phase abundance, which increases with each generation of new massive stars that form (and die), modulated by inflows and outflows, stellar metallicity traces the metal content in the surviving stars (i.e., those of intermediate and low mass). Therefore, its interpretation and the relation with the stellar mass is less evident than that of the oxygen abundance. By contrast, the derivation of the stellar metallicity depends strongly on the data used (photometry/spectroscopy, wavelength range, etc.) and the method adopted to explore the stellar populations: full fossil records, SFHs, and ChEHs adopted or not, comparison with single stellar populations (SSPs), inclusion or not of the [α/Fe] relative abundances, etc. (e.g., Walcher et al. 2011, Conroy 2013). Despite these caveats the lack of bimodality indicates that the quenching process does not affect the metal enrichment significantly, which, in any case, is frozen to the average metallicity from former SF processes.

4. RESOLVED PROPERTIES OF GALAXIES

In the previous sections, I have summarized the main properties of galaxies derived from integrated or aperture-limited spectroscopic surveys. In the current section, I review how these properties are extended to local scales (i.e., ~1 kpc), as uncovered by more recent IFS-GSs.

4.1. Ionized Gas Across the Optical Extension of Galaxies

As indicated in Section 3.1, the ionization in galaxies is produced by local processes[5] that may be different in different locations within each galaxy (e.g., Sharp & Bland-Hawthorn 2010). Averaged across a large aperture, the properties of the ionized gas reveal either the dominant physical process or a mixture of all of them (e.g., Kauffmann et al. 2003). This is illustrated in **Figure 4**, where two composite images are shown, one constructed based on the *g*, *r*, and *i*-band continuum images and the other one based on the [OIII], Hα, and [NII] emission-line maps, extracted from the MUSE (Multi Unit Spectroscopic Explorer) observations of the galaxy IC1657 corresponding to the AMUSING (All-weather MUse Supernova Integral field Nearby Galaxies survey; PI: J. Anderson) (e.g., Sánchez-Menguiano et al. 2018) project. **Figure 4*c*** shows the classical BPT diagnostic diagram (already discussed in Section 3.1 and shown in **Figure 1**). In this case, each dot in the BPT diagram corresponds to a pixel in the RGB emission-line image (**Figure 4*b***). This allows us to easily identify the location within a galaxy at which different ionization happens. A clear biconical ionized gas structure is seen in the center of this galaxy, highlighted as pink colors, indicating strong [NII]/Hα and [OIII]/Hβ line ratios (as seen in the BPT diagram). This structure is a clear signature of shock ionization induced most probably by an outflow driven by a strong nuclear SF event (e.g., López-Cobá et al. 2017b, 2019, 2020). In addition to this structure, it is easy to identify, in the emission-line image, the star-forming regions across the inclined disk (clumpy ionized greenish structures). They present a clear gradient in their line ratios, with green colors toward the center and bluish colors in the outer part (in the emission-line image). This change in the line ratios is frequently interpreted as a signature of the oxygen abundance gradient observed

[5] All sources of ionizing photons are local, not global. A galaxy does not have a single source of ionization. Integrated/average line ratios do not provide full information about the ionization conditions in galaxies.

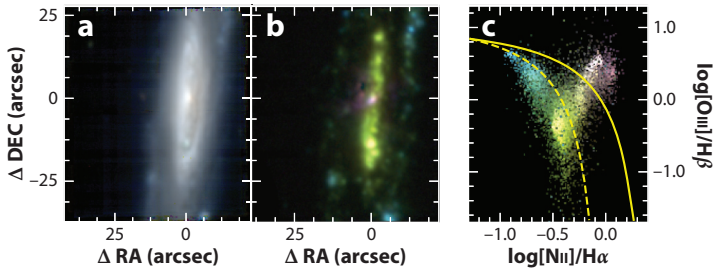

Figure 4

Galaxy IC1657 observed with MUSE (PI: R. Bacon): (*a*) The continuum image, created using *g*- (*blue*), *r*- (*green*), and *i*-band (*red*) images extracted from a MUSE datacube by convolving the individual spectra with each filter response; (*b*) the emission-line image created using the [OIII] (*blue*), Hα (*green*), and [NII] (*red*) emission-line maps extracted from the same datacube using the `Pipe3D` pipeline; and (*c*) the classical Baldwin–Phillips–Terlevich diagnostic diagram involving the [OIII]/Hβ and [NII]/Hα line ratios. Each point in panel *c* corresponds to a single pixel (spaxel) in the other two maps, represented with the same colors as those shown in the emission-line image (*panel b*). The solid and dashed lines represent the locations of the Kewley et al. (2001) and Kauffmann et al. (2003) demarcation lines, respectively. Abbreviations: DEC, declination; MUSE, Multi Unit Spectroscopic Explorer; PI, primary investigator; RA, right ascension. Images provided by C. López-Cobá.

in disk galaxies (e.g., Searle 1971, Vila-Costas & Edmunds 1992, Sánchez et al. 2014). This object is used to illustrate that different ionization sources could be present at different locations within each galaxy. Similar figures to this one for other galaxies are included in **Supplemental Figures 1–8**.[1] In general, all sources of ionization described in Section 3.1 may be present simultaneously (or not) in different galaxies.

Supplemental Material >

Despite the different ionization sources that may be present in a single galaxy, there are patterns within galaxy types, similar to those described for the integrated/average properties. **Figure 5** shows the distribution of individual ionized regions for the subsample of well-resolved galaxies described in Section 2. The adopted procedure to generate these distributions guarantees that they are not dominated by galaxies with a larger number of sampled regions (spaxels): The distribution is generated first for each galaxy, normalizing its integral to one, and then the average for all galaxies is derived (volume corrections are not feasible, because the sample is a compilation). The position of individual regions depends on the mass and morphology of the host galaxy; regions belonging to more massive and early-type galaxies populate the right-hand side of the figure, with lower values for the EW(Hα). In contrast, for late and less-massive galaxies, more ionized regions populate the left-hand side of the diagram with larger values of the EW(Hα). However, contrary to what is seen for the integrated properties of galaxies (shown in **Figure 1**), for the spatially resolved regions a wider range of parameters is covered in most of the diagrams. This reflects the fact that the average properties do not represent the full range of ionization conditions found across the optical extension of individual galaxies (as shown in **Figure 4**).

The distribution of ionized regions depends not only on the properties of the hosting galaxy but also on the location within the galaxy. The barycenter of the number density distributions of ionized regions along the diagram for different galactocentric distances is included in **Figure 5**. In doing so, I estimate the same density distribution, but in consecutive radial bins centered at consecutive galactocentric distances between 0.1 R_e and 2.1 R_e and a width of 0.2 R_e (following the position angle and ellipticity of each individual galaxy). The size of the circles increases with the galactocentric distance of the considered ring. For most galaxy types and stellar masses, there is a clear trend with the radial distance. The ionized regions in the center of galaxies ($R < R_e$) are

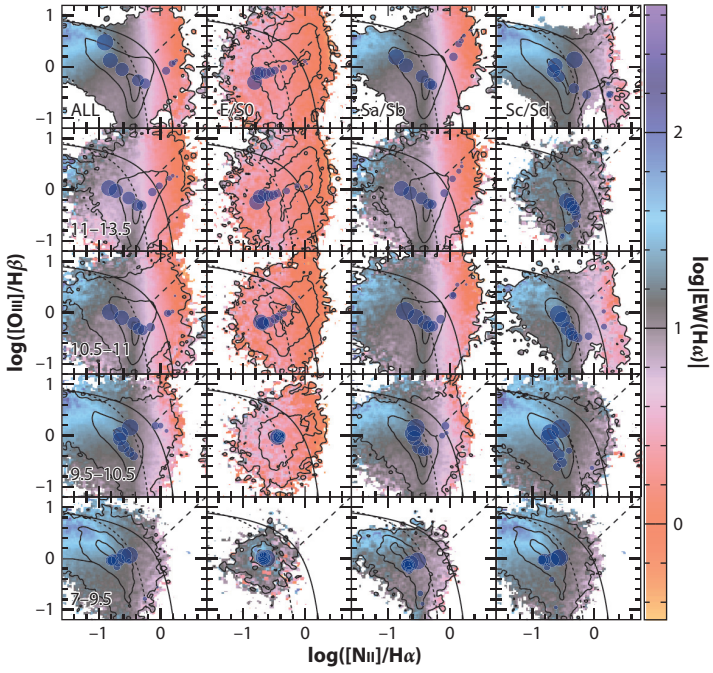

Figure 5

Classical [OIII]/Hβ versus [NII]/Hα diagnostic diagram for the spatially resolved distribution of the ionized gas across the optical extension of the considered sample of galaxies. The average of the logarithm of the equivalent width of Hα at each location is color-coded, and contours represent the density of spaxels, with contours indicating 90%, 50%, and 10% of the points. Blue solid circles represent the barycenter of the number density distribution of ionized regions at different galactocentric distances, represented by the size of circles, ranging from 0.1 R_e (*smallest circle*) to 2.1 R_e (*largest circle*). In all panels, the solid line represents the location of the Kewley et al. (2001) boundary lines, with the separation between Seyferts and LINERs indicated by a dashed line. Finally, the dotted line represents the location of the Kauffmann et al. (2003) demarcation line. The full sample is shown in the upper-left panel, and subsequent panels show a subsample of galaxies segregated by morphology (from *left* to *right*) and stellar mass (from *top* to *bottom*), with the covered ranges labeled in the top- and left-most panels. Abbreviation: LINERs, low-ionization nuclear emission-line regions.

mostly located in the upper-right side of the diagram. However, the outer regions are located either at the upper-left or left side (for most LTGs, apart from the lowest-mass ones) or at the bottom-left side (for early-type ones). However, there are substantial differences for different galaxy types and stellar masses. Early-type galaxies lack the left-side branch corresponding to SF regions in general, and the trend goes just from the upper-right side to the bottom-center. Finally, the lower the mass is, the narrower is the covered range of parameters, particularly for the [NII]/Hα ratio, and the trend is reversed for Sc/Sd galaxies.

The explanation for these distributions has been discussed in different articles. For the center of most massive and early-type galaxies, the location in the diagram and the low observed values for the EW(Hα) indicate that the dominant ionization is due to ionizing old stars, post–AGBs, or HOLMES (Binette et al. 1994, Stasińska et al. 2008, Cid Fernandes et al. 2010). Recent results have shown that this ionization, observed as a diffuse extended ionization in the central regions of early-type galaxies by Sarzi et al. (2010) and Gomes et al. (2016b), is ubiquitous in galaxies of different morphologies at the location of old stellar populations (Singh et al. 2013,

Papaderos et al. 2013, Sánchez et al. 2014). This result was recently confirmed by Belfiore et al. (2017b) and Lacerda et al. (2018). The observed trend from the upper-right side toward the lower-left side of the figure from the center to the outer regions could be explained by a change in the average age of the ionizing population, in agreement with the predictions by models (e.g., Morisset et al. 2016). This result highlights the connection between the observed properties of the ionized gas and those of the stellar populations, showing that in early-type galaxies there should be a negative gradient in the average age of the stellar population, as indeed is observed (e.g., González Delgado et al. 2014b). Finally, for a few early-type galaxies, in particular the less massive ones, there is some marginal SF activity (Gomes et al. 2016b, Méndez-Abreu et al. 2019). This SF could be the residue of a former activity that declines owing to the natural dimming or aging of the disk (e.g., Casado et al. 2015) or a rejuvenation caused by the capture of pristine gas or caused by the early-type galaxy capturing a gas-poor, low-mass galaxy (e.g., Husemann et al. 2011).

The connection with the properties of the stellar populations is even more clear for the LTGs. In those galaxies, there is some ionization due to old stars in the central regions for early-type spirals, i.e., spirals with bulge (Sa/Sb) at $R < R_e$. This is more clearly appreciated in the average distribution of these galaxies and for most massive ones (**Figure 5**, panel labeled S0). For the later-type spirals (Sc/Sd), galaxies without a prominent bulge, the location of the central ionized regions in the diagram is not well defined. This is in agreement with the results by Singh et al. (2013), as indicated previously, because bulges are dominated by older stellar populations. However, the dominant ionization in these galaxies is SF, and indeed the corresponding line ratios are found in the regions usually associated with this ionization, i.e., below the Kewley et al. (2001) curve with large values of the EW(Hα). This is where most of the ionized regions are found, particularly for galactocentric distances greater than 0.5 R_e. In these galaxies, and in particular in those with a stellar mass larger than $10^{9.5}$ $M_\odot$, there is a trend from the bottom-middle toward the upper-left area of the diagram as we move further away in the disk (from 0.5 to 1.5 R_e). This trend can be easily explained as a consequence of the well-known negative gradient in the gas-phase metallicity in spiral galaxies, which has been found to be very similar for all galaxies in this mass regime (Sánchez et al. 2014, Sánchez-Menguiano et al. 2016b). Oxygen abundance presents a positive trend with the [NII]/Hα line ratio (e.g., Pettini & Pagel 2004) as a pure effect of the nitrogen-to-oxygen abundance trend (e.g., Belfiore et al. 2017b). Due to that fact, low-metal SF regions are located at the left-end of the diagram, whereas high-metal regions are distributed to the center. There is also a counterintuitive negative trend between [OIII]/Hβ and O/H, due to cooling effect of metals (e.g., Evans & Dopita 1985), that produces the shift from the upper toward the lower ranges of the SF sequence in this diagram as the oxygen abundance increases. Finally, for the less massive LTGs ($<10^{9.5}$ $M_\odot$), there is a less clear or inverted trend, reflecting that in this regime the abundance gradient is less prominent, flat, or even inverted (Belfiore et al. 2017b, Sánchez & Sánchez-Menguiano 2017).

In summary, the observed distribution reflects the connection between the ionization conditions in star-forming regions and the overall evolution of the underlying stellar population (as described by Sánchez et al. 2015b). As a consequence of this connection, the location of an HII region in a diagnostic diagram is mostly determined by the stellar mass and morphology of its host galaxy and its galactocentric distance. Indeed, this is the reason why we can use HII regions to trace the chemical evolution of spiral galaxies, including that of our own Galaxy (e.g., Mollá & Díaz 2005, Esteban & García-Rojas 2018, Sánchez-Menguiano et al. 2018, Carigi et al. 2019).

These results show that the ionization through the full optical extension of the general population of galaxies is dominated by stellar processes (either young or old). However, in some particular galaxies (e.g., AGNs, galactic outflows hosts, mergers), there are other ionization processes that can clearly outshine the effect of these stellar ionizing sources. This is particularly

true for certain regions within galaxies (i.e., central regions), but it is also evident when the average/integrated ionization properties are explored (as shown in **Figure 1**, where AGNs are identified as blue points above the Kewley curve). However, the frequency of those processes is so low (at least in the nearby Universe), and in some cases the spatial extension is so confined to certain regions in galaxies, that they have little influence in the main trends for resolved regions, as shown in **Figure 5**. In other words, they are blurred by the overwhelming and ubiquitous presence of stellar ionization processes.

Local-age bimodality: areas within galaxies present a bimodal distribution in the Σ_*–age diagram

4.2. Local-Age Bimodality: Σ_*-Age Bimodality

I show in Section 3.4 that galaxies present a clear bimodal distribution along the M_*–age diagram. As indicated in that section, this diagram is a more physically driven version of the CMD, used for decades in astronomy to select star-forming and non-star-forming galaxies (e.g., McIntosh et al. 2014). González Delgado et al. (2014b) first showed the distribution along the Σ_*–age diagram for spatially resolved kiloparsec-scale regions of different galaxies, describing a clear trend toward older populations being located in denser regions of more massive galaxies (and in the central regions). More recently, Zibetti et al. (2017) demonstrated that this distribution is bimodal: The distribution of individual regions within galaxies in the Σ_*–age diagram presents two clear density peaks clustered around old (∼9 Gyr) and young (∼1–4 Gyr) ages, respectively, mostly related to retired regions (dominant in early-type galaxies), and star-forming regions (more frequent in LTGs). In LTGs (particularly in early spirals), the central regions associated with bulges are found around the old-age peak, whereas their disk and spiral arms are located around the young-age one. This is a clear indication of an internal/local-age bimodality. This result is found as a statistical effect when exploring the full sample and also in individual galaxies.

Figure 6 reproduces the results by Zibetti et al. (2017), showing the distribution of individual spaxels in the Σ_*–age diagram for the compilation explored in this review. I show the distributions for all galaxy types and segregated by morphology from earlier to later types. In addition, I show the density peak along Σ_* for different stellar masses. The bimodality uncovered by Zibetti et al. (2017) is clearly seen, showing a strong morphological dependence (with younger regions located in LTGs) and a trend with the stellar masses (with younger regions located in less-massive galaxies). Intermediate spirals (Sb/Sbc) show a clear bimodal distribution, highlighting the connection between the two populations with the bulge (old) and the disk (young). Like in the case of the M_*–age (and CMD), the regions with old stellar populations follow a well-defined region, called the old sequence (resembling the red sequence in a CMD), with very similar ages (∼6 Gyr) for a wide range of Σ_* values. However, young stellar populations cover a considerable range of values, from a few hundred-million years to a few gigayears within the same Σ_* range. The bimodality implies an abrupt/short-lived transition, leading to a local quenching of the SF or a sharp change in the SFHs from the inside out (e.g., Belfiore et al. 2017a, López Fernández et al. 2018). Furthermore, this distribution indicates that all regions with old stellar populations have very similar SFHs (owing to the limited range in ages). However, regions with young stellar populations may present a large variety of SFHs (owing to the spread of ages). This was indeed described by Ibarra-Medel et al. (2016) and García-Benito et al. (2019).

4.3. Local Star-Formation Main Sequence: Σ_*–Σ_{SFR}

I have shown in Section 3.2 that galaxies also present a bimodal distribution in the SFR–M_* diagram, with SFGs following a tight correlation (the SFMS) between the two parameters ($\sigma \sim 0.2$–0.3 dex; once removed the main trend). In 2013, two nearly simultaneous studies, Sánchez

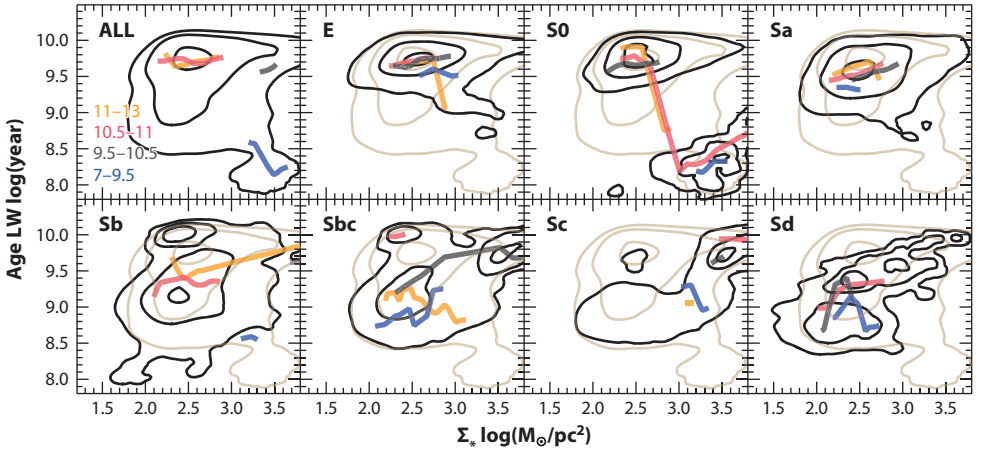

Figure 6

The distribution of the LW ages of the stellar populations from the stellar mass surface densities, shown as density contours (encircling 85%, 50%, and 15% of the regions) in solid black lines. The top-left panel shows the distribution for all galaxies considered in this review, and subsequent panels are segregated by morphology (from earlier galaxies to later ones, from *top left* to *bottom right*). In addition, the trace of peak densities for different integrated stellar mass bins is shown as colored solid lines, with each color representing an M_* bin as indicated in the legend (only densities above 50% are considered in this derivation). Finally, the light brown solid contours reproduce the distribution of the full population (shown in the *top-left panel*). Abbreviation: LW, luminosity-weighted.

et al. (2013) and Wuyts et al. (2013), analyzing completely different samples (at $z \sim 0$ and $z \sim 1$, respectively) and using different techniques (IFS and narrow-band HST imaging, respectively), showed that star-forming regions present a very similar relation between the SFR surface density (Σ_{SFR}) and stellar mass surface density (Σ_*), a relation that holds at kiloparsec scales. This relation is now known as the resolved SFMS (rSFMS) and has been confirmed by many different authors using mostly IFS-GS mainly for galaxies in the nearby Universe (e.g., Cano-Díaz et al. 2016, González Delgado et al. 2016, Maragkoudakis et al. 2017, Abdurro'uf & Akiyama 2017, Hsieh et al. 2017, Ellison et al. 2018, Hall et al. 2018, Medling et al. 2018, Pan et al. 2018, Cano-Díaz et al. 2019, Erroz-Ferrer et al. 2019, Vulcani et al. 2019). They all found that this relation is as tight as the global one, with a dispersion in the range of ∼0.2–0.3 dex (once removed the main trend), and a slope slightly below one. To our knowledge, there is no formal published comparison between the high-z rSFMS and the low-z ones. However, comparing the best-fitted values reported by Wuyts et al. (2013), and adopting a log-linear relation with those reported by the most recent analyses at low z, the rSFMS relation presents a weak evolution in the slope (from $\alpha_{z\sim1} \sim 0.95$ to $\alpha_{z\sim0} \sim 0.78$–$0.94$, respectively) and a very strong evolution in the zero-point (from $\Sigma_{SFR,2_{z\sim1}} = 10^{-6.8}$ $M_\odot$ year^{-1} pc^{-2} to $\Sigma_{SFR,2_{z\sim0}} = 10^{-8.5}$ $M_\odot$ year^{-1} pc^{-2}, with $\Sigma_{SFR,2}$ being the SFR surface density at $\Sigma_* = 10^2$ $M_\odot$ pc^{-2}). This evolution is similar to the one reported by the global SFMS (e.g., Speagle et al. 2014, Rodríguez-Puebla et al. 2016), and it is broadly reproduced by the most recent analysis of hydrodynamical/cosmological simulations (e.g., Trayford & Schaye 2019).

Figure 7 shows the distribution along the Σ_{SFR}–Σ_* diagram for the individual spaxels in my compilation, segregated by both morphology and mass. In this particular case, I adopted the Σ_{SFR} derived from the dust-corrected Hα emission irrespective of the ionizing source, following Cano-Díaz et al. (2016, 2019) and Sánchez et al. (2018). This way Hα traces either the SFR, for

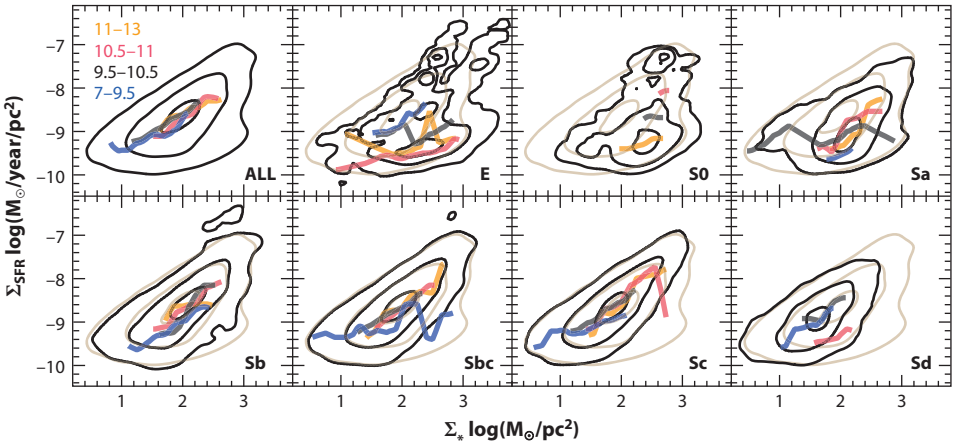

Figure 7

The distribution of the SFR surface densities from the stellar mass surface densities, shown as density contours. Black and brown contours and colored solid lines have similar meanings to those presented in **Figure 6**. SFRs are derived from dust-attenuation-corrected Hα fluxes. Abbreviation: SFR, star-formation rate.

star-forming areas (SFAs) in each galaxy, or just an upper limit to the SFR for non-star-forming/retired areas (RAs). The most recent results show that there is a bimodality in the distribution of areas in this diagram (e.g., Hsieh et al. 2017, Cano-Díaz et al. 2019), with SFAs tracing the described rSFMS relation and RAs located in a cloud well below that relation. Depending on the S/N (signal-to-noise ratio) cut applied to the Hα detection (or any other tracer of the SFR), this second cloud is more-or-less evident. In our particular compilation this cloud is clearly seen only for earlier-type galaxies (E and S0, and less clearly for Sa), and only as a bump in the distribution for all galaxy types. As reported by the same authors, the RAs cloud is dominated by regions in early-type galaxies, whereas the rSFMS is dominated by regions in LTGs, with a clear morphological evolution (as found by González Delgado et al. 2016). The existence of a dependence of the rSFMS with the morphology and other properties of galaxies was also discussed by Medling et al. (2018), Cano-Díaz et al. (2019), and Vulcani et al. (2019). For the bulk population of galaxies, irrespective of their morphologies, the density peak in the diagram traces the rSFMS at any mass. Thus, the mass dependence is weaker than the morphological one. Like in the case of the Σ_*–age bimodality, this is a consequence of the local evolution, with SFAs associated with regions in the disk and RAs associated with regions in the bulge (dominated by quenched regions).

Star-forming areas (SFAs): regions in a galaxy where ionization is dominated by young stars

Retired areas (RAs): regions in a galaxy that do not present any significant amount of or very little star formation

It is worth noticing that the applied cuts in the S/N and the detection limits for properties involved in resolved relations have to be treated with care. Cano-Díaz et al. (2019) explored the effects of the detection limit in the shape of the rSFMS and in the artificial generation of broken distributions resembling two-linear regimes (e.g., Erroz-Ferrer et al. 2019). Finally, the results described above are very similar to those that can be derived using other estimators of the SFR (like the stellar population analysis; e.g., González Delgado et al. 2016).

Besides the increase of the fraction of RAs, some authors (e.g., González Delgado et al. 2016, Cano-Díaz et al. 2019) reported a change in the rSFMS itself with the morphology of the host galaxy. Later spirals (Sc/Sd) present slightly larger Σ_{SFR} than earlier spirals (Sa/Sb) for a fixed stellar mass. This is shown in **Figure 7**, with the rSFMS of Sa (Sc) galaxies being slightly below (above) that of the full population. This result may indicate that the SFH of SFAs in earlier spirals presents a sharper decline with cosmological time (shorter timescales) than in later ones, because

they have a lower Σ_{SFR} at $z \sim 0$ than in the past. Thus, they present a faster evolution or aging than the SFAs of purely disk-dominated galaxies. More recently, Ellison et al. (2020) have demonstrated that the dispersion across the rSFMS is due to changes in the local SFE. This agrees with the described morphological trend, because the SFE does indeed change with galaxy type both globally and locally (e.g., Colombo et al. 2018). There are probably dynamical effects, like the stabilization induced by the bulge proposed by Martig et al. (2009), that precludes the SF in earlier spirals. This effect is a consequence of the removal of stellar mass to the disk that allows the gas disk to be more stable. As a result, an early-type spiral is more stable than an LTG, but only at a fixed stellar mass. Thus, increasing the bulge fraction at a given stellar mass decreases the SFE. However, the SFE does not explain why a region is retired. This seems to be more directly connected with a lack of gas (i.e., with the conditions required to form stars) and being driven by global properties, in particular by the presence of a massive central black hole, as demonstrated by Bluck et al. (2020). In other words, SF is governed by local processes (autoregulation/local feedback), whereas quenching is driven by global ones (in agreement with the results presented in González Delgado et al. 2014b).

4.4. Local Mass–Metallicity Relations

In the previous sections, I showed that the stellar populations present a local bimodality in the M_*–age and SFR–M_* diagrams, with RAs located in a tight old-sequence region in the top-left panel of **Figure 7** and SFAs following a local rSFMS in the latter panels. These local/resolved counterparts of global relations and properties have been explored for other parameters like the MZR. Ryder (1995) already showed that local/spatially resolved oxygen abundance presents a correlation with the surface brightness in the optical band. This relation suggests the existence of a local/resolved MZR (rMZR hereafter). Like in the case of the rSFMS, this relation was proposed in two independent studies by Moran et al. (2012) and Rosales-Ortega et al. (2012) using different techniques. In the first case, classical slit spectroscopy was used to recover the oxygen abundance along the aperture for a sample of SFGs in combination with SDSS photometry to estimate Σ_*. The second study explored the relation among oxygen abundance, Σ_*, and EW(Hα) for the SFAs (HII regions and clusters) detected using IFS (Rosales-Ortega et al. 2010). Both studies show that there is a relation between Σ_* and O/H with a shape that resembles the global M_*–O/H relation: It presents two regimes, with one, just below $\Sigma_* < 10^2$ $M_\odot$ pc^{-2}, having an almost log-linear increase of the oxygen abundance with Σ_*, followed by the other flattening to an asymptotic value at $\Sigma_* \sim 10^3$ $M_\odot$ pc^{-2}. Indeed, Rosales-Ortega et al. (2012) explicitly show that the global MZR can be recovered from the rMZR by integrating the local one along the optical extension of each galaxy. Subsequent studies confirmed the existence of this local relation using larger samples of galaxies and/or SFAs or IFS data with better spatial resolution (e.g., Sánchez et al. 2013, Barrera-Ballesteros et al. 2016, Erroz-Ferrer et al. 2019), which has been recently reproduced by hydrodynamical/cosmological simulations (e.g., Trayford & Schaye 2019). In some cases two-linear relations are proposed for that relation rather than a smooth transition between the two regimes (e.g., Erroz-Ferrer et al. 2019).

Figure 8 shows the distribution in the Σ_*–O/H diagram for the individual spaxels of the explored data set, once more segregated by morphology and stellar mass. In this particular case, only the SFAs have been selected to derive the oxygen abundance, following the criteria outlined in Appendix B. For the remaining regions, the adopted oxygen abundance calibrators may not be valid, as they are anchored to measurements derived for HII regions or photoionization models created to describe these SF ionized structures. Like in the case of the global MZR, the shape of the relation is basically preserved irrespective of the calibrator adopted to estimate the O/H or the assumptions made to derive the stellar mass density. However, the absolute scale of the oxygen

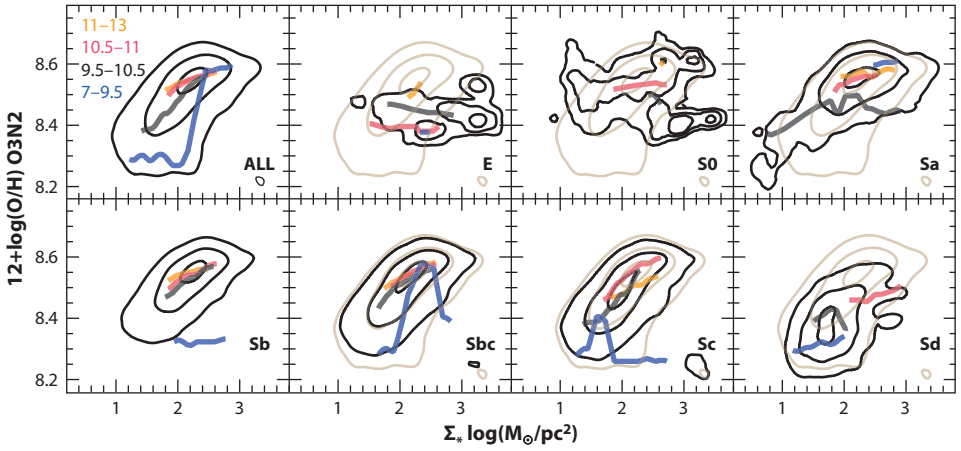

Figure 8

The distribution of the gas-phase oxygen abundances from the stellar mass surface densities, shown as density contours following the nomenclature of **Figure 6**. The O/H was derived based on the M13 calibrator (Marino et al. 2013).

abundance changes with the calibrator (in agreement with the expectations of the results found by Kewley & Ellison 2008). Contrary to those found for the age bimodality and the rSFMS, the distribution of SFAs in the Σ_*–O/H does not present clear deviations with either the stellar mass (for $M_* > 10^{9.5}$ $M_\odot$) or the morphology (for spiral galaxies) aside from the wide range of values covered by each group. In other words, all SFAs seems to be distributed along the same rMZR, with more massive galaxies covering the upper right of the figure and low-mass (and later types, e.g., Sd) covering the lower-left range. Clear deviations from this global trend are shown for low-mass galaxies ($M_* < 10^{9.5}$ $M_\odot$), and maybe the few star-forming regions in elliptical galaxies (E and S0). In the first case, the statistic is poor (due to low number of galaxies). However the result could be interpreted as a consequence of an outside-in chemical enrichment, which I discuss in the upcoming sections. However, for the ellipticals and S0s, maybe the few galaxies with detected SF (Gomes et al. 2016b) are the consequence of the capture of metal-poor galaxies rather than an effect of disk dimming. Indeed, in the case of S0s, the distribution shows two peaks, one following the main rMZR trend and another one more similar to the distribution appreciated for pure ellipticals. Unfortunately, even for the large compilation considered here, the statistic is too low for SFAs in early-type galaxies.

Recent studies have explored whether the rMZR presents a possible secondary relation with the SFR (Σ_{SFR}), following the concept of the FMR. This secondary relation is commonly interpreted as the consequence of gas inflows and outflows (as discussed in Section 3.3). The results of these explorations are not fully conclusive. Some authors claim that there is no secondary relation (e.g., Barrera-Ballesteros et al. 2016, 2017), on the basis of the possible dependence of the residuals of the rMZR with the sSFR and Σ_{SFR}. Other authors claim that there are secondary trends between the residuals of the radial distributions of Σ_{SFR} and O/H (e.g., Sánchez-Menguiano et al. 2019) that at low mass are negative and at high mass are positive. This may be interpreted as evidence for a local/resolved FMR (or rFMR; Sánchez Almeida & Sánchez-Menguiano 2019). However, radial migration and the local effects of spiral arms may produce similar effects (e.g., Sánchez-Menguiano et al. 2016a, Vogt et al. 2017) without involving the same physics claimed to explain the FMR (i.e., a strong effect of outflows and inflows). Finally, there are authors that have reported the existence

of individual anomalous metallicities regions (AMRs) in galaxies that deviate from the rMZR (e.g., Hwang et al. 2019). Like in the case of Sánchez-Menguiano et al. (2019), they consider that gas accretion is the main cause of these deviations. The AMRs are located mostly in interacting systems and in the direction of the close companion, which indeed suggests a nonsecular origin, which is different than the concept of the FMR or rFMR (aimed at describing the quiescent evolution of SFGs in general). So far, with the current compilation of data, the results by Barrera-Ballesteros et al. (2016) are reproduced, showing no significant correlation between the residual of the rMZR and the Σ_{SFR} (i.e., no general/fundamental secondary relation with the SFR is appreciated).

The global and local relations of the oxygen abundance with both M_* and Σ_* are consequences of how α elements (O-like) are produced (i.e., expelled to the ISM mostly by type-II SNe, the direct by-product of SF). By contrast, non-α elements (Fe-like), are introduced to the ISM by different mechanisms, involving the production of new stars (the main enrichment process for α elements, through type-II SNe). The main mechanism for enriching the ISM with these elements is the death of intermediate mass ones (by the production of type-Ia SNe) and by stellar winds over their entire lifetimes (e.g., Yates et al. 2012), as already indicated in Section 3.3. Indeed, the [α/Fe] ratio is strongly related to the shape of the SFHs in galaxies (e.g., de La Rosa et al. 2011). As the SFH changes for galaxies of different masses (e.g., Panter et al. 2003) and morphologies (e.g., López Fernández et al. 2018), and from the inside out (e.g., Pérez et al. 2013, Ibarra-Medel et al. 2016), the dependence of the stellar metallicity with the stellar mass is less obvious than that of the oxygen abundance. The existence of a global stellar mass–metallicity or M_*–[Z/H] relation in galaxies, summarized in Section 3.4, highlights the relation between the shape of the SFH and the stellar mass density (and therefore, the integrated stellar mass, too).

A local counterpart of the M_*–[Z/H] relation has not been broadly explored. To our knowledge, it was presented by González Delgado et al. (2014a), where they showed the distribution along the Σ_*–[Z/H] diagram for the azimuthally averaged mass-weighted stellar metallicities of 300 galaxies extracted from the CALIFA survey. I present in **Figure 9** a similar distribution

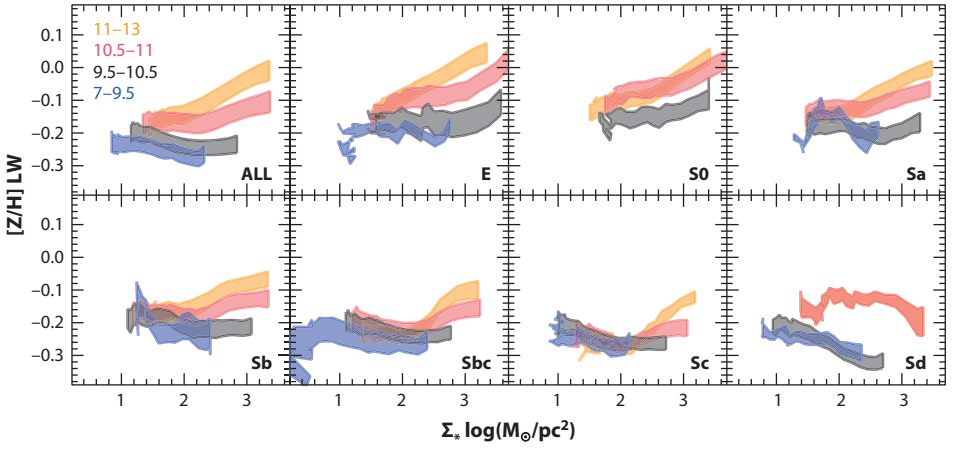

Figure 9

The distribution of the LW metallicities of the stellar populations from the stellar mass surface densities derived from the azimuthally averaged radial distributions described in Section 4.7 for the galaxies considered in this review, segregated by stellar mass and morphology. The top-left panel includes the distributions for all the galaxies, with different colors indicating different mass ranges, and subsequent panels include the same distributions for different morphologies, from earlier (*top left*) to later types (*bottom right*). Abbreviation: LW, luminosity-weighted.

for the collection of data adopted here. Following González Delgado et al. (2014a), in order to minimize the scatter introduced by the large uncertainties in the derivation of [Z/H] in individual spectra, I first derive azimuthal average values in bins of 0.1 R_e for each galaxy (i.e., I create radial distributions of [Z/H], which I discuss later in Section 4.7.2). Broadly speaking, the results are consistent with those presented by González Delgado et al. (2014a), with the local [Z/H] increasing with Σ_*, in particular for the same stellar mass regime ($M_* > 10^{9.5}$ $M_\odot$, once considered the differences in the adopted IMFs). This agrees with the existence of a negative stellar metallicity gradient in most massive galaxies (e.g., González Delgado et al. 2014b, Oyarzún et al. 2019). However, contrary to what happens with the rMZR, the local stellar metallicity–Σ_* relation is not the same for all galaxies. It depends strongly on galaxy mass and morphology. In particular, for low-mass LTGs, the distribution of [Z/H] along Σ_* is almost flat or even negative. This indeed agrees with a flattening of the stellar metallicity gradient observed in this kind of galaxy (González Delgado et al. 2014b). In addition, the observed differences of the behavior between the gas phase (oxygen) and stellar metallicities across galaxies implies a change in the SFHs and, therefore, a differential ChEH for α and non-α elements.

4.5. Local Schmidt–Kennicutt Law

The birth of new stars comprises two different processes. First, the diffuse atomic gas is transformed into highly dense molecular gas. Second, stars are born owing to the dynamical collapse of self-gravitating portions of those molecular clouds. Schmidt (1959) proposed that the SFR should depend on the mass of gas included in a volume, assuming that all stars are formed locally from the original available gas and that there was no interexchange (of stars and gas) with the near environment (i.e., $SFR = M_{gas}^n$). However, the power-scaling factor (n) between both quantities was not defined. Kennicutt et al. (1989) proposed that this scaling factor could be derived through the gas free-fall time (τ_{ff}), following the equation $\rho_{SFR} \propto \rho_{gas}/\tau_{ff}$, by assuming that all gas collapsed within this time is transformed into stars. Considering that $\tau_{ff} \propto \rho_{gas}^{-0.5}$, they conjectured that the basic SK law should follow a relation $\rho_{SFR} \propto \rho_{gas}^{1.5}$. Empirically, Kennicutt et al. (1989) and Kennicutt (1998a) demonstrated that indeed the surface density of the SFR follows a relation with the gas surface density similar to the proposed one.[6] This relation was derived originally galaxy wide, and it is known as the SK law.

As discussed in previous sections, SF, and in particular the collapse of molecular clouds, is a local process that happens at much smaller scales than galaxy size. Spatially resolved observations have shown that indeed the SK law is verified only for molecular gas (Wong & Blitz 2002, Kennicutt et al. 2007), a result confirmed for integrated quantities too (e.g., de los Reyes & Kennicutt 2019). At kiloparsec scales, the SK law shows an almost linear relation (e.g., Bigiel et al. 2008, Leroy et al. 2008). Therefore, the depletion time ($\tau_{dep} = \Sigma_{gas}/\Sigma_{SFR}$) or SFE ($=\Sigma_{SFR}/\Sigma_{gas}$) is almost constant at these scales (Bolatto et al. 2008, Hughes et al. 2010), with a value of ∼2 Gyr (e.g., Bigiel et al. 2008, Rahman et al. 2012, Leroy et al. 2013). However, these studies are biased toward low-mass LTGs. It is still not known if these results hold in more massive or more early-type galaxies. The particular conversion factors to derive the molecular gas and the adopted IMF may play a role in these results. It is known that there are clear deviations from the SK law (thus variations in τ_{dep}) at subkiloparsec scales (Schruba et al. 2011, Kruijssen & Longmore 2014, Kruijssen et al. 2019), in extreme starburst galaxies (e.g., Daddi et al. 2010, Genzel et al. 2010), in the center of galaxies (Jogee et al. 2005, Leroy et al. 2013, Utomo et al. 2017), in regions near strong spiral arms or with different local dynamical states (Schruba et al. 2019), and in early-type galaxies (Davies et al.

[6] In purity, the two relations are the same only if the scale height is constant, which could not be the case.

2014). The average τ_{dep} within a galaxy presents a clear dependence with sSFR and M_* (Saintonge et al. 2017). All these results clearly indicate that the combination of the optical spectroscopic information provided by IFS-GSs, for a wide variety of galaxies, with estimations of the cold gas content at similar spatial scales, is crucial to understanding these processes (e.g., Bolatto et al. 2017, Ellison et al. 2020). It is beyond the scope of this review to make a detailed exploration of the cold gas content in galaxies (atomic or molecular), or to explore the SK law at different scales (see Kennicutt & Evans 2012 and Bolatto et al. 2013, for detailed reviews on the topic). In this section, I summarize the most recent results based on the combination of IFS data with molecular gas at kiloparsec resolutions.

So far the number of galaxies sampled by both IFS-GSs and spatially resolved molecular gas observations is small. Pioneering studies cover mostly early-type galaxies observed by the SAURON (Spectrographic Areal Unit for Research on Optical Nebulae) and ATLAS^{3D} surveys (e.g., ∼40 galaxies; Alatalo et al. 2013). More recent explorations range from a handful of objects (e.g., Belli et al. 2017, Stark et al. 2018) to a few tens [like the ∼47 galaxies in the ALMAQUEST (ALMA-MaNGA QUEnching and STar formation survey) collection; Lin et al. 2017, Ellison et al. 2020], to a well-defined sample of over one hundred galaxies (EDGE–CALIFA sample; Bolatto et al. 2017). There are a few ongoing surveys, like PHANGS (Physics at High Angular Resolution in Nearby GalaxieS; Rosolowsky et al. 2019), but they are focused on large galaxies in the Local Universe that can hardly be a representative sample of the $z \sim 0$ population owing to the cosmic variance and the limited sample volume.

To highlight the urgent need for complementary explorations of the molecular gas on a large sample of galaxies already covered by IFS-GSs, I present in **Figure 10** the spatially resolved distribution in the Σ_{SFR}–Σ_{gas} diagram for the sample of galaxies considered in this review. Lacking spatially resolved information for the molecular gas, I adopted the dust-to-gas conversion proposed by Barrera-Ballesteros et al. (2020) (using data from the EDGE-CALIFA survey) and already used by Galbany et al. (2017) and Sánchez et al. (2018). It involves an additional scatter of ∼0.3 dex to the relation, but it is the best proxy so far that I can adopt. Despite these limitations, there is a

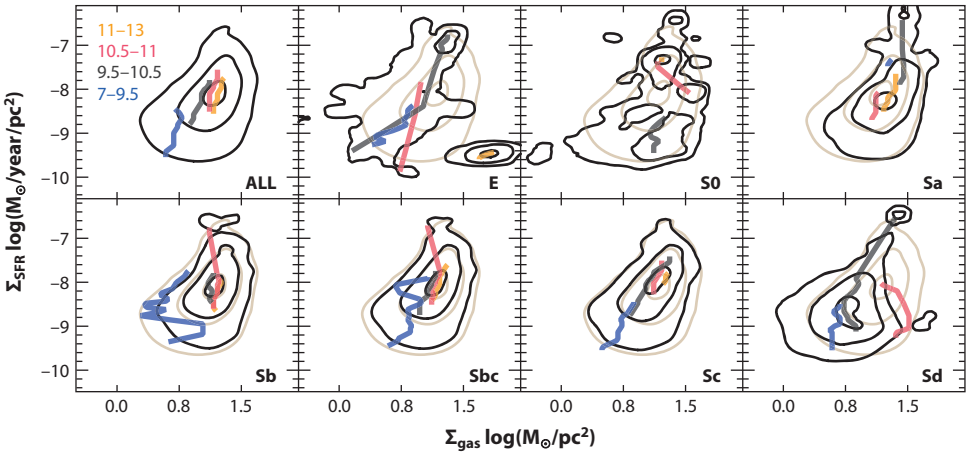

Figure 10

The distribution of the SFR surface densities (derived from the Hα luminosity) from the molecular gas-mass surface densities (derived from the dust attenuation), shown as density contours. Black and brown contours and colored solid lines have similar meanings to those presented in **Figure 6**. Abbreviation: SFR, star-formation rate.

clear relation between the two parameters, with a slope near one ($\alpha = 1.12 \pm 0.09$) and an average $\tau_{dep} \sim 1.7$ Gyr, in agreement with published results. The dispersion of the relation, ∼0.1 dex, is clearly below the expected individual errors, which validates the approach adopted. When this relation is explored using estimations of the molecular gas based on direct CO observations, the scatter is as low as ∼0.05 dex (e.g., Bolatto et al. 2017, Lin et al. 2019, Ellison et al. 2020). Indeed, it is possible that the rSFMS and the SFMS are direct consequences of this relation through the tight Σ_{gas}–Σ_* and M_{gas}–M_* relations shown by Lin et al. (2019) and Calette et al. (2018), respectively.

Earlier-type galaxies present shallower relations ($\alpha \sim 0.8$–0.9) with a larger dispersion, and larger τ_{dep} (∼10 Gyr), than late types that present steeper slopes ($\alpha \sim 1.2$–2.7), smaller dispersions, and lower τ_{dep} (∼0.5 Gyr). Both results agree with the most recent explorations by Colombo et al. (2018), Utomo et al. (2017), and Lin et al. (2017) using direct estimations of the molecular gas derived from CO observations, and they agree broadly with the model presented by Belfiore et al. (2019a). These results indicate that the aging and quenching of the SF is driven by not only the lack of molecular gas (e.g., Saintonge et al. 2016) but also a decline in the SFE (i.e., increase in τ_{dep}; e.g., Sánchez et al. 2018). The observed differences imply that most probably there is no unique τ_{dep} (or SFE) value or single SK law for all galaxies and areas within them (e.g., Ellison et al. 2020), contrary to the early evidence. In other words, τ_{dep} (SFE) may depend on additional parameters whose inclusion in the SK law would reduce the scatter in the $\Sigma_{SFR} \propto \Sigma_{gas}$ relation (e.g., Dey et al. 2019, Bluck et al. 2020).

Following this reasoning, it is possible to reconcile the observed differences for high-redshift starburst galaxies and nearby disks, and even between the observed differences in the central and outer regions of galaxies. The processes involved entail (*a*) the inclusion of the orbital or dynamical time (τ_{dyn}), which connects the gravitational instability (due to bar or spiral arms) with an abrupt increase of the SFE (Elmegreen 1997, Silk 1997); (*b*) the gas velocity dispersion as a measurement of the local pressure that increases owing to the SF feedback (Silk 1997); (*c*) the stellar velocity dispersion, in particular in bulges, that stabilizes the molecular clouds, preventing the SF (Martig et al. 2009); (*d*) the local gravitational potential traced by Σ_* (that would connect the SK law with the SFMS) (e.g., Saintonge et al. 2011); (*e*) the gas metallicity that facilitates the cooling; or (*f*) a combination of all of these (e.g., Dey et al. 2019). In summary, the current results indicate that the SF follows the SK law only at a first order.

Furthermore, considering the SK law, the SF quenching (either global or local) may be related to a deficit of cold gas. As indicated before, there is a global (and local) M_{gas}–M_* (Σ_{gas}–Σ_*) relation for SFGs (and SF regions). This relation is not verified for early-type galaxies that present a deficit of neutral (at least molecular) gas with respect to their LTG counterparts of the same M_* (e.g., Calette et al. 2018, and references there in). This deficit is considered the primary cause of the global decline of the SFR observed in these objects (e.g., Saintonge et al. 2011). The same deficit is observed at local scales, where retired regions present lower Σ_{gas} than star-forming ones at the same Σ_*. With the explored compilation of data, I confirm this trend.

The origin of this deficit is still not clear. Several authors propose that it is originated by AGN feedback, by either removing gas due to galactic winds or heating gas and preventing it from collapsing and forming stars (e.g., Sanders & Mirabel 1996, Hopkins et al. 2009). However, the evidence connecting AGNs and quenching is still circumstantial: (*a*) It seems to be the only process energetic enough to produce this effect (e.g., Croton et al. 2006, Henriques et al. 2019), and (*b*) their hosts are located in the GV between SFGs and RGs (e.g., Kauffmann et al. 2003, Sánchez et al. 2004, Schawinski et al. 2014), as indicated in Section 3.2, sharing many of their properties with GV galaxies (e.g., Sánchez et al. 2018, Lacerda et al. 2020). However, there are still problems in this scenario, like the lack of direct evidence (although see Fabian 2012) and the mismatch of the timescales between quenching (∼1–2 Gyr) (e.g., Sánchez et al. 2019a) and the length of an AGN

lifetime (∼1–100 Myr; e.g., Bird et al. 2008). Other authors indicate that the presence of the bulge itself could stabilize the atomic gas, preventing it from collapsing and forming molecular clouds or decreasing the SFE (e.g., Martig et al. 2009). In this case, a decline in the general SFE (and toward the center) could contribute to the halt of the SF (or give support to this halt, as suggested by Bluck et al. 2020). An additional complication is that the presence of an AGN is directly linked with the presence of a bulge through the Magorrian et al. (1998) relation (e.g., Kormendy & Ho 2013). Therefore, a clean distinction between the two processes is difficult.

Downsizing: evidence that more massive galaxies completed the SF episodes in earlier epochs than less massive ones

4.6. Spatially Resolved Star-Formation Histories

The analyses adopted in the different publications reviewed in the previous sections exploring the properties of the stellar populations rely on the assumption that the observed spectra of galaxies (and regions within galaxies) preserve the imprints of their cosmological evolution and that these imprints can be used to trace back that evolution. This method is known as the fossil record and has been reviewed in detail by other authors (e.g., Walcher et al. 2011, Conroy 2013). In particular, Walcher et al. (2011) explore how the main properties of the stellar populations (luminosity and mass-weighted ages and metallicities, dust attenuation and masses) can be derived from the decomposition of the stellar continuum (and its limitations).

In principle, from these analyses, it is possible to recover SFHs and ChEHs. The fossil record methods have two main implementations. One adopts a particular shape for the SFHs and ChEHs (e.g., Gallazzi et al. 2005, Thomas et al. 2010, Bitsakis et al. 2016, Zibetti et al. 2017) and compares the observed spectra with those predicted, tuning/fitting certain parameters that govern the functional forms considered, e.g., the decay time of an exponential SFH (τ) or the time delay for the ignition of SF in the Universe ($t_{\rm delay}$). A second approach consists of a nonparametric exploration of the SFHs (and ChEHs) based on their decomposition in single bursts of SF. Each burst produces an SSP, a set of stars born all at a certain time (and therefore with the same age as they evolve) from the same gas with a certain metal content (e.g., Panter et al. 2007, Vale Asari et al. 2009, Pérez et al. 2013, Ibarra-Medel et al. 2016, García-Benito et al. 2017). The first approach is unable to reproduce in detail the full spectral features of the observed spectra, and it is frequently used to compare broad- (or medium-) band photometry or particular stellar features (like stellar indices; e.g., Gallazzi et al. 2005, Zibetti et al. 2019). However, the first approach provides SFHs (and ChEHs) that are more easily interpreted. The latter approach is able to reproduce the details of the observed spectra; however, the interpretation of the results is frequently less obvious. It is technically complex and prone to large uncertainties (e.g., Cid Fernandes et al. 2014, Sánchez et al. 2016b). The results depend strongly on the selected templates of SSPs or the stellar libraries (e.g., González Delgado et al. 2014b) and on how the errors propagate when nonlinear components are considered, like the dust attenuation or the stellar kinematics (Cid Fernandes et al. 2013, 2014). Finally, the latter approach relies on the assumption that the SSPs are eigenvectors, which is mathematically not right. Therefore, it may present different degeneracies, like those of the age–metallicity or the metallicity–velocity dispersions (e.g., Sánchez-Blázquez et al. 2011). Further issues, involving stellar evolution isochrones, dust extinction curve, the IMF that is assumed, the stellar template that is adopted, and so on, are discussed in detail by Walcher et al. (2011). I should clarify that most of these caveats apply to the parametric methods too.

Using the fossil record method, the following was possible: (*a*) to confirm the downsizing in galaxies (e.g., Pérez-González et al. 2008; Thomas et al. 2005, 2010); (*b*) to explore cosmic evolution of the SFR density in the Universe (e.g., Panter et al. 2007, López Fernández et al. 2018, Sánchez et al. 2019a), reproducing the distribution derived from direct observations (e.g., Madau et al. 1998, Madau & Dickinson 2014); and (*c*) to predict the global ChEH of galaxies

Local downsizing: evidence that more massive (or central) regions within a galaxy complete the SF episodes in earlier epochs than do less massive (or outer) regions

(e.g., Asari et al. 2007). Most of those results were based on single-aperture spectroscopic data and/or integrated multiband photometry, and therefore, they trace the evolution of galaxies as a whole (or they attempt to do so, although they just cover a single aperture per galaxy for the spectroscopic data set). The advent of IFS-GSs has allowed the exploration of the spatially resolved SFHs of galaxies, too. The pioneering study by Pérez et al. (2013), using a limited sample extracted from the CALIFA survey, first demonstrates that the downsizing is spatially preserved: (*a*) The central and outer regions of more massive galaxies grow faster than those of less massive ones; (*b*) the inner regions of galaxies more massive than $\gtrsim 10^{9.5-10}$ $M_\odot$ assemble their mass faster than the outer regions, following an inside-out growth. It is worth noticing that evidence of inside-out growth was already described, mostly for disk galaxies, using direct imaging explorations on large cosmological surveys (e.g., Barden et al. 2005, van Dokkum et al. 2013). (*c*) For less-massive galaxies ($\lesssim 10^{8-9}$ $M_\odot$) there is a possible transition from the inside out toward the outside in. Keep in mind that in this context the difference between inside out and outside in refers to the speed at which SF happens and not to the amount of stellar mass formed. Low-mass galaxies have a peak in their stellar mass density in their centers; they do not form as rings. However, they form stars more steadily in the central regions than in the outer ones.

Recent updates of these results, using the full CALIFA sample, including UV photometry and/or adopting a different inversion method, were presented by González Delgado et al. (2017), García-Benito et al. (2017), and López Fernández et al. (2018). These results were broadly confirmed with the exploration by Ibarra-Medel et al. (2016) using a much larger sample of galaxies extracted from the MaNGA survey. The main difference between this latter study and the previous one is that at low stellar masses the outside-in does not seem to be universal (note that this mass regime was not well covered by the original CALIFA sample). In this later work, the diversity of spatially resolved SFHs (rSFHs, hereafter) was studied, finding that more massive galaxies present very similar rSFHs at the different spatial regimes explored. However, as the integrated mass decreases, galaxies present a much greater variety of rSFHs (which implies a larger dispersion in their average properties, like age and metallicity). However, on average, low-mass galaxies follow outside-in rSFHs, in agreement with the distributions found in the Σ_*–O/H and Σ_*–[Z/H] diagrams (Section 4.4). The validity and limitations of this method and the results reported were explored through the analysis of postprocessed cosmological hydrodynamics simulations, where the rSFHs are well known (Ibarra-Medel et al. 2019).

I reproduce these results in **Figure 11**, which shows the average evolution of the stellar mass density at different look-back times and for different radial bins, Σ_* (r, t) for the sample of galaxies explored here. Different panels show the distributions segregated by mass and morphology. Following Pérez et al. (2013) and Ibarra-Medel et al. (2016), the radial bins are selected normalized to the current ($z = 0$) observed effective radius. The figure shows that more massive galaxies indeed present larger values of Σ_* (r, t) than do less massive ones at any radius and cosmological time (i.e., the local downsizing/resolved downsizing). This segregation is also seen for different morphologies, with earlier-type galaxies having larger Σ_* (r, t) than LTGs not only at any r and t but also at any stellar mass bin. Thus, the local downsizing depends not only on the mass but also on the morphology. This result was published by García-Benito et al. (2017), who show that the local downsizing and inside-out growth have a trend with $\Sigma_{*,\mathrm{cen}}$ (the stellar mass density in the center, ∼1 kpc, of galaxies). Indeed, their results suggest that the diversity in the rSFHs found by Ibarra-Medel et al. (2016) for low-mass galaxies has a clear dependence with this parameter.

García-Benito et al. (2017) reported two additional results: (*a*) The scale-length of galaxies in mass is smaller (on average) than the corresponding parameter in light (characterized by r_{50}). This result was already shown by González Delgado et al. (2014b). Although I do not show a similar plot, this result is clearly reproduced with the sample explored in this review. (*b*) The

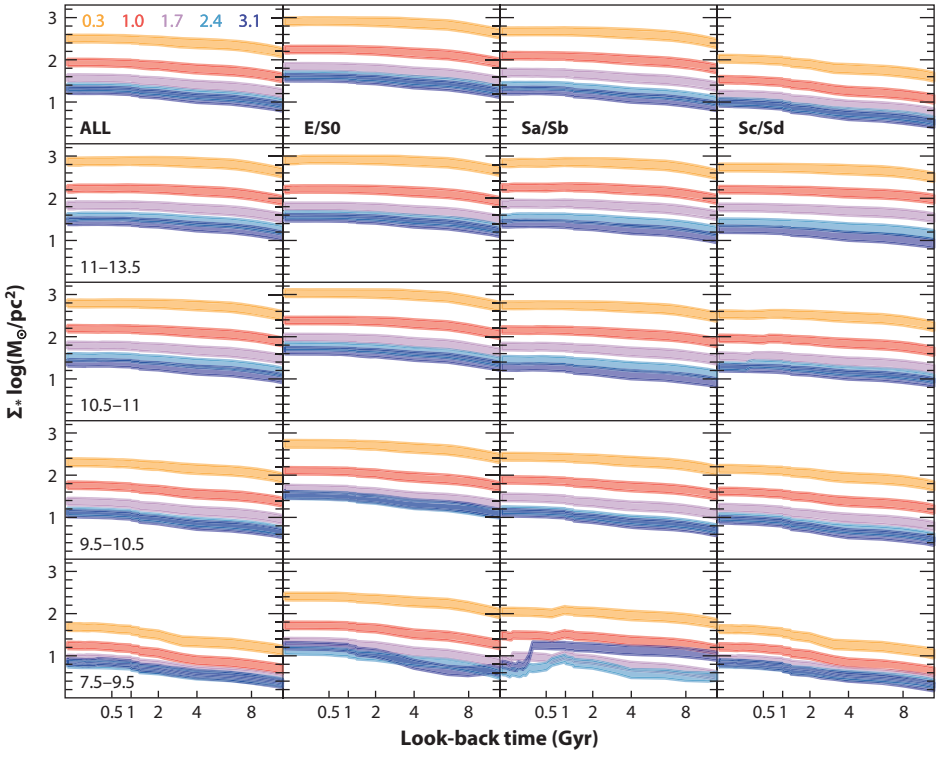

Figure 11

The distribution of the cumulative stellar mass surface densities at different galactocentric distances (labeled with different colors) along the look-back time for all galaxies considered in this review with spatially resolved information (*top-left panel*) and for galaxies of different morphology (subsequent panels from *left* to *right*) and/or stellar masses (from *top* to *bottom*).

local downsizing (understood as the speed of mass assembly) with morphology may be broken for Es/S0s, which seem to form their outer regions at a slower rate than Sas. A possible explanation is that in early-type galaxies, captures/minor mergers affect the mass-assembling history in the outer regions, resembling a change in the local downsizing, as proposed by Oyarzún et al. (2019). Further explorations, and in particular deep comparisons with mock/simulated galaxies (following Ibarra-Medel et al. 2019), are required to fully understand all these results.

4.7. Radial Gradients of Galaxy Properties

It is clear that the properties of the stellar populations and ionized gas change along the optical extensions of galaxies, showing patterns and relations that reassemble well-known ones derived for integrated properties. In many cases, the explored physical parameter (Σ_{SFR}, age, [Z/H], O/H, or Σ_{gas}) presents clear dependencies with Σ_*. As this parameter presents a clear radial trend in galaxies (e.g., González Delgado et al. 2014b), many of the analyzed parameters are expected to present radial trends too (e.g., Barrera-Ballesteros et al. 2016). Besides these radial trends, due to the different substructures observed in LTGs, like spiral arms and bars, azimuthal or local deviations from the pure radial distribution are expected (e.g., Sánchez-Menguiano et al. 2016a). Despite the reduction of one dimension, and the decrease of information, radial gradients provide a simple way to visualize trends in galaxies as well. In this section, I review the most recent results

regarding the radial distribution of the spectroscopic properties of galaxies and their relation with the observed patterns described in previous sections.

Throughout this review, all radial distributions are shown with distances normalized to the effective radius of each galaxy (R_e, already used in **Figure 5**). I adopt this scheme instead of representing them in physical scales to facilitate comparisons among galaxies covering a wide range of sizes possible. This method was introduced by Sánchez et al. (2012b) and nowadays is commonly used (e.g., González Delgado et al. 2014b, 2015, 2016; Sánchez-Menguiano et al. 2016b, 2018; Belfiore et al. 2017b), because it uncovers patterns not clearly seen when using physical sizes (e.g., Pérez et al. 2013, Ibarra-Medel et al. 2016). Furthermore, the effective radius has been proved to be really effective, with most of the physical parameters sampled at this distance being representative of the average values across the optical extension of galaxies (e.g., Moustakas & Kennicutt 2006, Sánchez et al. 2013, González Delgado et al. 2014b).

4.7.1. Stellar mass density gradients. It is well known that the radial distribution of the azimuthal averaged surface brightness profiles (SBPs) presents an almost monotonic decrease for almost all galaxy types of any stellar mass. In the case of disk-dominated spiral-like galaxies, this profile is well characterized, as a first order, by an exponential function of the radius (Freeman 1970) or a double exponential profile (e.g., Courteau et al. 1996). However, the SBP of early-type galaxies (or the bulge of LTGs) is better represented by a sharper profile, well described by an exponential of the 1/4th power of the radius (de Vaucouleurs 1959), or a more general profile known as the Sérsic profile (Sérsic 1968), for which the adopted functional form is an exponential of the $1/n_s$ power of radius, where n_s is known the Sérsic index (see the sidebar titled Functional Forms for Flux Intensity Radial Profiles).

In general, early-type spirals (Sa/Sb) require a combination of a single or a double exponential plus one of the functional forms described to characterize the bulge. The description of other structural components, like a bar, requires the inclusion of further functional forms (e.g., Méndez-Abreu et al. 2017, and references therein). Irregular or interacting galaxies show much more complex radial profiles, and in many cases their characterization requires a full analysis of the two-dimensional distribution using more complicated functional forms (e.g., Peng et al. 2010, Méndez-Abreu et al. 2017).

The radial decline of the SBP is nowadays accepted to be a consequence of an almost monotonic decline in the stellar mass density (Σ_*), via a conversion through the M/L ratio (e.g., Bakos et al. 2008). In general, the M/L ratio presents a log-linear relation with optical colors, which is a simple consequence of the color–age relation in stellar populations (e.g., Bell & de Jong 2001, Zibetti et al. 2009). As galaxies contain older stellar populations in their central regions (e.g., González Delgado et al. 2014b), the M/L ratio enhances the radial decline of Σ_* with respect to that of the SBP. For this reason, the R_e in light is larger, in general, than the one derived in mass (as indicated in the previous section). The advent of IFS-GSs has allowed exploration of the spatially resolved distribution of the stellar population content, providing more accurate M/L ratios at kiloparsec

FUNCTIONAL FORMS FOR FLUX INTENSITY RADIAL PROFILES

- Freeman: $\ln I(R) = \ln I_0 - kR$
- de Vaucouleurs: $\ln I(R) = \ln I_0 - kR^{1/4}$
- Sérsic: $\ln I(R) = \ln I_0 - kR^{1/n_s}$, where $I(R)$ is the flux intensity at radius R; I_0 is the central flux intensity; k is a scaling parameter; and n_s is the Sérsic index.

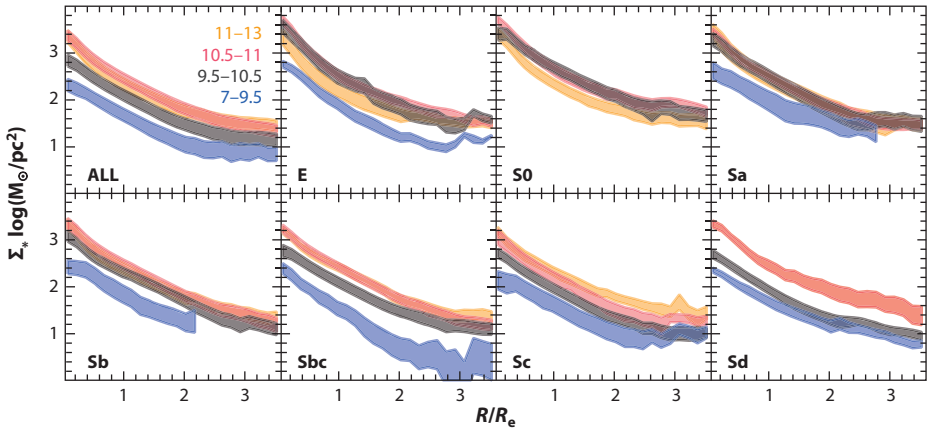

Figure 12

Azimuthally averaged radial distributions of the stellar mass surface density for the galaxies considered in this review, segregated by stellar mass and morphology (as indicated in the legend). The top-left panel includes the radial distributions for all the galaxies, with different colors indicating different mass ranges, and the subsequent panels include the same distributions for different morphologies, from earlier (*top left*) to LTGs (*bottom right*).

scales (e.g., García-Benito et al. 2019). This improves the derivations based on colors (e.g., Bell & de Jong 2001) adopted in previous studies (e.g., Bakos et al. 2008). These new data sets facilitate the systematic exploration of the radial distributions of Σ_* in galaxies of different morphology and stellar mass.

Figure 12 shows the radial distribution of Σ_* for the current adopted compilation. As stated beforehand, all galaxies, irrespective of their morphology and mass, present a decline of Σ_* with radius. The central ($\Sigma_{*,\mathrm{cen}}$) and effective (Σ_{*,R_e}) stellar mass densities increase with the integrated mass and morphology (from late to early types) for galaxies later than S0s (e.g., García-Benito et al. 2017). González Delgado et al. (2014b) already showed that elliptical galaxies are more compact, with a steeper radial decrease of Σ_*, particularly the more massive ones. Note that when the radial distribution of Σ_* is not normalized by R_e, the picture changes, because there is a correlation between M_* and R_e (e.g., Cappellari 2016, van de Sande et al. 2019).

González Delgado et al. (2014b) showed that galaxies, in general, present two regimes in the radial distribution of Σ_*, one at $R < 0.5\,R_e$, (with a slope α between $\sim$−0.5 dex/R_e and $\sim$−1.5 dex/R_e), and another one at $R > 0.5\,R_e$ (with an almost constant slope of $\alpha \sim -0.5$ dex/R_e). The first regime corresponds (broadly) to the bulge, whereas the second regime corresponds to the disk (for LTGs). Finally, the radial profile is steeper ($\sim$−1.5 dex/R_e) for more massive galaxies and shallower for less massive ones ($\sim$−0.5 dex/R_e). All these trends are qualitatively illustrated in **Figure 12**. They agree with the explorations of the rSFHs reviewed in previous sections: The stellar mass assembles faster and with stronger intensities (higher SFRs) in the inner regions of more massive/early-type galaxies than it does in the outer regions of less massive LTGs.

4.7.2. Stellar age and metallicity gradients. Pioneering works on the radial gradients of colors and stellar indices were already performed four decades ago (e.g., Faber 1977). Radial changes in both properties were interpreted as physical variations in the average ages (and metallicities) of the stellar populations. The combination of better quality long-slit spectroscopy with broad-band imaging, focused on the study of elliptical galaxies (e.g., Peletier et al. 1990, González 1994), shows that these galaxies present a shallow gradient in age and a clear negative

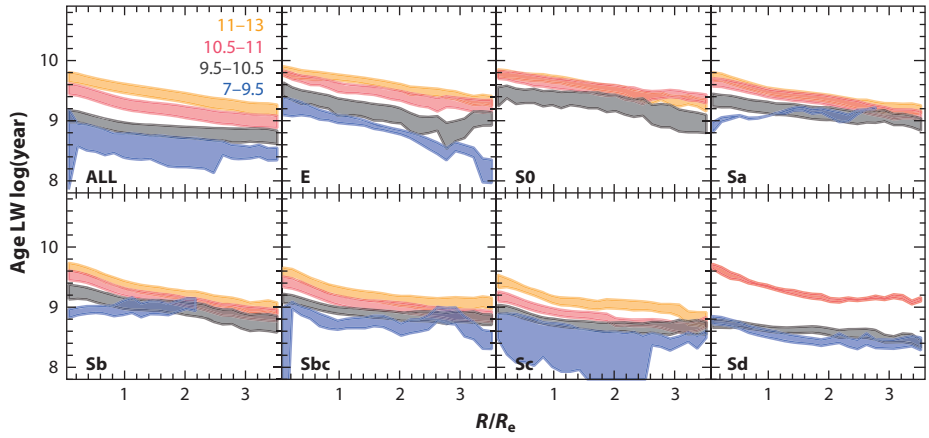

Figure 13

Azimuthally averaged radial distributions of the LW stellar ages for the galaxies in this review, segregated by stellar mass and morphology; colors and symbols have the same meanings as those in **Figure 12**. Abbreviation: LW, luminosity-weighted.

gradient in metallicity. These early results were revisited based on the analysis of larger samples of galaxies, using multi-broad-band photometry and long-slit and even IFS data (e.g., Mehlert et al. 2003; Sánchez-Blázquez et al. 2007; Rawle et al. 2008; Coccato et al. 2010; Kuntschner et al. 2010; Spolaor et al. 2010; Koleva et al. 2011; González Delgado et al. 2014b, 2015; McDermid et al. 2015; Ruiz-Lara et al. 2016; Goddard et al. 2017; Oyarzún et al. 2019). All these studies agreed in reports of a negative gradient in the stellar metallicity, [Z/H], but the consensus was less clear for the presence of a negative age gradient. Goddard et al. (2017) reported a flat or even a positive gradient in the stellar ages of early-type galaxies, explained by an outside-in scenario, based on data extracted from the primary sample of the MaNGA survey (reaching 1.5 R_e). Similar positive age gradients are sometimes described from analyses based on broad-band colors (e.g., Tortora et al. 2010). In spectroscopic-based studies, clear positive age gradients were found only in the very central regions ($\sim R_e/8$; Kuntschner 2015, McDermid et al. 2015). At larger scales ($>1.5\ R_e$), different authors have found contradictory results; they found a wide range of gradients, from negative to positive (e.g., Spolaor et al. 2010, Koleva et al. 2011); shallow negative gradients; or the absence of a gradient (e.g., Sánchez-Blázquez et al. 2007, Rawle et al. 2010). However, when the spectroscopic data reach the outer regions of galaxies ($R > 2\ R_e$), most of the studies report a negative gradient in the stellar ages, supporting an inside-out scenario (e.g., González Delgado et al. 2014b, 2015; Li et al. 2015; Zheng et al. 2017).

Figure 13 shows the radial gradients of the luminosity-weighted ages derived using our own analysis based on our compilation of IFS observations. For early-type galaxies of any mass there is a clear negative gradient, in agreement with most of the published results, although I should stress that there is no full consensus in this regard. The lack of consensus is deeply ingrained in the procedure adopted to derive the stellar ages. González Delgado et al. (2014b, 2015) used a full spectral fitting based on the `STARLIGHT` code (Cid Fernandes et al. 2011). This code, like `Pipe3D` (implemented in this review), uses the full optical spectral range and does not remove the shape of the spectral continuum (i.e., features like D4000 are important in that derivation), contrary to the one adopted by Goddard et al. (2017). Removing the shape of the continuum has strong implications, because the dust attenuation is no longer recovered (although not removing it requires a high-quality spectrophotometric calibration, as stated in Walcher et al. 2011). Recent

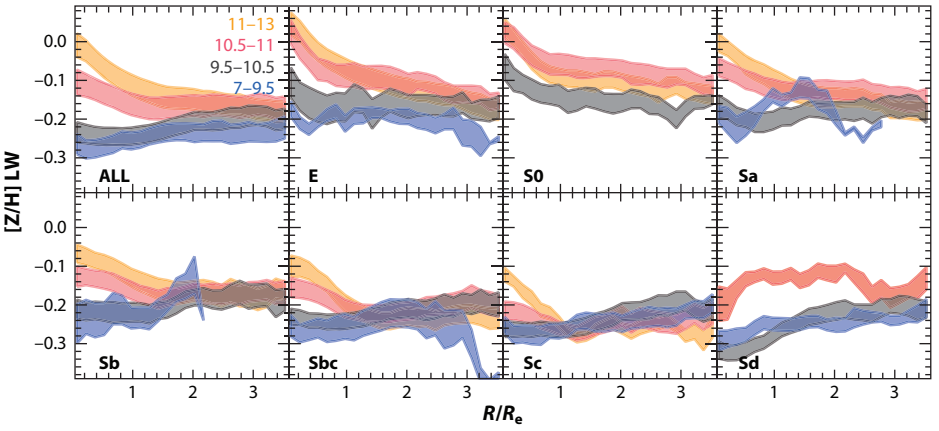

Figure 14

Azimuthally averaged radial distributions of the LW stellar metallicities ([Z/H]) for the galaxies considered in this review, segregated by stellar mass and morphology; colors and symbols have the same meanings as those in **Figure 12**. Abbreviation: LW, luminosity weighted.

results show that the polynomial functions adopted in some methods to describe and correct the shape are indeed very similar to the expected correction by a dust attenuation law (Belfiore et al. 2019b). Finally, I should note that the use of different wavelength ranges (e.g., ATLAS^{3D} covers just the wavelength range from 4800–5380 Å; Cappellari et al. 2011), or the inclusion or exclusion of the α-enhancement in the models, could contribute significantly to the reported differences.

The number of similar studies for LTGs is limited. This is mostly due to the difficulty of removing the emission lines that contaminate the spectra. This is particularly important in some spectral ranges, like those covered by the Balmer absorption lines (sensitive mostly to the age; e.g., Worthey 1994). Different fitting techniques have addressed this issue in different ways (e.g., Sarzi et al. 2006, Sánchez-Blázquez et al. 2014b, Sánchez et al. 2016b), efficiently removing this contamination. In this regard, the consensus is that the averaged ages of the stellar populations present a negative gradient for all LTGs more massive than $10^{9.5}$ $M_\odot$, with an almost similar slope (Sánchez-Blázquez et al. 2014a, González Delgado et al. 2015, Goddard et al. 2017, Ruiz-Lara et al. 2017). The stellar metallicity presents a negative gradient only for earlier-type spirals (Sa, Sb, Sbc) and more massive ones ($M_* > 10^{9.5}$ $M_\odot$), with a slope that becomes shallower for low-mass and LTGs. This is illustrated in **Figure 14**, which shows the radial gradients of the luminosity-weighted stellar metallicities derived for our data compilation. Again, these results agree with the scenario reviewed in Section 4.6, with an inside-out growth for more massive and earlier-type galaxies, and an outside-in growth for the less massive LTGs.

However, we should be cautious with the low-mass LTGs. For galaxies with strong SF with respect to their mass (i.e., the low-mass SFGs, mostly Sc and Sd, with high sSFRs) that are more metal poor (following the MZR), the estimation of age and metallicity is highly degenerated. The degeneracy between these two parameters is well known and widely studied (e.g., Walcher et al. 2011). However, in this range it is far more complicated: (*a*) The presence of strong emission lines on top of the Balmer absorptions, in combination with the fact that the spectral features are narrower owing to the combination of the type of stars and the low velocity dispersion, affects the accuracy in the removal of the contamination by the emission lines; (*b*) the absorptions by metallic elements are weaker than they are in the case of more massive galaxies, making it more difficult to obtain a precise metallicity; (*c*) this, in combination with the limited range of values for the 4000-Å

break when the light of the stellar population is dominated by young stars, affects the accuracy and precision in the derivation of both ages and metallicities.

R_{25}: radius of the elliptical isophote of a galaxy at which a surface brightness of 25 mag arcsec^2 in the V-band is reached

Characteristic gradient: oxygen abundances that have similar slopes in their gradients for disk galaxies with $M_* > 10^{9.5}$ M$_\odot$

4.7.3. Oxygen abundance gradients. Before stellar population analysis had enough accuracy to explore the metallicity gradients in SFGs, for decades, the study of the chemical enrichment was based in the analysis of the gas-phase abundance. In particular, HII regions have been considered good tracers of the chemical composition in these galaxies. It was in the 1970s that the presence of a negative abundance gradient across the disks of nearby galaxies had been uncovered (Searle 1971, Comte 1975), even in the Milky Way (Peimbert et al. 1978). This gradient has been confirmed by different observations (e.g., Matteucci & Francois 1989, Vila-Costas & Edmunds 1992, Martin & Roy 1994, Zaritsky et al. 1994, Esteban & García-Rojas 2018), and some deviations from this single negative gradient have been acknowledged (Belley & Roy 1992, Vilchez & Esteban 1996, Roy & Walsh 1997). Like in the case of other gradients explored in this review, the use of the effective radius as a scale length has helped to uncover the patterns and differences between galaxy types. Diaz (1989), and later Vila-Costas & Edmunds (1992), demonstrated that using a scale length anchored to the galaxy properties (like R_e and R_{25}), instead of a pure physical radial distance, reduces the scatter in the distribution of slopes of the abundance gradients. Following this philosophy, with the advent of large IFS observations, Sánchez et al. (2012a, 2014) showed that all SFGs more massive than $M_* > 10^{9.5}$ M$_\odot$ present a characteristic oxygen abundance gradient of $\sim$−0.1 dex/R_e when computed within the range 0.5–2.0 R_e (i.e., the disk region). Contrary to early results (e.g., Zaritsky et al. 1994), the slope of the gradient in this region is not strongly affected by other properties of the galaxy, like morphology or the presence of a bar. This result was confirmed also for the stellar metallicity (Sánchez-Blázquez et al. 2014a).

Besides the presence of a common/characteristic gradient, for some galaxies there is an apparent flattening or drop of the abundance in the central regions ($R < 0.5R_e$), and a flattening in the outer regions ($R > 2R_e$) in most of the cases. These results were confirmed using larger IFS data sets (e.g., Sánchez-Menguiano et al. 2016b, Zinchenko et al. 2016, Belfiore et al. 2017b, Pérez-Montero 2017, Poetrodjojo et al. 2018) or observations with exquisite spatial resolution (i.e., MUSE data; Sánchez-Menguiano et al. 2018). In other cases, no drop or flattening is appreciated at any scale, and a single slope for the abundance gradient reproduces the data well (Pilyugin et al. 2014). Some works described a continuous change in the abundance gradient from almost flat for low-mass galaxies ($M_* < 10^9$ M$_\odot$) toward the described characteristic slope, reached at $M_* \sim 10^9$ M$_\odot$ (Bresolin & Kennicutt 2015, Belfiore et al. 2017b). The actual selection of the SFAs used to derive the gradient may affect the results. For example, the inner drop is not detected when the SF/HII regions in the intermediate area between the Kauffmann and Kewley curves are excluded (e.g., Zinchenko et al. 2016). I should stress here that selecting only regions below the Kauffmann (or Kewley) curve may exclude SFAs with large forbidden line ratios (i.e., nitrogen enhanced), like the ones described in the inner region of galaxies by Kennicutt et al. (1989), Ho et al. (2014) and Sánchez et al. (2012a). The nature of those regions is still not clear, but they are easily identified as ionized nebulae in narrow-band images or emission-line maps based on IFS data.

Figure 15 shows the radial profiles of the oxygen abundance for the sample analyzed in this review, segregated by mass and morphology. These profiles reproduce the results reported in the literature well, in particular those by Sánchez-Menguiano et al. (2018). These authors presented the most detailed analysis so far on the shape of the abundance gradient. They used the super-high-resolution data obtained by MUSE on a sample of more than 100 galaxies, confirming that the slope of the abundance gradient in the disk regime is indeed very similar for all galaxies when the distribution is normalized to the effective radius (as suggested by Sánchez et al. 2014).

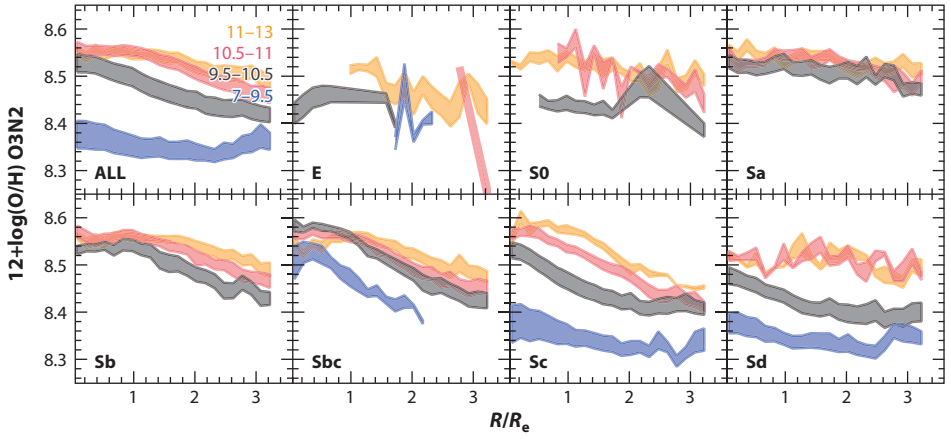

Figure 15

Azimuthally averaged radial distributions of the gas-phase oxygen abundances derived using the O3N2 calibrator for the galaxies considered in this review, segregated by stellar mass and morphology; colors and symbols have the same meanings as those in **Figure 12**.

Regarding the shape, it may present either a single slope or the combination of a monotonic decrease with an inner drop and/or an outer flattening. Sánchez-Menguiano et al. (2016b) and Belfiore et al. (2017b) already showed that the inner drop is ubiquitous in massive galaxies ($M_* > 10^{10}$ $M_\odot$) and not present in low-mass ones ($M_* < 10^{9.5}$ $M_\odot$). This is seen in **Figure 15**, particularly for Sb to Sc galaxies. The effect of radial migration toward the Lindblad resonances, or the freezing of the chemical enrichment associated with the quenching of the SF in the inner (bulge-dominated) regions, are plausible explanations for this deviation from the monotonic decrease. By contrast, the outer flattening does not have a clear pattern. The outer flattening is not directly connected with the shape of the SBP of disk galaxies (e.g., Marino et al. 2016). A change in the efficiency of the SF in the outer regions of the disk (e.g., Thilker et al. 2007), or outer radial migrations, are possible explanations for this change in the shape of the abundance gradient (e.g., Bresolin 2017). Sánchez-Menguiano et al. (2018) present the concept of a chemical-enrichment scale length in a galaxy ($R_{O/H}$), defined as the distance at which the oxygen abundance decreases by ~0.1 dex. They show that this parameter presents a linear and almost one-to-one correlation with the effective radius. This relation was already outlined by Bresolin & Kennicutt (2015), when they showed the relation between the slope (in physical scales for the galactocentric distances) and the scale length of the disk. As a consequence, when normalized by this scale length, the inner drop and the outer flattening happens virtually at $0.5R_{O/H}$ and $2.0R_{O/H}$ for all galaxies, with a very narrow scatter.

Some recent results have questioned the existence of a characteristic abundance gradient. Belfiore et al. (2017b), using data from the MaNGA survey, showed that for some O/H calibrators (Maiolino et al. 2008) there is a strong dependence of the gradient with the stellar mass, with low-mass galaxies ($M_* < 10^{9.5}$ $M_\odot$) presenting an almost flat abundance gradient. However, for other calibrators (Pettini & Pagel 2004) the distribution is consistent with a single slope for most of the galaxies. Poetrodjojo et al. (2018), using data from the SAMI survey, reported a weak trend with the mass only when using an R23-based oxygen abundance calibrator (like the one proposed in Maiolino et al. 2008). For other calibrators, they found an almost constant slope. Furthermore, as indicated above, the analysis by Sánchez-Menguiano et al. (2018), using MUSE data (with much better spatial resolution), does not provide any evidence of a dependence of the slope with M_*. In

the regime of low-mass galaxies (down to $M_* < 10^{8.5}$ $M_\odot$), the most recent explorations have not found any dependence with M_* either (Bresolin 2019). Thus, the possible dependence with the stellar mass has been reported only for low-mass galaxies, for particular calibrators, and using IFS data of low spatial resolution.

Secondary production: the production of elements that require preexisting seed nuclei, such as N (in some conditions) and some heavy elements

Primary production: the production of elements in stars derived directly from the original hydrogen, like C, O, and those in the iron-peak

The existence of a general rMZR, discussed in Section 4.4, can explain the observed oxygen abundance gradients in galaxies simply considering the existence of an inverse radial gradient in Σ_* (Section 4.7.1). Indeed, Barrera-Ballesteros et al. (2016) were able to reproduce not only the negative abundance gradient but also the characteristic slope of the gradient in disk galaxies ($\sim$−0.1 dex/R_e) assuming a universal rMZR and a radial decline of Σ_*. The small scatter in the rMZR relation ($\sim$0.05–0.07 dex) and the abundance gradients strongly supports the idea that oxygen chemical enrichment is dominated by local processes, being tightly related to the local SFH, without little effects of migrations or mixing beyond a few kiloparsecs. This supports the idea that the radial-mixing scale [introduced by Sánchez et al. (2015a) based on the scatter of the abundance gradient], the typical distance of oxygen abundance mixing in a galaxy, is rather small ($\sim$0.3–0.4 R_e).

In addition to the exploration of the radial gradient of the oxygen abundance, recent studies have focused on the exploration of possible azimuthal variations in the oxygen abundance. These variations could be induced by the nature of spiral arms as possible density waves, which may produce a differential SFH (e.g., Grand et al. 2016, Peterken et al. 2018) with respect to the rest of the disk, and introduce an azimuthal variation in the stellar or gas metallicity. Bars could also induce radial motions that produce azimuthal variations in these physical parameters (e.g., Athanassoula 1992, Minchev et al. 2012, Di Matteo et al. 2013). Pioneering observations have found that the abundance gradient shows subtle differences when the galaxy is divided in quadrants (Rosales-Ortega et al. 2011). More recent studies have found significant azimuthal variations in the oxygen abundance in a handful of galaxies (e.g., Li et al. 2013; Sánchez et al. 2015a; Sánchez-Menguiano et al. 2016a; Zinchenko et al. 2016; Ho et al. 2017, 2018; Vogt et al. 2017). However, when making a statistical analysis there are very few differences, even when considering barred and unbarred galaxies (Sánchez-Menguiano et al. 2016b, Zinchenko et al. 2016). An alternative interpretation is that the observed azimuthal variations are induced by the presence of anomalous abundance regions (Hwang et al. 2019), related more to gas inflow than to secular processes (Sánchez-Menguiano et al. 2019). In any case, azimuthal variations may be present in some galaxies induced by the combination of very particular dynamical processes or even external effects. However, azimuthal variations have a subtle effect in the radial abundance gradient (but not in the chemical distribution across the entire disk).

Although there are several studies of the oxygen abundance gradients in nearby SFGs, the systematic studies of nitrogen abundances (N/H) or nitrogen-to-oxygen abundances (N/O) are less numerous. In general, these studies have found a steady monotonic decrease of the N/O ratio from the inner to the outer regions (Pérez-Montero 2014, Belfiore et al. 2017b). There are no significant deviations from this pattern described in the literature. In general, it is accepted that most of the nitrogen observed in galaxies in the nearby Universe is due to secondary production, at least for galaxies more massive than $M_* > 10^{9.5}$ $M_\odot$. However, for earlier cosmological times and low-mass galaxies, its production may be the result of primary production. Thus, the N/O gradient follows the oxygen abundance gradient in general (e.g., Belfiore et al. 2017b).

4.7.4. Star-formation rate gradients. The presence of a monotonic decrease of the gas-phase oxygen and nitrogen abundances in (mostly disk) SFGs, described in the previous section, has been interpreted as direct evidence of an inside-out formation of these objects (Matteucci & Francois 1989, Boissier & Prantzos 1999). Under this scenario, the gradient is formed as a consequence of

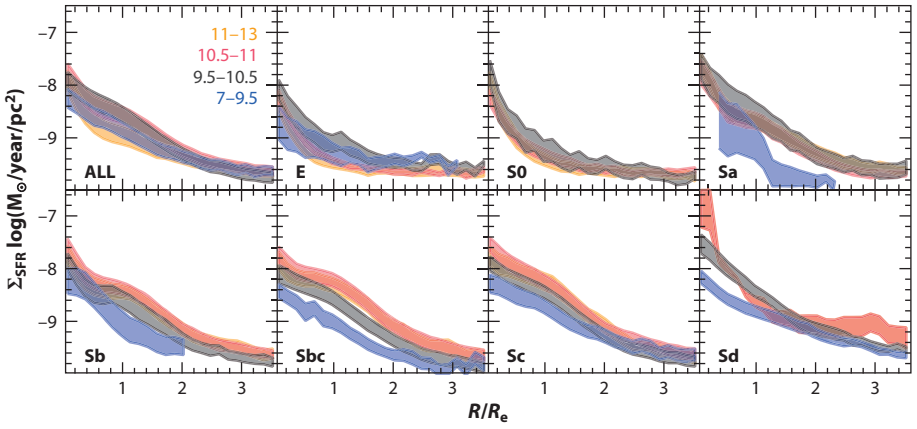

Figure 16

Azimuthally averaged radial distributions of the surface density of the SFR derived from the Hα intensity for the sample of galaxies considered in this review, segregated by stellar mass and morphology; colors and symbols have the same meanings as those in **Figure 12**. Abbreviation: SFR, star-formation rate.

the increased timescales of the gas infall with galactocentric distance. The differential amount of gas supply in the inner regions compared with that of the outer ones implies a differential SFR, assuming a constant or similar depletion time across the disk (i.e., a common SK law; Schmidt 1959, Kennicutt et al. 1989). The subsequent differential chemical enrichment naturally explains the oxygen (and nitrogen) abundance gradients. Most chemical abundance codes aiming to reproduce the described gradients, in particular those in our Galaxy, are based on this scheme on a first order (e.g., Mollá & Díaz 2005, Tissera et al. 2013, Carigi et al. 2019). In summary, this scenario predicts and requires the existence of a monotonic decrease of SF with the galactocentric distance.

Figure 16 shows the radial distribution of the SFR density (Σ_{SFR}). There is a clear peak in the central regions with a decrease toward the outer ones, which is broadly in agreement with the proposed inside-out scenario. González Delgado et al. (2016) conducted one of the first studies exploring the radial dependence of the SF with both the stellar mass and morphology of galaxies. They found results qualitatively similar to those presented here. Besides the radial decline in the Σ_{SFR} for all galaxies, early-type galaxies (E/S0) present, on average, lower values of SF than those seen in late-type counterparts at any stellar mass, for any galactocentric distance (which may not be true for individual galaxies). Thus, in these galaxies the decline of the SF happens at every radial distance. However, the maximum decline is found in the central regions. As already indicated in previous sections, the SF activity in early-type galaxies is a somewhat recent topic (see Section 4.1) being explored using IFS by a very small number of studies (e.g., Gomes et al. 2016b). In general, these galaxies host fewer SFAs, and those SFAs are forming stars at a lower rate with respect to those in LTGs (e.g., Cano-Díaz et al. 2019).

For LTGs, the most common morphological type among SFGs, Σ_{SFR} is 0.5–1 dex stronger than that of early types at any galactocentric distance. Among them, there is a clear variation with the stellar mass and the morphology: more massive and later LTGs present stronger SFRs. However, once normalized by the stellar mass density (Σ_*), the differences are less evident. **Figure 17** shows the radial distribution of the spatially resolved sSFRs ($= \frac{\Sigma_{SFR}}{\Sigma_*}$). For LTGs (from Sa to Sc), the sSFR presents a very similar value of about $\sim 10^{-11}$ year^{-1}, with a possible variation of ± 0.25 dex between earlier and later spirals (in agreement with González Delgado et al. 2016, Belfiore et al. 2018, and Sánchez et al. 2018). The sSFR has units of the inverse of time, and indeed its inverse

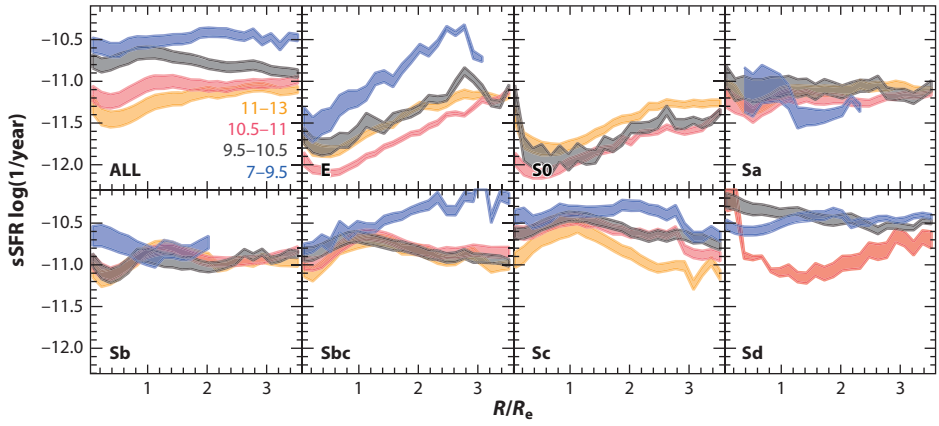

Figure 17

Azimuthally averaged radial distributions of the sSFR for the galaxies considered in this review, segregated by stellar mass and morphology; colors and symbols have the same meanings as those in **Figure 12**. Abbreviation: sSFR, specific star-formation rate.

could be interpreted as the amount of time required to form the current stellar mass at the current SFR (e.g., González Delgado et al. 2016). In purity, this is true if the current observed M_* is corrected by the mass locked in dead stars along cosmological times. However, that correction has a maximum of ∼30% for the adopted IMF (e.g., Courteau et al. 2014). Therefore, it does not significantly affect the order of magnitude of the estimation. This result indicates that at the current Σ_{SFR} galaxies would require hundreds of gigayears to form their current Σ_* (this is particularly true for the early-type galaxies). Thus, the SFR in the past must have been considerably higher than it is today, at any galactocentric distance. This is in agreement with the observations of the evolution of the SFR throughout time on the basis of integrated quantities (e.g., Speagle et al. 2014) or by the exploration of the cosmic SF density in the Universe (Madau & Dickinson 2014, Driver et al. 2018, Sánchez et al. 2019a).

The low dispersion of the sSFR at any galactocentric distance for (mostly star-forming) LTGs was interpreted by González Delgado et al. (2016) as being a direct consequence of the existence of the rSFMS. Comparing only the radial distributions of the two involved quantities, Σ_* (**Figure 12**) and Σ_{SFR} (**Figure 16**), an rSFMS should clearly hold. Contrary to LTGs, early-type (E/S0) galaxies exhibit a clear decrease of the sSFR toward the inner regions, at any mass, despite the peak observed in Σ_{SFR} for these galaxies. This has been interpreted by different authors as clear evidence of inside-out quenching (González Delgado et al. 2016, Belfiore et al. 2018, Lin et al. 2017, Ellison et al. 2018, Sánchez et al. 2018). This process is evidently related to the presence or influence of a bulge in the halting of the SF activity, either directly (e.g., Martig et al. 2009) or by hosting an AGN (e.g., Bell 2008). In terms of their distribution along the Σ_{SFR}–Σ_*, early-type galaxies, dominated by RAs, are located well below the loci of the rSFMS (Cano-Díaz et al. 2019; and **Figure 7**).

4.7.5. Gas-mass density gradients. The exploration of the radial distribution of Σ_{gas} and its connection with Σ_{SFR} (through the SFE) are giving us clues as to how the SF is maintained (or enhanced) and the reason for its quenching. In Section 4.5, I described the few cases of galaxies covered by IFS-GSs and spatially resolved molecular gas observations. Regarding the radial distribution, the molecular gas content peaks softly in the inner regions (Bolatto et al. 2017, Lin et al. 2017), with a more-or-less monotonic decrease from the central regions outward (e.g., Colombo

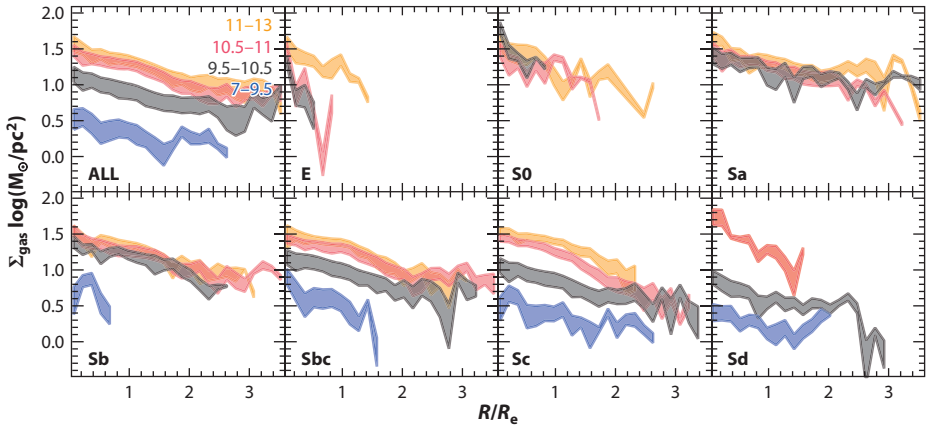

Figure 18

Azimuthally averaged radial distributions of the surface density of the gas mass, estimated based on the dust-to-gas ratio for the galaxies considered in this review, segregated by stellar mass and morphology; colors and symbols have the same meanings as those in **Figure 12**.

et al. 2018, their figure 4), with a scale length (effective or half-light radius) that matches well that of the stellar light (e.g., Bolatto et al. 2017, their figure 13), confirming the results by previous studies (Regan et al. 2001, Davis et al. 2013). **Figure 18** shows the radial distribution of the molecular gas surface density derived using the dust-to-gas proxy described before (Section 4.5) for the well-resolved galaxies in our IFS compilation. The general radial decline reported in the literature is clearly reproduced.

I segregate the radial distributions by stellar mass and morphology, following the scheme of previous figures. In general, the gas surface density strongly depends on the total stellar mass for LTGs (e.g., Saintonge et al. 2011). However, for early-type galaxies (E, S0, and Sa), there is no clear trend with the mass, in agreement with the results by Young et al. (2011). In addition, for the same mass, galaxies of different morphology present similar radial gradients of Σ_{gas}, as reported by Colombo et al. (2018). Finally, the molecular gas fraction decreases for earlier and more massive galaxies. This decline is stronger in the inner regions, as is evident when comparing the distributions shown in **Figures 12** and **18**. This indicates that the observed decline in the sSFR from the inside out (**Figure 17**) is due primarily to a relative lack of molecular gas. However, a change in the SFE plays a role too.

Utomo et al. (2017) found that, on average, the radial distribution of the depletion time τ_d (the inverse of the SFE) is rather flat when analyzed spaxel by spaxel at a kiloparsec scale. However, this quantity presents a clear radial trend, when radial averages by galaxy morphological type are considered (Colombo et al. 2018). In the inner regions, τ_d has lower values, of the order of $\sim$1 Gyr (SFE $\sim 10^{-9}$ year^{-1}), and up to $\sim$10–20 Gyr (SFE $\sim 10^{-10.5}$ year^{-1}) in the outer ones, with a clear segregation by mass and morphology (e.g., Colombo et al. 2018, their figure 4). Despite the different proxies adopted to derive the molecular gas mass (dust attenuation versus CO observations), similar results are recovered for our data set. **Figure 19** shows the radial distribution of the SFE segregated by stellar mass and morphology. The monotonic decrease from the center outward is clearly shown, with more massive galaxies presenting lower SFEs (larger τ_d) than less massive galaxies. When segregating by morphology, the picture is less clear. Whereas for some morphological types (e.g., E or Sc) there is still a segregation by mass, for other ones (e.g., S0 or Sbc) its seems that all galaxies have a similar SFE distribution irrespective of their mass, without a

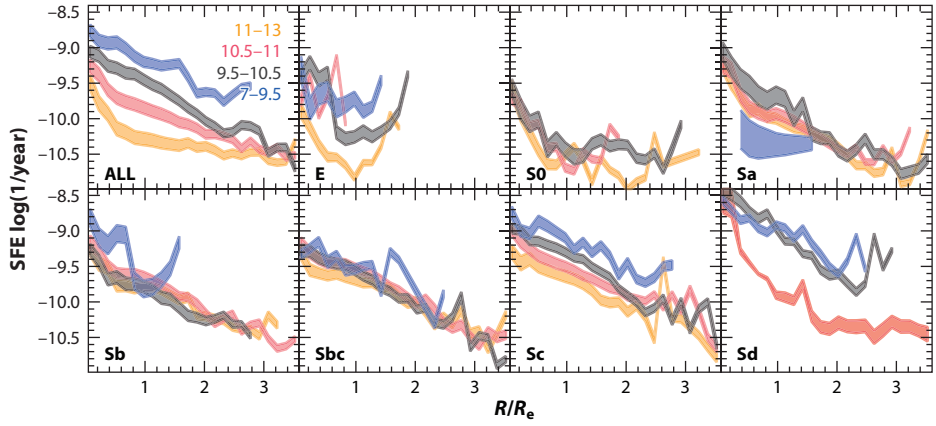

Figure 19

Azimuthally averaged radial distributions of the SFE for the galaxies considered in this review, segregated by stellar mass and morphology; colors and symbols have the same meanings as those in **Figure 12**. Abbreviation: SFE, star-formation efficiency.

clear pattern. However, when comparing galaxies of different morphology but of the same stellar mass, the trend is clear: In general, LTGs present larger SFEs (shorter τ_d) than do earlier ones, at any galactocentric distance. Recent results (Ellison et al. 2020) indicate that this change in the SFE is one of the causes of the dispersion in the rSFMS, which can be observed as a segregation by morphology (e.g., Cano-Díaz et al. 2019). If τ_d is interpreted as the time required to consume the current molecular gas mass with the current SFR, then this time is shorter in the inner regions of less massive and later galaxies and in the outer regions of more massive and earlier galaxies.

I note that the reported distributions may change in the presence of bars, which are known to induce radial movements of gas (e.g., Shlosman et al. 1989, Boone et al. 2007, Knapen et al. 2019). In particular, they can produce an increase of the molecular gas and even the SFE in the inner regions of galaxies (in contrast with results found in this review).

5. WHAT WE HAVE LEARNED

In this review, I summarize the most recent results in the characterization of the spatially resolved spectroscopic properties of galaxies in the nearby Universe ($z < 0.1$). To do so, I compile the largest possible sample of galaxy data observed using optical IFS and replicate the published results (to a certain extent).

In summary, recent results have found that the evolution of galaxies is governed by local properties but influenced somehow by global ones. The duty cycle of gas to stars, the chemical enrichment, and the quenching and halting of both follow local/spatially resolved scaling/evolutionary laws that are verified at kiloparsec scales in galaxies. Among them, the SK law and rSFMS and rMZR relations, verified for SFAs in galaxies, are followed by regions of different galaxies that to some extent follow the same resolved SFHs and ChEHs. These evolutionary sequences depend on the galactocentric distance, the stellar mass, and the morphology, indicating that most probably they actually depend on the local strength of the gravitational potential and the dynamical/orbital structure. The central regions of more massive and earlier-type galaxies evolve faster, showing sharper SFHs; are initiated by a steady and rapid increase of the SFR, which lasts less than 1 Gyr; and reach a peak that is followed by a sharp decay. The outer regions of less massive LTGs evolve in a slower fashion, with smoother SFHs; they are initiated with a slow increase of the SFR,

reaching its peak of SF at much more recent cosmological times (in some cases, they are still in the rising phase of SF). This, together with a narrow range of depletion times (within a factor of ~2) across galaxy types, galactocentric distances, and final stellar masses, explains the observed local relations.

The SFH defines to a great extent the ChEH, which in general is governed by local processes, with recycling, inflow, and outflow happening more at local than at global scales. The SFHs and ChEHs shape (or are shaped by) the scaling relations indicated previously, which evolve with cosmological times (in the case of the rSFMS and rMZR) or are rather constant (SK law). Above the kiloparsec scale, integrated/averaged through the optical extension of galaxies, the local/resolved relations are observed as global ones (SFMS, MZR). In some cases, depending on the fraction of regions actually forming stars within a galaxy, the global relations may present shallower relations than the local ones (e.g., SFMS versus rSFMS). However, not all global relations are induced by local ones. This is the case with the stellar MZR, which relates the average [Z/H] and the stellar mass. There is no parallel Σ_*–[Z/H], because the stellar metallicity depends on both the amount of generated stars and the way that these stars are formed, i.e., both the strength and shape of the SFH. Furthermore, a certain time is required before intermediate-mass stars pollute the ISM with non-α (Fe-like) elements, and therefore, different SFHs leading to the same Σ_* imply different [Z/H] values.

The described resolved relations shape the radial gradients observed in many different quantities, as a pure consequence of the radial gradient of Σ_*, which is formed in early cosmological times. The early evolution is dominated by the trigger of SF happening at the same time across galaxies, consuming the gas reservoir that is larger in the central regions by a pure effect of the shape of the gravitational potential. The ignition of the SF, following an SK law shaped by the free-fall time of collapsing molecular clouds, automatically creates a radial gradient in Σ_*. Due to the local relations indicated previously and the differential evolution of the stellar populations (formed faster and earlier in the central regions of more massive galaxies), the observed properties of galaxies present clear radial gradients, with central regions having older and more metal-rich stellar populations, higher rates of SF, and more metal-rich gas. In general, the evolution of galaxies is governed by an inside-out growth during most of their lifetimes.

This evolution is verified for galaxies with a stellar mass of $M_* > 10^{9.5}$ $M_\odot$. Below that mass most of the regions at any galactocentric distance are still in the rising phase of their SFHs, and therefore their chemical enrichment is slightly different, presenting flatter oxygen abundance gradients and even inverse stellar metallicity gradients. If this evolution is scaled toward higher redshifts for more massive galaxies, it may indicate that the very early phase of the evolution of galaxies had an outside-in growth phase, which is shorter for massive galaxies, and it has left almost no trace in the current fossil record. It is possible that the outer regions of massive galaxies are still in this evolutionary phase, which may explain the flattening of some observed gradients in external regions of galaxies. I speculate here that the transition happens in the regime in which the infalling gas is of the same order as the original reservoir, which keeps the SFHs in a continuous (but smooth) rising phase.

The lack of (molecular) gas is the main driver for halting the SF activity, triggering a quenching that also evolves from the inside out. In other words, the central regions of more massive galaxies, which have followed the sharpest SFHs, exhaust the cold gas earlier than do the outer regions of less massive ones. In addition, there is a decline in the SFE, related to dynamical effects (i.e., a shift from a pure SK law). It may well be that AGN feedback is the main driver for the absence of the SF fuel, due to either physical removal or heating beyond the cooling timescales. However, the dynamical effects introduced by the bulge dynamics seem to maintain the effects of the quenching for longer periods.

One of the main outcomes of large explorations of galaxy properties using IFS is that most galaxies present many different ionization processes at different locations. Thus, we should consider and study ionization as a local process. A fraction of galaxies may present AGN activity that could ionize (mostly) the central regions. But this does not preclude them from presenting SF activity in the disk, which produces a different kind of ionization. Central outflows, usually associated with shock ionization, could be observed in galaxies hosting an AGN or galaxies with strong nuclear SF activity. Even more, it is now clear that LINER-like emission is not dominated by weak AGNs, as was commonly assumed for decades (although ionization by weak AGNs may also be present in some of them). The most probable reason for this kind of ionization, observed as diffuse ionized gas, is the presence of sufficiently old stellar populations (older than 1.6 Gyr, on average). However, in the case of radio galaxies, shock ionization may be a significant contribution to the ionization (i.e., the so-called red geysers). But they represent less than 1% of the total number of galaxies. Finally, in a very few cases, collimated synchrotron radiation associated with radio jets could be sufficiently energetic to ionize the ISM (e.g., 3C120, M87). Altogether, the description of the ionization stage of a galaxy using only global properties (e.g., average line ratios) is fundamentally wrong. It has a pure statistical meaning that is true only if there is a single ionization process that clearly dominates over the remaining ones. Particular care should be taken in the interpretation of the classical diagnostic diagrams, which make little sense unless they are combined with the properties of the underlying continuum (stellar population, mostly). If not, they may lead to fundamental mistakes.

Finally, despite recent advances, there are caveats to the emerging picture. First, we have limited knowledge of the atomic and molecular gas content at the same spatial scales explored using the most recent optical IFS-GSs (thus, covering a wide range of integrated properties as stellar masses and/or morphologies). Despite the individual efforts on a handful of targets (e.g., Lin et al. 2017) or pioneering explorations in large samples (e.g., Davis et al. 2013, Bolatto et al. 2017), there is still a need for a comprehensive exploration of the HI and H2 distribution at a kiloparsec scale for samples of galaxies already observed using IFS. Current instruments, like the Very Large Array, could easily be used to accomplish such exploration for the atomic gas for those samples at low redshifts (AMUSING++, CALIFA, and the lower-redshift targets of the MaNGA and SAMI surveys). For the molecular gas, the Atacama Large Millimeter Array (ALMA) would be ideal, particularly considering that the FoV of this instrument matches pretty well that of MUSE and the optical extension of the galaxies of some of the quoted IFS-GSs (e.g., CALIFA, whose diameter selection matches the FoV of ALMA). In other cases, like MaNGA or SAMI, the FoV of ALMA is considerably larger, and therefore there is no perfect match of the covered regime between both observations. The lack of this data sets limits on our knowledge of the gas-to-stars duty cycle and our understanding of the feedback and quenching processes.

Second, we still do not know the real nature of the scaling relations. So far, we know that they are verified at kiloparsec scales, and we also know that they break at lower scales. SF and chemical enrichment are very local processes, and at the scale of an individual HII region these scaling relations are clearly not verified. This indicates that they have a statistical nature and are only verified at certain volumes and timescales: (*a*) volumes in which the integrated molecular and stellar masses are big enough to average the physical processes and (*b*) timescales sufficiently long to compensate the instant SF with the metal mixing and stellar feedback, in different locations within the area (or volume) considered. Thus, the SF and chemical enrichment are the result of physical processes that indeed do not verify those scaling relations. Optical IFS-GSs exploring galaxies at much smaller physical scales (like PHANGS; Rosolowsky et al. 2019) may tackle this problem in the near future. Following this reasoning, the derived SFHs and ChEHs also have a statistical nature, reflecting the envelope evolution of more pseudostochastic processes. In other

words, the SFHs at lower scales do not present the described patterns, being dominated by peaks of SF that reflect the single events observed as individual HII regions.

Third, we need to extend our explorations to different wavelength ranges to improve our understanding of the properties of the stellar populations and the ionized gas. In particular, the combination of UV and far-IR data with the information provided by IFS is a promising tool to improve our estimations of the resolved SFHs and ChEHs (following López Fernández et al. 2018). So far, we are limited by the coarse spatial resolution of the data in these wavelength ranges.

Fourth, we lack of a detailed knowledge of the AGN feedback and its connection with the bulge growth to the extent that we could explain the quenching using simple causal connections. We do not know whether the effect is purely mechanical (gas removal) or thermal (gas heating), or a combination of both and to what extent. We also do not know which frequency is required to sustain the quenching or if it is a single event process, supported by other processes (like bulge-induced dynamical effects). Actually, we do not know which is the real mechanism that makes bulges grow in time in sufficient detail.

Fifth, we need to extend our current IFS explorations to larger samples at higher redshifts in order to study the evolution of the observed quantities and to determine whether our inferences based on the fossil records are compatible with observations. This would require new instruments still not foreseen or those installed in new facilities (like the IFS at the *James Webb Space Telescope*).

Finally, an effort should be made to develop detailed hydrodynamical and *N*-body simulations, with more precise recipes of the feedback, to a resolution good enough for comparisons with the current and future data sets. Little has been done to reproduce simultaneously the spatially resolved and integrated scaling relations observed in galaxies using simulations to the extent that we can understand the physical processes better, following, for instance, Trayford & Schaye (2019) and van de Sande et al. (2019).

In summary, the most recent results based (mainly) on optical IFS-GS data and their combination with spatially resolved information of the cold gas content have improved our understanding of the interconnections among SF, chemical enrichment, and stellar evolution in general. New patterns and scaling relations have been uncovered, particularly at kiloparsec scales. In addition, previously known patterns and scaling relations have been reinterpreted, mostly global scaling relations. However, there is still a vast number of unsolved problems that would require new data, new techniques, and a deeper interexchange and cross-talk between observational and theoretical studies. As frequently happens in any branch of knowledge, new answers have led to new questions that require further explorations in the coming years.

APPENDIX A. INTEGRAL FIELD SPECTROSCOPY GALAXY SURVEYS

This review is focused on the most recent results on the spatially resolved properties of galaxies derived using mostly IFS. IFS is the technique that allows us to simultaneously obtain several spectra (within a defined FoV) of a quasi-continuous region in the sky. So, the final data, after reduction, consist of either a spatially continuous distribution of spectra (3D cube) or a set of individual spectra arranged across the FoV in certain fixed positions. It is beyond the scope of this review to discuss the details of the IFS technique, explaining the differences between the several IFUs or the data acquisition, reduction, and analysis of this particular type of data. For these details, I refer readers to Bershady (2009) and more extensively to the book published by Bacon & Monnet (2017). However, I include in this review a brief description of the IFS technique, since most of the reviewed results are based on optical IFS.

IFS is not a totally new technique, with early experiments already presented in the 1980s (e.g., Vanderriest et al. 1987). For years it was used to explore in detail the spatially resolved

spectroscopic properties of a single object (or a handful of them). In the particular case of the study of galaxy properties, the stellar and gas kinematics, together with the exploration of ionization conditions in different regions, were more frequently the targets of this technique (e.g., García-Lorenzo et al. 1997). The computational complexity of the data reduction and analysis hampered the development of IFS as a common-user technique for decades, excluding its use for large samples of galaxies. Collective efforts (like the Euro3D Research Training Network; Roth 2006), inspiring small-group initiatives (like the SAURON project; Bacon et al. 2001), and the growth of computational capabilities through the years allowed the implementation of IFS as a common-user technique and extended its use as a survey mode tool.

The SAURON project is usually considered the first attempt to perform an IFS galaxy survey (de Zeeuw et al. 2002). It explored the central regions of a representative sample of 72 early-type galaxies (E/S0/Sa) in the nearby Universe (<42 Mpc; de Zeeuw et al. 2002). The path opened by this project was continued by ATLAS^{3D} (Cappellari et al. 2011), the real first IFS-GS. It uses the same instrument as did SAURON to study the central regions ($R < 1.5\ R_e$) of a volume-limited sample of 260 galaxies of the same morphological type and at the same cosmological distances. Both projects explored mostly the properties of the stellar populations in early-type galaxies and bulges of early spirals (e.g., Emsellem et al. 2004, Ganda et al. 2006), studying their dynamics, stellar composition, and, to a lesser extent, the ionized gas properties (e.g., Kuntschner et al. 2010, Sarzi et al. 2010). Most of the results from both surveys were recently reviewed by Cappellari (2016).

The exploration of LTGs by IFS-GSs started later. One major problem that delayed these studies was the presence of ionized gas throughout the disk of these objects. This created an additional technical complication because it is required the separation of the stellar and gas components in the analysis (e.g., Sánchez-Blázquez et al. 2011). Pioneering projects in the exploration of spiral galaxies by IFS surveys were (*a*) the Disk Mass Survey (Bershady et al. 2010); (*b*) the exploration of galactic winds by Sharp & Bland-Hawthorn (2010); (*c*) the PINGS survey (Rosales-Ortega et al. 2010); (*d*) the VENGA project (Blanc et al. 2010); and (*e*) the CALIFA pilot survey (Mármol-Queraltó et al. 2011). Most of these were focused on the study of the ionized gas, and, in some cases, of the stellar populations, tending particularly toward the stellar/gas dynamics. I do not discuss here explorations at high redshift, which are beyond the scope of this review.

None of those pioneering surveys explored a wide range of galaxy properties, including all morphological types and/or covering a wide mass/luminosity/color regime, and in a statistically large sample of galaxies (e.g., ATLAS^{3D} observed only E/S0 and red early spirals). The first IFS-GS fully representative of the population of galaxies in the near Universe was the CALIFA survey, started in 2010 (Sánchez et al. 2012a). Furthermore, CALIFA was the first IFS-GS designed as a legacy survey, i.e., with the main and primary goal of delivering the data freely to the community in a form that was easily accessible and fully documented. Soon after, two major IFS-GSs were launched (and are still ongoing) following the same philosophy: MaNGA (Bundy et al. 2015) and SAMI (Croom et al. 2012). It is beyond the scope of this review to make a detailed comparison between them (see, e.g., Sánchez 2015 and Sánchez et al. 2017). I briefly summarize here their main properties, which are also listed in **Table 1**. CALIFA offers the best compromise among spatial resolution, covered fraction of the galaxy extension, and number of sampled elements. However, this comes at a cost because of sampling of a much lower number of galaxies than MaNGA (one-tenth) and SAMI (one-third). Thus, for detailed analyses of the

Table 1 Summary of the main properties of different IFS-GSs

Parameter	MaNGA	SAMI	CALIFA	AMUSING++
Current sample size	6,850	2,400	974	540
Selection	M_* flat distribution	Volume limited	Diameter	Compilation
Redshift range	0.01–0.15	0.01–0.1	0.005–0.03	0.001–0.1
Mean redshift	0.03	0.04	0.015	0.017
Maximum galactic radius sampled	1.5 R_e (2/3), 2.5 R_e (1/3)	∼1 R_e	>2.5 R_e	>2 R_e
Diameter of FoV	32 arcsec[a]	16 arcsec	74 arcsec	60 arcsec
S/N at 1 R_e per spaxel	20	10	50	5
S/N at 1 R_e per arcsec	40	20	50	25
Wavelength range (Å)	3600–10300	3700–5700/6250–7350	3700–7500	4650–9300
Original sampling elements	3 × 127[b]	n × 61[c]	3 ×331	90,000
Spectral resolution (σ)	80 km s^{-1}	75/28 km s^{-1}	85/150 km s^{-1}	40 km s^{-1}
Spatial resolution (FWHM)	2.5 arcsec	2.3 arcsec	2.4 arcsec	∼ 0.7 arcsec
Physical spatial resolution (kpc)	2.5 [0.5, 6.5]	2.2 [0.4, 4.6]	0.8 [0.3, 1.5]	0.3 [0.1, 1.3]
Telescope size	2.5 m	3.6 m	3.5 m	8.2 m
Telescope name	SDSS	AAT	CAHA	VLT
Galaxies in sample	4,651	2,222	868	435
Galaxies with morphology	2,593	2,109	625	310
Galaxies in resolved sample	720	0[d]	520	254

Abbreviations: AAT, Anglo-Australian Telescope; CAHA, Centro Astronómico Hispano Alemán; FoV, field of view; IFS-GSs, integral field spectroscopy–galaxy surveys; IFU, integral field unit; MaNGA, Mapping Nearby Galaxies at Apache Point Observatory; SAMI, Sydney-Australian-Astronomical-Observatory Multi-object IFS; SDSS, Sloan Digital Sky Survey; VLT, Very Large Telescope.

[a]This corresponds to the largest MaNGA bundle. Each MaNGA plate provides 17 bundles of different hexagonal FoVs. The smallest covers 12 arcsec in diameter.

[b]This corresponds to the largest MaNGA bundle. Each MaNGA plate provides 17 bundles of different amounts of fibers: 2 × 19, 4 × 37, 4 × 61, 2 × 91, and 5 × 127.

[c]The dithering scheme in SAMI is repeated until a certain S/N ratio is reached. Therefore, the number of independent sampling elements is variable from target to target.

[d]Excluded due to the FoV of the SAMI IFU.

spatially resolved properties, CALIFA may present an advantage. However, for galaxy statistics, MaNGA is far superior. MaNGA also offers a wider wavelength range and slightly better spectral resolution. Finally, although SAMI offers the smallest FoV (and covered area of each galaxy), it has by far the highest spectral resolution (in the red wavelength range). Thus, for kinematics (particularly gas kinematics) it provides more precise estimations. In general, the three IFS-GSs are pretty complementary, compensating for the limitations and strengths of each other.

In addition to these three major IFS-GSs, I include in **Table 1** a large compilation of IFS observations of galaxies in the nearby Universe performed with MUSE (Bacon et al. 2010). This instrument is the IFS that offers the best compromise among spatial sampling, resolution, FoV, spectral resolution, and collecting power by far. The only drawback it presents is that of a limited wavelength range in the blue optical range (cut at 4650 Å), which strongly affects any analysis of the stellar populations at low redshift. The current compilation, named AMUSING++ (López-Cobá et al. 2020), involves a diameter selection (1 R_e < FoV < 3 R_e) of galaxies included in the European Southern Observatory archive corresponding to different projects (e.g., MAD, GASP,

TIMER, PHANGS, and AMUSING; Galbany et al. 2016, Kreckel et al. 2017, Poggianti et al. 2017, Erroz-Ferrer et al. 2019, Gadotti et al. 2019). Two-thirds of the objects are extracted from the AMUSING survey (PI: J. Anderson), which was already used in different studies (e.g., Sánchez et al. 2015a; Sánchez-Menguiano et al. 2016b, 2018; López-Cobá et al. 2017a; Galbany et al. 2018). It is by far the largest compilation of IFU data with the best possible spatial resolution. It was included in the compilation of data for completeness and to highlight what would be achieved in the near future when such new instruments would be used in a survey mode.

I compiled all the publicly available data from all these IFS-GSs (and compilations) to reproduce the main results reviewed throughout this article (as indicated in Section 2), restricted to a maximum redshift of $z < 0.02$. This compilation comprises a total number of 8,177 galaxies (and datacubes). This way, I expect to minimize the possible biases introduced by the particularities of sample selection and instrumental details of each IFS-GS. The number of galaxies corresponding to each survey included in this compilation is listed in **Table 1**. In addition, I obtained the morphological classification for two-thirds of them, using public information from different sources (HyperLeda for MUSE: Walcher et al. 2014, Sánchez et al. 2018; L. Cortese for SAMI, private communication). For the particular purpose of this review I selected the best resolved and sampled galaxies, as indicated in Section 2 (i.e., the well-resolved subsample).

It is clear that the current compilation does not comprise a well-defined sample of galaxies (in principle). However, it is broadly representative of the general population of galaxies in the considered redshift range, because it was created from samples that are indeed representatives themselves. **Figure 20** shows the distribution of colors (*B*–*R*), effective radii, and redshifts along the *R*-band absolute magnitudes for the full compilation of galaxies (and segregated by morphology). Features such as the red sequence (for E/S0) and the blue cloud (for Sc/Sd) are nicely recovered. Indeed, the morphological distribution is similar to that recovered by volume-limited surveys, with ∼33% of early-type galaxies (E/S0), ∼40% of early-spirals (Sa/Sb), and ∼27% of late spirals (Sc/Sd; e.g., Bamford et al. 2009). The fractions of SFGs (∼50%), RGs (∼46%), and AGN hosts (∼4%) are also consistent with the most recent estimations at the considered redshift range (e.g., Cano-Díaz et al. 2016, and references therein). The distribution along the R_e–$M_{abs,\,R}$ plane follows the expected trends for both the full population and the different morphological types (e.g., Cappellari 2016). Finally, the redshift–$M_{abs,\,R}$ distribution (and that of the derived redshift–R_e) resembles that of a diameter-selected sample. These may or may not be the primary selection criteria of the different IFS-GSs included in this compilation, but they all aim to have their targets fit within the FoV of their IFUs (to a certain stage). In **Figure 20**, the two distinctive distributions correspond to the CALIFA/AMUSING++ and the MaNGA/SAMI subsamples, which cover two clearly different redshift ranges in general (see **Table 1**).

Figure 20 also shows the distributions for the well-resolved subsample (defined in Section 2). In general, it presents a similar distribution rather than the full compilation for the parameters analyzed here. The strongest difference is the cut at low luminosity and blue colors, which corresponds in general to the tail toward low-mass galaxies included in the SAMI sample but is not well covered by other IFS-GS (e.g., Sánchez et al. 2017). However, excluding dwarf galaxies (not included in the current review), the two samples cover a similar range of parameters. Furthermore, both of them are representative of the global population of galaxies in the nearby Universe (at a first order). As expected, the number of galaxies in the considered compilation is clearly dominated by the publicly available data from the MaNGA IFS-GS (DR15; Aguado et al. 2019), comprising ∼57% of those

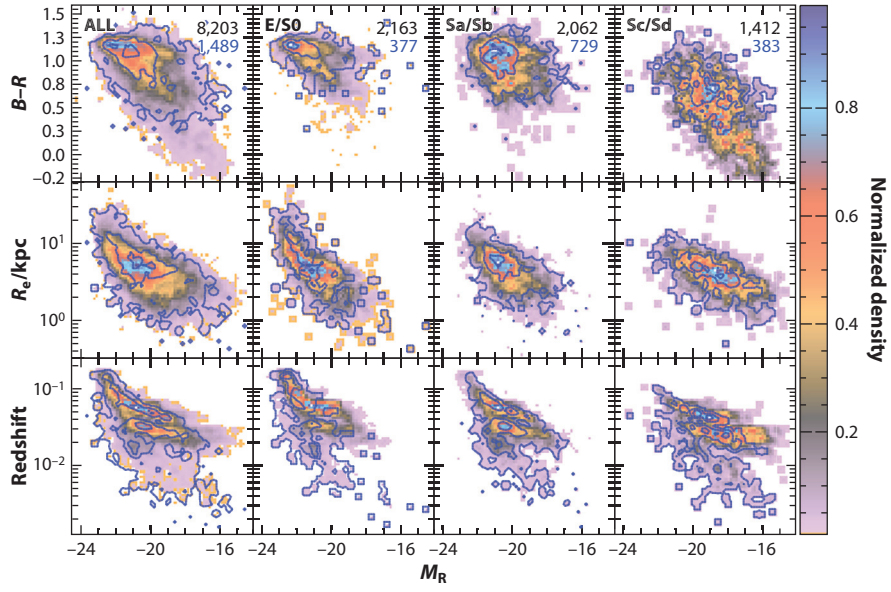

Figure 20

The distribution of colors (*B–R*, *top row*), effective radii (*middle row*), and redshifts (*bottom row*) for the *R*-band absolute magnitudes for the collection of galaxies with IFS observations used in this review. Panels in the far-left column show the distribution for the full sample of galaxies considered in this review, and each consecutive panel from left to right shows similar distributions segregated by morphology (with the morphology indicated in the *top panels*). Color maps show the density distribution normalized to the peak density for the full compilation, whereas contours show the same distribution for the subsample of well-resolved galaxies. Contours include 90%, 50%, and 10% of the points. Finally, the number of galaxies included is indicated in the top panels, in black for the full sample and in blue for the well-resolved one.

galaxies (**Table 1**). However, only half of them have publicly available morphology, and just ∼15% fulfill our strict criteria for the well-resolved subsample. These cuts exclude all the SAMI data as well, because I impose a minimum galaxy size of larger than the FoV of their IFUs. These are arbitrary criteria, aiming to recover only the best sampled and resolved IFS data and to homogenize the different data sets. They do not imply any judgement on the quality of the different IFS-GS data sets, considering their different goals and scopes. Further details of the compilation and its main global properties are provided elsewhere (S.F. Sánchez & C. López-Cobá, in preparation).

APPENDIX B. IONIZED GAS: A PRACTICAL CLASSIFICATION SCHEME

Based on the different results discussed in this review, I present the following practical classification scheme to distinguish between different kinds of ionizing sources, particularly for IFS data at ∼1-kpc resolution:

- **A star-forming or HII region:** It is a clumpy area (clustered) in a galaxy in which the ionized gas emission-line ratios are below the Kewley et al. (2001) demarcation line in at least one of the classical diagnostic diagrams involving [OIII/Hβ] versus [NII]/Hα, [SII]/Hα, or [OI/Hα], with EW(Hα) above 6 Å and with a fraction of young stars (age < 100 Myr) in flux in the visual band of at least 4–10%.

Red geyser: elliptical galaxy with filamentary ionized gas most probably due to shocks, but not clearly related to high-speed outflows

- **An AGN-ionized region:** It is a central ionized region, clearly more intense than the diffuse ionized gas, in which the emission-line ratios are above the Kewley et al. (2001) demarcation line in **Figures 1**, **4**, and **5** with EW(Hα) above 3 Å. Below that limit it is not possible to determine whether the ionization is due to an AGN or to other processes. The line ratios decrease with respect to the center of the galaxy, and the flux decays at r^{-2} or faster (not following the light surface brightness of the continuum).
- **Diffuse gas ionized by old stars (HOLMES, post-AGBs):** It is a smooth ionized structure that follows the light distribution of the old stellar population in galaxies, presenting an EW(Hα) clearly below 3 Å. The fraction of young stars for the underlying stellar population is never larger than 4% (in the *V*-band). It does not present any clumpy or filamentary distribution. In the BPT diagram, it could be located covering the LINER-like region (or AGN locus) toward the location of metal-rich SFAs. It is present in galaxies with old stellar populations (massive, earlier types) or regions in galaxies with the same characteristics (bulges), and it shares the same kinematic structure as the old stellar population.
- **Diffuse gas due to photon-leaking by HII regions:** They are smooth ionized structures present in galaxies with young stellar populations (in general, low-mass LTGs) or regions in galaxies with the same characteristics (disks), presenting an EW(Hα) below 3 Å, with a fraction of young stars that is never larger than 4% (in the *V*-band). It shares the same location as classical HII regions in the diagnostic diagrams and should be included in the photon budget to derive the SFR in galaxies. Its kinematics is not fundamentally different from that of the disk. In high spatial resolution data (10–100 pc), it may present some shells or bubble-like structures that are not visible at kiloparsec scales.
- **A high-velocity shock-ionized region:** It is a filamentary or biconical ionized gas structure with an intensity stronger than that of the diffuse ionized gas. The emission-line ratios are above the Kewley et al. (2001) demarcation line in **Figures 1**, **4**, and **5** with an EW(Hα) above 3 Å. It shows asymmetrical lines extended through the filamentary structure. Most cases are associated with galactic outflows. It demonstrates a clear increase of the considered line ratios (in particular [OI/Hα]) with the velocity dispersion and the distance from the source of the outflow. AGN and SF-driven outflows could be separated, in principle, using the demarcation line proposed by Bland-Hawthorn (1995).
- **A low-velocity shock-ionized region:** It shares many of the characteristics of the diffuse gas ionized by old stars, and indeed it is considered to be diffuse by different authors (e.g., Dopita et al. 1996, Monreal-Ibero et al. 2010). However, it presents a clear filamentary structure and a velocity distribution not following the general rotational pattern of the galaxy. Recently proposed red geysers most probably are ionized by this kind of process (Kehrig et al. 2012, Cheung et al. 2016).

Other sources of ionization, like supernova remnants or planetary nebulae, are in general not resolved at kiloparsec scales, and they are sources of contamination that may complicate classification even more. Furthermore, in many cases it is not easy to clearly define which kind of region is observed when different types are on the same aperture/line of sight. For a recent review on the properties of the ISM and how to recover them from emission lines, I refer readers to Kewley et al. (2019).

APPENDIX C. LIST OF ACRONYMS AND DEFINITIONS

Table 2 presents a list acronyms, symbols, and definitions used in this review.

Table 2 Acronyms used in this review

AAT	Anglo-Australian Telescope
AGB	Asymptotic giant branch
[α/Fe]	Relative abundance of α elements over Fe
AMRs	Anomalous metallicities regions
ALMaQUEST	ALMA-MaNGA QUEnching and STar formation survey
AMUSING	All-weather MUse Supernova Integral field Nearby Galaxies survey
ATLAS^{3D}	IFS survey of elliptical galaxies in the nearby Universe
BPT	Baldwin–Phillips–Terlevich
CALIFA	Calar Alto Legacy Integral Field spectroscopy Area survey
ChEH	Chemical-enrichment history
CMD	Color–magnitude diagram
D4000	Stellar index that compares the flux before and after 4000 Å
DR	Data release
EDGE	Extragalactic Database for Galaxy Evolution survey
EDGE-CALIFA	Combination of the EDGE CO data with the CALIFA data
EW	Equivalent width
FMR	Fundamental metallicity relation
FoV	Field of view
FWHM	Full width at half maximum
GAMA	Galaxy and Mass Assembly survey
GASP	GAs Stripping Phenomena in galaxies with MUSE
GV	Green valley
GVG	Green valley galaxy
IMF	Initial mass function
LINERs	Low-ionization nuclear emission-line regions
`LZIFU`	Emission-line analysis pipeline for IFS-GS data (used mostly in SAMI data)
MAD	MUSE Atlas of Disks
MaNGA	Mapping Nearby Galaxies at Apache Point Observatory survey
`MaNGA DAP`	MaNGA data analysis pipeline
MZR	Mass–metallicity relation
$M_{\rm gas}$	Cold gas mass
M_*	Stellar mass
$M_\odot$	Solar mass
PHANGS	Physics at High Angular resolution in Nearby GalaxieS survey
`Pipe3D`	Pipeline for the analysis of emission lines and stellar populations for IFS-GS data
PINGS	Ppak IFS Nearby Galaxy Survey
PSF	Point spread function
`PyCASSO`	Value-added catalog for CALIFA galaxies analyzed with `STARLIGHT`
rFMR	Resolved fundamental metallicity relation
rMZR	Resolved mass–metallicity relation
rSFH	Resolved star-formation history
rSFMS	Resolved SFMS relation
S/N	Signal-to-noise ratio

(*Continued*)

Table 2 ***(Continued)***

SAMI	Sydney-Australian-Astronomical-Observatory Multi-object Integral-Field Spectrograph survey
SAURON	IFS survey of elliptical galaxies in the nearby Universe
SBP	Surface brightness profile
SDSS	Sloan Digital Sky Survey
SF	Star formation
SFE	Star-formation efficiency (=SFR/M_{gas})
SFH	Star-formation history
SFR	Star-formation rate
SN	Supernova
Σ_{gas}	Cold gas mass surface density
Σ_{SFR}	SFR surface density
Σ_{*}	Stellar mass surface density
sSFR	Specific star-formation rate
SK law	Schmidt–Kennicutt Law
SSP	Single stellar population
τ_{dep}	Depletion time (=M_{gas}/SFR)
TIMER	Time Inference with MUSE in Extragalactic Rings
VENGA	Virus-P Exploration of Nearby Galaxies
[Z/H]	Stellar metallicity normalized to the solar one in logarithmic scale

SUMMARY POINTS

1. Evolution of galaxies is governed by local properties but affected by global ones. Most scaling relations (like the SK law, MZR, and SFMS) have local/resolved counterparts verified at kiloparsec scales from which the global ones are integrated versions.
2. Not all global relations are verified at local scales for all galaxy types and at any stellar masses (e.g., stellar MZR).
3. Local scaling relations (and the lack of them) are a consequence of the narrow range of depletion times and the similarities of the local SFHs at fixed galactocentric distances of galaxies of similar final stellar mass, together with a chemical enrichment dominated by local processes.
4. Radial gradients are a consequence of the local relations and the initial radial distribution of gas following the gravitational potential.
5. Deviations from local relations (and gradients) are either (*a*) associated with dynamical and mixing processes, together with local exchange of gas (inflows, outflows, fountains) or (*b*) described by differences in t_{dep} or the local SFHs among galaxy types.
6. Ionization happens at local scales, driven by different physical processes coexisting in a galaxy, and it cannot be clearly understood using purely integrated quantities.
7. The dominant ionization in a certain location in a galaxy is mostly dictated by the properties of the underlying stellar population (that are connected with those of the ionized gas).

FUTURE ISSUES

1. How do the stellar and ionized gas properties connect with those of the cold gas (atomic and molecular) at kiloparsec scales? We require HI and H2 explorations at similar physical scales of current IFS-GSs on large and statistically significant samples of galaxies already covered by those surveys.
2. At which scales are local relations still verified? What does this tell us about their nature? Are those statistical laws? IFS-GSs should expand to smaller physical scales to explore these issues.
3. IFS-GSs should expand toward larger samples and higher redshifts to constrain even more the evolutionary paths already uncovered by recent surveys (e.g., the Hector survey; Bland-Hawthorn 2015). Covering lower-mass ranges will be also fundamental.
4. We need to improve our methods to recover the SFHs and ChEHs. Spatially resolved spectroscopic information should be complemented with multiwavelength information at similar scales (that would require new UV and far-IR explorers).
5. Data at higher spectral resolution that go deeper and are on wider wavelength ranges are required to use fainter emission lines to obtain precise information on the ionization conditions and the chemical composition of the gas.
6. Which is the real quenching mechanism? Mergers? AGNs? Stabilization? The involved mechanisms, in particular AGN feedback, should be understood in much more detail to understand which observables constrain/define it in a better way.
7. Greater efforts in detailed hydrodynamical and *N*-body simulations at kiloparsec and subkiloparsec scales are required for a better understanding of the local/resolved scaling relations.

DISCLOSURE STATEMENT

The author is not aware of any affiliations, memberships, funding, or financial holdings that might be perceived as affecting the objectivity of this review.

ACKNOWLEDGMENTS

I thank Karen for allowing me to work on this review when I should not have.

I am grateful for comments and corrections on the content of this review from J. Schaye, E. Pérez, L. Sánchez-Menguiano, P. Sánchez-Blazquez, C.J. Walcher, R.C. Kennicutt Jr., A. de Lorenzo-Caceres, J.K. Barrera-Ballesteros, C. Morisset, B. Hussemann, A. Bolatto, R. Cid-Fernandes, E. Lacerda, A. Mejia, and C. López-Cobá. I thank the editor J. Schaye and R. Lowe-Webb for helping me in the production phase.

I thank M.M. Roth and L. Wisotzki for recovering me for astronomy. It is an honor to have such friends. I thank the full Calar Alto Legacy Integral Field Area (CALIFA) collaboration for their incredible work through the years, and in particular D. Mast, B. Husemann, and R. Garcia-Benito. The CALIFA survey was my personal excuse to justify being around an exceptional group of astronomers from whom I learned and developed most of what it is included in this review. I also thank the members of the MaNGA, Sydney–Australian Astronomical Observatory

Multi-object Integral (SAMI), and AMUSING collaborations for allowing me to continue developing new ideas with new amazing data sets with incredible people. I would like to thank the EDGE collaboration and, in particular, A. Bolatto for opening a new branch of opportunities with the inclusion of spatial resolve CO data. Finally, I thank all the Calar Alto Observatory staff, who allowed me to develop professionally and personally. When I am there, I know I am at home.

I am grateful for the support of CONACYT grants CB-285080 and FC-2016-01-1916 and funding from the PAPIIT-DGAPA-IA101217 (UNAM) project.

For this review, I used data from the CALIFA, SAMI, and MaNGA IFS-GS surveys.

This study uses data provided by the CALIFA survey (**http://califa.caha.es/**) based on observations collected at the Centro Astronómico Hispano Alemán (CAHA) at Calar Alto, operated jointly by the Max-Planck-Institut für Astronomie and the Instituto de Astrofísica de Andalucía (CSIC).

The SAMI Galaxy Survey is based on observations made at the Anglo-Australian Telescope. The SAMI field spectrograph was developed jointly by the University of Sydney and the Australian Astronomical Observatory.

The MaNGA survey is part of the Sloan Digital Sky Survey IV (SDSS-IV). Funding for the SDSS-IV has been provided by the Alfred P. Sloan Foundation, the US Department of Energy Office of Science, and the Participating Institutions. SDSS-IV acknowledges support and resources from the Center for High-Performance Computing at the University of Utah. The SDSS web site is **www.sdss.org**.

I also use data from the MUSE instrument installed at the European Space Observatory's Very Large Telescope facility.

LITERATURE CITED

Abdurro'uf, Akiyama M. 2017. *MNRAS* 469:2806–20
Aguado DS, Ahumada R, Almeida A, et al. 2019. *Ap. J. Suppl.* 240:23
Alatalo K, Davis TA, Bureau M, et al. 2013. *MNRAS* 432:1796–844
Asari NV, Cid Fernandes R, Stasińska G, et al. 2007. *MNRAS* 381:263–79
Athanassoula E. 1992. *MNRAS* 259:345–64
Bacon R, Accardo M, Adjali L, et al. 2010. *Proc. SPIE Conf. Ser.* 7735:7735O8
Bacon R, Copin Y, Monnet G, et al. 2001. *MNRAS* 326:23–35
Bacon E, Monnet G. 2017. *Optical 3D-Spectroscopy for Astronomy*. Weinheim, Ger.: Wiley-VCH Verlag
Bakos J, Trujillo I, Pohlen M. 2008. *Ap. J. Lett.* 683:L103–6
Baldwin JA, Phillips MM, Terlevich R. 1981. *Publ. Astron. Soc. Pac.* 93:5–19
Bamford SP, Nichol RC, Baldry IK, et al. 2009. *MNRAS* 393:1324–52
Barden M, Rix HW, Somerville RS, et al. 2005. *Ap. J.* 635:959–81
Barrera-Ballesteros JK, Heckman T, Sánchez SF, et al. 2018. *Ap. J.* 852:74
Barrera-Ballesteros JK, Heckman TM, Zhu GB, et al. 2016. *MNRAS* 463:2513–22
Barrera-Ballesteros JK, Sánchez SF, Heckman T, Blanc GA, The MaNGA Team. 2017. *Ap. J.* 844:80
Barrera-Ballesteros JK, Utomo D, Bolatto AD, et al. 2020. *MNRAS* 492:2651–62
Belfiore F, Maiolino R, Bothwell M. 2016. *MNRAS* 455:1218–36
Belfiore F, Maiolino R, Bundy K, et al. 2018. *MNRAS* 477:3014–29
Belfiore F, Maiolino R, Maraston C, et al. 2017a. *MNRAS* 466:2570–89
Belfiore F, Maiolino R, Tremonti C, et al. 2017b. *MNRAS* 469:151–70
Belfiore F, Vincenzo F, Maiolino WR, Matteucci F. 2019a. *MNRAS* 487:456–74
Belfiore F, Westfall KB, Schaefer A, et al. 2019b. *Astron. J.* 158:160
Bell EF. 2008. *Ap. J.* 682:355–60
Bell EF, de Jong RS. 2001. *Ap. J.* 550:212–29
Bell EF, McIntosh DH, Barden M, et al. 2004. *Ap. J. Lett.* 600:L11–14

Bell EF, McIntosh DH, Katz N, Weinberg MD. 2003. *Ap. J. Suppl.* 149:289–312
Bell EF, Phleps S, Somerville RS, et al. 2006. *Ap. J.* 652:270–76
Belley J, Roy JR. 1992. *Ap. J. Suppl.* 78:61–85
Belli S, Genzel R, Förster Schreiber NM, et al. 2017. *Ap. J. Lett.* 841:L6
Bershady MA. 2009. arXiv:0910.0167
Bershady MA, Verheijen MAW, Swaters RA, et al. 2010. *Ap. J.* 716:198–233
Bigiel F, Leroy A, Walter F, et al. 2008. *Astron. J.* 136:2846–71
Binette L, Magris CG, Stasińska G, Bruzual AG. 1994. *Astron. Astrophys.* 292:13–19
Bird J, Martini P, Kaiser C. 2008. *Ap. J.* 676:147–62
Bitsakis T, Dultzin D, Ciesla L, et al. 2016. *MNRAS* 459:957–70
Blanc GA, Gebhardt K, Heiderman A, et al. 2010. In *New Horizons in Astronomy: Frank N. Bash Symposium 2009*, ed. LM Stanford, JD Green, L Hao, Y Mao, Vol. 432, *Astron. Soc. Pac. Conf. Ser.*, pp. 180–86. San Francisco: ASP
Blanc GA, Lu Y, Benson A, Katsianis A, Barraza M. 2019. *Ap. J.* 877:6
Bland-Hawthorn J. 1995. *Publ. Astron. Soc. Aust.* 12:190–96
Bland-Hawthorn J. 2015. In *Galaxies in 3D Across the Universe*, *Proc. IAU Symp. 309*, ed. BL Ziegler, F Combes, H Dannerbauer, M Verdugo, pp. 21–28. Cambridge, UK: Cambridge Univ. Press
Blanton MR, Hogg DW, Bahcall NA, et al. 2003. *Ap. J.* 592:819–38
Blanton MR, Moustakas J. 2009. *Annu. Rev. Astron. Astrophys.* 47:159–210
Bluck AFL, Maiolino R, Sánchez SF, et al. 2020. MNRAS 492:96–139
Boissier S, Prantzos N. 1999. *MNRAS* 307:857–76
Bolatto AD, Leroy AK, Rosolowsky E, Walter F, Blitz L. 2008. *Ap. J.* 686:948–65
Bolatto AD, Wolfire M, Leroy AK. 2013. *Annu. Rev. Astron. Astrophys.* 51:207–68
Bolatto AD, Wong T, Utomo D, et al. 2017. *Ap. J.* 846:159
Bonnell IA, Bate MR, Zinnecker H. 1998. *MNRAS* 298:93–102
Boone F, Baker AJ, Schinnerer E, et al. 2007. *Astron. Astrophys.* 471:113–25
Bresolin F. 2017. In *Outskirts of Galaxies*, Vol. 434, *Ap. Space Sci. Libr.* ed. JH Knapen, JC Lee, A Gil de Paz, pp. 145–73. Cham, Switz.: Springer Nature
Bresolin F. 2019. *MNRAS* 488:3826–43
Bresolin F, Kennicutt RC Jr. 2015. *MNRAS* 454:3664–73
Brinchmann J, Charlot S, White SDM, et al. 2004. *MNRAS* 351:1151–79
Bundy K, Bershady MA, Law DR, et al. 2015. *Ap. J.* 798:7
Calette AR, Avila-Reese V, Rodríguez-Puebla A, Hernández-Toledo H, Papastergis E. 2018. *Rev. Mex. Astron. Astrophys.* 54:443–83
Cano-Díaz M, Ávila-Reese V, Sánchez SF, et al. 2019. *MNRAS* 488:3929–48
Cano-Díaz M, Sánchez SF, Zibetti S, et al. 2016. *Ap. J. Lett.* 821:L26
Cappellari M. 2016. *Annu. Rev. Astron. Astrophys.* 54:597–665
Cappellari M, Emsellem E, Krajnović D, et al. 2011. *MNRAS* 413:813–36
Carigi L, Peimbert M, Peimbert A. 2019. *Ap. J.* 873:107
Casado J, Ascasibar Y, Gavilán M, et al. 2015. *MNRAS* 451:888–903
Catalán-Torrecilla C, Gil de Paz A, Castillo-Morales A, et al. 2015. *Astron. Astrophys.* 584:A87
Cheung E, Bundy K, Cappellari M, et al. 2016. *Nature* 533:504–8
Cid Fernandes R, González Delgado RM, García Benito R, et al. 2014. *Astron. Astrophys.* 561:A130
Cid Fernandes R, Mateus A, Sodré L, Stasinska G, Gomes JM. 2011. Astrophysics Source Code Library. ascl:1108.006
Cid Fernandes R, Pérez E, García Benito R, et al. 2013. *Astron. Astrophys.* 557:A86
Cid Fernandes R, Stasińska G, Schlickmann MS, et al. 2010. *MNRAS* 403:1036–53
Coccato L, Gerhard O, Arnaboldi M. 2010. *MNRAS* 407:L26–30
Colombo D, Kalinova V, Utomo D, et al. 2018. *MNRAS* 475:1791–808
Comte G. 1975. *Astron. Astrophys.* 39:197–205
Conroy C. 2013. *Annu. Rev. Astron. Astrophys.* 51:393–455
Courteau S, Cappellari M, de Jong RS, et al. 2014. *Rev. Mod. Phys.* 86:47–119

Courteau S, de Jong RS, Broeils AH. 1996. *Ap. J. Lett.* 457:L73–76
Cresci G, Mannucci F, Curti M. 2019. *Astron. Astrophys.* 627:A42
Croom SM, Lawrence JS, Bland-Hawthorn J, et al. 2012. *MNRAS* 421:872–93
Croton DJ, Springel V, White SDM, et al. 2006. *MNRAS* 365:11–28
Curti M, Mannucci F, Cresci G, Maiolino R. 2019. *MNRAS* 491:944–64
Daddi E, Dickinson M, Morrison G, et al. 2007. *Ap. J.* 670:156–72
Daddi E, Elbaz D, Walter F, et al. 2010. *Ap. J. Lett.* 714:L118–22
Davé R, Finlator K, Oppenheimer BD. 2011. *MNRAS* 416:1354–76
Davies RL, Kewley LJ, Ho IT, Dopita MA. 2014. *MNRAS* 444:3961–74
Davis TA, Alatalo K, Bureau M, et al. 2013. *MNRAS* 429:534–55
de Amorim AL, García-Benito R, Cid Fernandes R, et al. 2017. *MNRAS* 471:3727–52
de La Rosa IG, La Barbera F, Ferreras I, de Carvalho RR. 2011. *MNRAS* 418:L74–78
de los Reyes MAC, Kennicutt RC Jr. 2019. *Ap. J.* 872:16
de Vaucouleurs G. 1959. In *Astrophysik IV: Sternsysteme. Handbuch der Physik*. 11:311–72. Berlin, Heidelberg: Springer
de Zeeuw PT, Bureau M, Emsellem E, et al. 2002. *MNRAS* 329:513–30
Dey B, Rosolowsky E, Cao Y, et al. 2019. *MNRAS* 488:1926–40
Di Matteo P, Haywood M, Combes F, Semelin B, Snaith ON. 2013. *Astron. Astrophys.* 553:A102
Diaz AI. 1989. In *Evolutionary Phenomena in Galaxies*, ed. JE Beckman, BEJ Pagel, pp. 377–97. Cambridge, UK: Cambridge Univ. Press
Dopita MA, Koratkar AP, Evans IN, et al. 1996. In *The Physics of LINERS in View of Recent Observations*, ed. M Eracleous, A Koratkar, C Leitherer, L Ho, *ASP Conf. Ser*. 103:44–55. San Francisco: ASP
Driver SP, Andrews SK, da Cunha E, et al. 2018. *MNRAS* 475:2891–35
Driver SP, Norberg P, Baldry IK, et al. 2009. *Astron. Geophys.* 50:5.12–19
Drory N, Fisher DB. 2007. *Ap. J.* 664:640–49
Elbaz D, Daddi E, Le Borgne D, et al. 2007. *Astron. Astrophys.* 468:33–48
Ellison SL, Patton DR, Simard L, McConnachie AW. 2008. *Ap. J. Lett.* 672:L107–10
Ellison SL, Sánchez SF, Ibarra-Medel H, et al. 2018. *MNRAS* 474:2039–54
Ellison SL, Thorp MD, Lin L, et al. 2020. *MNRAS* 493:L39–43
Elmegreen BG. 1997. In *1st Guillermo Haro Conference on Astrophysics: Starburst Activity in Galaxies, Puebla, Pue., Mexico, Apr. 29–May 3, 1996*, Vol. 6, *Rev. Mex. Astron. Astrophys. Conf. Ser.*, ed. J Franco, R Terlevich, A Serrano, pp. 165–71. Mexico City, Mex.: Univ. Nac. Auton. Mex.
Elmegreen DM, Elmegreen BG, Ravindranath S, Coe DA. 2007. *Ap. J.* 658:763–77
Emsellem E, Cappellari M, Peletier RF, et al. 2004. *MNRAS* 352:721–43
Erb DK. 2008. *Ap. J.* 674:151–56
Erb DK, Shapley AE, Pettini M, et al. 2006. *Ap. J.* 644:813–28
Erroz-Ferrer S, Carollo CM, den Brok M, et al. 2019. *MNRAS* 484:5009–27
Esteban C, García-Rojas J. 2018. *MNRAS* 478:2315–36
Evans IN, Dopita MA. 1985. *Ap. J. Suppl.* 58:125–42
Faber S. 1977. In *The Evolution of Galaxies and Stellar Populations*, ed. BM Tinsley, RB Larson, pp. 157, New Haven, CT: Yale Univ. Obs.
Faber SM, Willmer CNA, Wolf C, et al. 2007. *Ap. J.* 665:265–94
Fabian AC. 2012. *Annu. Rev. Astron. Astrophys.* 50:455–89
Flores-Fajardo N, Morisset C, Stasińska G, Binette L. 2011. *MNRAS* 415:2182–92
Freeman KC. 1970. *Ap. J.* 160:811–30
Gadotti DA, Sánchez-Blázquez P, Falcón-Barroso J, et al. 2019. *MNRAS* 482:506–29
Galbany L, Anderson JP, Rosales-Ortega FF, et al. 2016. *MNRAS* 455:4087–99
Galbany L, Collett TE, Méndez-Abreu J, et al. 2018. *MNRAS* 479:262–74
Galbany L, Mora L, González-Gaitán S, et al. 2017. *MNRAS* 468:628–44
Gallazzi A, Brinchmann J, Charlot S, White SDM. 2008. *MNRAS* 383:1439–58
Gallazzi A, Charlot S, Brinchmann J, White SDM, Tremonti CA. 2005. *MNRAS* 362:41–58
Ganda K, Falcón-Barroso J, Peletier RF, et al. 2006. *MNRAS* 367:46–78

García-Benito R, González Delgado RM, Pérez E, et al. 2017. *Astron. Astrophys.* 608:A27
García-Benito R, González Delgado RM, Pérez E, et al. 2019. *Astron. Astrophys.* 621:A120
García-Lorenzo B, Mediavilla E, Arribas S, del Burgo C. 1997. *Ap. J.* 483:L99–102
Garnett DR. 2002. *Ap. J.* 581:1019–31
Gavazzi G, Consolandi G, Dotti M, et al. 2015. *Astron. Astrophys.* 580:A116
Genzel R, Tacconi LJ, Gracia-Carpio J, et al. 2010. *MNRAS* 407:2091–108
Goddard D, Thomas D, Maraston C, et al. 2017. *MNRAS* 466:4731–58
Gomes JM, Papaderos P, Kehrig C, et al. 2016a. *Astron. Astrophys.* 588:A68
Gomes JM, Papaderos P, Vílchez JM, et al. 2016b. *Astron. Astrophys.* 585:A92
González Delgado RM, Cid Fernandes R, García-Benito R, et al. 2014a. *Ap. J. Lett.* 791:L16
González Delgado RM, Cid Fernandes R, Pérez E, et al. 2016. *Astron. Astrophys.* 590:A44
González Delgado RM, García-Benito R, Pérez E, et al. 2015. *Astron. Astrophys.* 581:A103
González Delgado RM, Pérez E, Cid Fernandes R, et al. 2014b. *Astron. Astrophys.* 562:A47
González Delgado RM, Pérez E, Cid Fernandes R, et al. 2017. *Astron. Astrophys.* 607:A128
González JJ. 1994. *Line-strength gradients and kinematic profiles in elliptical galaxies*. PhD Thesis, Univ. Calif., Santa Cruz
Graham MT, Cappellari M, Li H, et al. 2018. *MNRAS* 477:4711–37
Grand RJJ, Springel V, Kawata D, et al. 2016. *MNRAS* 460:L94–98
Hall C, Courteau S, Jarrett T, et al. 2018. *Ap. J.* 865:154
Heavens A, Panter B, Jimenez R, Dunlop J. 2004. *Nature* 428:625–27
Heckman TM, Armus L, Miley GK. 1990. *Ap. J. Suppl.* 74:833–68
Henriques BMB, White SDM, Lilly SJ, et al. 2019. *MNRAS* 485:3446–56
Henry A, Scarlata C, Domínguez A, et al. 2013. *Ap. J. Lett.* 776:L27
Ho IT, Kewley LJ, Dopita MA, et al. 2014. *MNRAS* 444:3894–910
Ho IT, Medling AM, Groves B, et al. 2016. *Ap. Space Sci.* 361:280
Ho IT, Meidt SE, Kudritzki RP, et al. 2018. *Astron. Astrophys.* 618:A64
Ho IT, Seibert M, Meidt SE, et al. 2017. *Ap. J.* 846:39
Hopkins PF, Cox TJ, Younger JD, Hernquist L. 2009. *Ap. J.* 691:1168–201
Hsieh BC, Lin L, Lin JH, et al. 2017. *Ap. J. Lett.* 851:L24
Hubble E. 1936. *Ap. J.* 84:517–54
Hubble EP. 1926. *Ap. J.* 63:236–74
Hughes A, Wong T, Ott J, et al. 2010. *MNRAS* 406:2065–86
Husemann B, Jahnke K, Sánchez SF, et al. 2014. *MNRAS* 443:755–83
Husemann B, Sánchez SF, Wisotzki L, et al. 2010. *Astron. Astrophys.* 519:A115
Husemann B, Wisotzki L, Jahnke K, Sánchez SF. 2011. *Astron. Astrophys.* 535:A72
Hwang HC, Barrera-Ballesteros JK, Heckman TM, et al. 2019. *Ap. J.* 872:144
Ibarra-Medel HJ, Avila-Reese V, Sánchez SF, González-Samaniego A, Rodríguez-Puebla A. 2019. *MNRAS* 483:4525–50
Ibarra-Medel HJ, Sánchez SF, Avila-Reese V, et al. 2016. *MNRAS* 463:2799–818
Jarvis BJ. 1990. *Astron. Astrophys.* 240:L8–10
Jogee S, Scoville N, Kenney JDP. 2005. *Ap. J.* 630:837–63
Kauffmann G, Heckman TM, Tremonti C, et al. 2003. *MNRAS* 346:1055–77
Kehrig C, Monreal-Ibero A, Papaderos P, et al. 2012. *Astron. Astrophys.* 540:A11
Kennicutt RC Jr. 1998a. *Annu. Rev. Astron. Astrophys.* 36:189–232
Kennicutt RC Jr. 1998b. *Ap. J.* 498:541–52
Kennicutt RC Jr., Calzetti D, Walter F, et al. 2007. *Ap. J.* 671:333–48
Kennicutt RC Jr., Evans NJ. 2012. *Annu. Rev. Astron. Astrophys.* 50:531–608
Kennicutt RC Jr., Keel WC, Blaha CA. 1989. *Astron. J.* 97:1022–35
Kewley LJ, Dopita MA, Sutherland RS, Heisler CA, Trevena J. 2001. *Ap. J.* 556:121–40
Kewley LJ, Ellison SL. 2008. *Ap. J.* 681:1183–204
Kewley LJ, Nicholls DC, Sutherland RS. 2019. *Annu. Rev. Astron. Astrophys.* 57:511–70
Knapen JH, Comerón S, Seidel MK. 2019. *Astron. Astrophys.* 621:L5

Koleva M, Prugniel P, De Rijcke S, Zeilinger WW. 2011. *MNRAS* 417:1643–71
Kormendy J, Ho LC. 2013. *Annu. Rev. Astron. Astrophys.* 51:511–653
Kreckel K, Groves B, Bigiel F, et al. 2017. *Ap. J.* 834:174
Kruijssen JMD, Longmore SN. 2014. *MNRAS* 439:3239–52
Kruijssen JMD, Schruba A, Chevance M, et al. 2019. *Nature* 569:519–22
Krumholz MR, Dekel A, McKee CF. 2012. *Ap. J.* 745:69
Kuntschner H. 2015. In *Galaxy Masses as Constraints of Formation Models*, *IAU Symp. 311*, ed. M Cappellari, S Courteau, pp. 53–56. Cambridge, UK: Cambridge Univ. Press
Kuntschner H, Emsellem E, Bacon R, et al. 2010. *MNRAS* 408:97–132
Lacerda EAD, Cid Fernandes R, Couto GS, et al. 2018. *MNRAS* 474:3727–39
Lacerda EAD, Sánchez SF, Fernandes RC, et al. 2020. *MNRAS* 492:3073–90
Lara-López MA, Cepa J, Bongiovanni A, et al. 2010. *Astron. Astrophys.* 521:L53
Leroy AK, Walter F, Brinks E, et al. 2008. *Astron. J.* 136:2782–845
Leroy AK, Walter F, Sandstrom K, et al. 2013. *Astron. J.* 146:19
Li C, Wang E, Lin L, et al. 2015. *Ap. J.* 804:125
Li Y, Bresolin F, Kennicutt RC Jr. 2013. *Ap. J.* 766:17
Lilly SJ, Carollo CM, Pipino A, Renzini A, Peng Y. 2013. *Ap. J.* 772:119
Lin L, Belfiore F, Pan HA, et al. 2017. *Ap. J.* 851:18
Lin L, Pan HA, Ellison SL, et al. 2019. *Ap. J. Lett.* 884:L33
López-Cobá C, Sánchez SF, Anderson J, et al. 2020. *Astron. J.* 159:167
López-Cobá C, Sánchez SF, Bland-Hawthorn J, et al. 2019. *MNRAS* 482:4032–56
López-Cobá C, Sánchez SF, Cruz-González I, et al. 2017a. *Ap. J. Lett.* 850:L17
López-Cobá C, Sánchez SF, Moiseev AV, et al. 2017b. *MNRAS* 467:4951–64
López Fernández R, Cid Fernandes R, González Delgado RM, et al. 2016. *MNRAS* 458:184–99
López Fernández R, González Delgado RM, Pérez E, et al. 2018. *Astron. Astrophys.* 615:A27
Madau P, Dickinson M. 2014. *Annu. Rev. Astron. Astrophys.* 52:415–86
Madau P, Pozzetti L, Dickinson M. 1998. *Ap. J.* 498:106–16
Magorrian J, Tremaine S, Richstone D, et al. 1998. *Astron. J.* 115:2285–305
Maiolino R, Mannucci F. 2019. *Astron. Astrophys. Rev.* 27:3
Maiolino R, Nagao T, Grazian A, et al. 2008. *Astron. Astrophys.* 488:463–79
Mannucci F, Cresci G, Maiolino R, Marconi A, Gnerucci A. 2010. *MNRAS* 408:2115–27
Maragkoudakis A, Zezas A, Ashby MLN, Willner SP. 2017. *MNRAS* 466:1192–204
Marino RA, Gil de Paz A, Sánchez SF, et al. 2016. *Astron. Astrophys.* 585:A47
Marino RA, Rosales-Ortega FF, Sánchez SF, et al. 2013. *Astron. Astrophys.* 559:A114
Mármol-Queraltó E, Sánchez SF, Marino RA, et al. 2011. *Astron. Astrophys.* 534:A8
Martig M, Bournaud F, Teyssier R, Dekel A. 2009. *Ap. J.* 707:250–67
Martin P, Roy JR. 1994. *Ap. J.* 424:599–614
Matteucci F, Francois P. 1989. *MNRAS* 239:885–904
McDermid RM, Alatalo K, Blitz L, et al. 2015. *MNRAS* 448:3484–513
McIntosh DH, Wagner C, Cooper A, et al. 2014. *MNRAS* 442:533–57
McWilliam A. 1997. *Annu. Rev. Astron. Astrophys.* 35:503–56
Medling AM, Cortese L, Croom SM, et al. 2018. *MNRAS* 475:5194–214
Mehlert D, Thomas D, Saglia RP, Bender R, Wegner G. 2003. *Astron. Astrophys.* 407:423–35
Méndez-Abreu J, Ruiz-Lara T, Sánchez-Menguiano L, et al. 2017. *Astron. Astrophys.* 598:A32
Méndez-Abreu J, Sánchez SF, de Lorenzo-Cáceres A. 2019. *MNRAS* 488:L80–84
Minchev I, Famaey B, Quillen AC, et al. 2012. *Astron. Astrophys.* 548:A126
Mollá M, Díaz AI. 2005. *MNRAS* 358:521–43
Monreal-Ibero A, Vílchez JM, Walsh JR, Muñoz-Tuñón C. 2010. *Astron. Astrophys.* 517:A27
Moran SM, Heckman TM, Kauffmann G, et al. 2012. *Ap. J.* 745:66
Morisset C, Delgado-Inglada G, Sánchez SF, et al. 2016. *Astron. Astrophys.* 594:A37
Moustakas J, Kennicutt RC Jr. 2006. *Ap. J.* 651:155–66
Noeske KG, Faber SM, Weiner BJ, et al. 2007. *Ap. J. Lett.* 660:L47–50

Osterbrock DE. 1989. *Astrophysics of Gaseous Nebulae and Active Galactic Nuclei*. Mill Valley, CA: Univ. Sci. Books
Oyarzún GA, Bundy K, Westfall KB, et al. 2019. *Ap. J.* 880:111
Pagel BEJ, Edmunds MG. 1981. *Annu. Rev. Astron. Astrophys.* 19:77–113
Pagel BEJ, Patchett BE. 1975. *MNRAS* 172:13–40
Pan HA, Lin L, Hsieh BC, et al. 2018. *Ap. J.* 854:159
Panter B, Heavens AF, Jimenez R. 2003. *MNRAS* 343:1145–54
Panter B, Jimenez R, Heavens AF, Charlot S. 2007. *MNRAS* 378:1550–64
Panter B, Jimenez R, Heavens AF, Charlot S. 2008. *MNRAS* 391:1117–26
Papaderos P, Gomes JM, Vílchez JM, et al. 2013. *Astron. Astrophys.* 555:L1
Peimbert M, Luridiana V, Peimbert A. 2007. *Ap. J.* 666:636–46
Peimbert M, Torres-Peimbert S, Rayo JF. 1978. *Ap. J.* 220:516–24
Peletier RF. 1989. *Elliptical galaxies: structure and stellar content*. PhD Thesis, Univ. Gröningen, The Netherlands
Peletier RF, Davies RL, Illingworth GD, Davis LE, Cawson M. 1990. *Astron. J.* 100:1091–142
Peng Y, Lilly SJ, Kovac K, et al. 2010. *Ap. J.* 721:193–221
Pérez E, Cid Fernandes R, González Delgado RM, et al. 2013. *Ap. J. Lett.* 764:L1
Pérez-González PG, Rieke GH, Villar V, et al. 2008. *Ap. J.* 675:234–61
Pérez-Montero E. 2014. *MNRAS* 441:2663–75
Pérez-Montero E. 2017. *Publ. Astron. Soc. Pac.* 129:043001
Peterken TG, Merrifield MR, Aragón-Salamanca A, et al. 2018. *Nat. Astron.* 3:178–82
Pettini M, Pagel BEJ. 2004. *MNRAS* 348:L59–63
Pilyugin LS, Grebel EK, Kniazev AY. 2014. *Astron. J.* 147:131
Pilyugin LS, Thuan TX, Vílchez JM. 2007. *MNRAS* 376:353–60
Poetrodjojo H, Groves B, Kewley LJ, et al. 2018. *MNRAS* 479:5235–65
Poggianti BM, Moretti A, Gullieuszik M, et al. 2017. *Ap. J.* 844:48
Pozzetti L, Bolzonella M, Zucca E, et al. 2010. *Astron. Astrophys.* 523:A13
Rahman N, Bolatto AD, Xue R, et al. 2012. *Ap. J.* 745:183
Rawle TD, Smith RJ, Lucey JR. 2010. *MNRAS* 401:852–66
Rawle TD, Smith RJ, Lucey JR, Swinbank AM. 2008. *MNRAS* 389:1891–904
Regan MW, Thornley MD, Helfer TT, et al. 2001. *Ap. J.* 561:218–37
Renzini A, Peng Y. 2015. *Ap. J. Lett.* 801:L29
Rodríguez-Puebla A, Primack JR, Behroozi P, Faber SM. 2016. *MNRAS* 455:2592–606
Rosales-Ortega FF, Díaz AI, Kennicutt RC Jr., Sánchez SF. 2011. *MNRAS* 415:2439–74
Rosales-Ortega FF, Kennicutt RC Jr., Sánchez SF, et al. 2010. *MNRAS* 405:735–58
Rosales-Ortega FF, Sánchez SF, Iglesias-Páramo J, et al. 2012. *Ap. J. Lett.* 756:L31
Rosolowsky E, Schinnerer E, Leroy A, et al. 2019. In *Am. Astron. Soc. Meet. #233* (Abstr. id. 450.01)
Roth MM. 2006. *New Astron. Rev.* 50:252–58
Roy JR, Walsh JR. 1997. *MNRAS* 288:715–25
Roy N, Bundy K, Cheung E, et al. 2018. *Ap. J.* 869:117
Ruiz-Lara T, Pérez I, Florido E, et al. 2016. *MNRAS* 456:L35–39
Ruiz-Lara T, Pérez I, Florido E, et al. 2017. *Astron. Astrophys.* 604:A4
Ryder SD. 1995. *Ap. J.* 444:610–31
Saintonge A, Catinella B, Cortese L, et al. 2016. *MNRAS* 462:1749–56
Saintonge A, Catinella B, Tacconi LJ, et al. 2017. *Ap. J. Suppl.* 233:22
Saintonge A, Kauffmann G, Kramer C, et al. 2011. *MNRAS* 415:32–60
Salim S, Lee JC, Davé R, Dickinson M. 2015. *Ap. J.* 808:25
Salim S, Lee JC, Ly C, et al. 2014. *Ap. J.* 797:126
Salpeter EE. 1955. *Ap. J.* 121:161–67
Sánchez SF. 2015. In *Galaxies in 3D Across the Universe*, *Proc. IAU Symp. 309*, ed. BL Ziegler, F Combes, H Dannerbauer, M Verdugo, pp. 85–92. Cambridge, UK: Cambridge Univ. Press
Sánchez SF, Avila-Reese V, Hernandez-Toledo H, et al. 2018. *Rev. Mex. Astron. Astrophys.* 54:217–60
Sánchez SF, Avila-Reese V, Rodríguez-Puebla A, et al. 2019a. *MNRAS* 482:1557–86

Sánchez SF, Barrera-Ballesteros JK, López-Cobá C, et al. 2019b. *MNRAS* 484:3042–70
Sánchez SF, Barrera-Ballesteros JK, Sánchez-Menguiano L, et al. 2017. *MNRAS* 469:2121–40
Sánchez SF, Galbany L, Pérez E, et al. 2015a. *Astron. Astrophys.* 573:A105
Sánchez SF, Jahnke K, Wisotzki L, et al. 2004. *Ap. J.* 614:586–606
Sánchez SF, Kennicutt RC Jr., Gil de Paz A, et al. 2012a. *Astron. Astrophys.* 538:A8
Sánchez SF, Pérez E, Rosales-Ortega FF, et al. 2015b. *Astron. Astrophys.* 574:A47
Sánchez SF, Pérez E, Sánchez-Blázquez P, et al. 2016a. *Rev. Mex. Astron. Astrophys.* 52:171–220
Sánchez SF, Pérez E, Sánchez-Blázquez P, et al. 2016b. *Rev. Mex. Astron. Astrophys.* 52:21–53
Sánchez SF, Rosales-Ortega FF, Iglesias-Páramo J, et al. 2014. *Astron. Astrophys.* 563:A49
Sánchez SF, Rosales-Ortega FF, Jungwiert B, et al. 2013. *Astron. Astrophys.* 554:A58
Sánchez SF, Rosales-Ortega FF, Marino RA, et al. 2012b. *Astron. Astrophys.* 546:A2
Sánchez SF, Sánchez-Menguiano L. 2017. In *LARIM 2016: XV Latin American Regional IAU Meeting, Cartagena de Indias, Columbia, October 3–7, 2016*, Vol. 49, *Rev. Mex. Astron. Astrophys. Conf. Ser.*, ed. MAH Garzón, SV Domínguez, pp. 28–32. Mexico City, Mex.: Univ. Nac. Auton. Mex.
Sánchez Almeida J, Elmegreen BG, Muñoz-Tuñón C, Elmegreen DM. 2014. *Astron. Astrophys. Rev.* 22:71
Sánchez Almeida J, Sánchez-Menguiano L. 2019. *Ap. J. Lett.* 878:L6
Sánchez-Blázquez P, Forbes DA, Strader J, Brodie J, Proctor R. 2007. *MNRAS* 377:759–86
Sánchez-Blázquez P, Ocvirk P, Gibson BK, Pérez I, Peletier RF. 2011. *MNRAS* 415:709–31
Sánchez-Blázquez P, Rosales-Ortega F, Diaz A, Sánchez SF. 2014a. *MNRAS* 437:1534–48
Sánchez-Blázquez P, Rosales-Ortega FF, Méndez-Abreu J, et al. 2014b. *Astron. Astrophys.* 570:A6
Sánchez-Menguiano L, Sánchez SF, Kawata D, et al. 2016a. *Ap. J. Lett.* 830:L40
Sánchez-Menguiano L, Sánchez SF, Pérez I, et al. 2016b. *Astron. Astrophys.* 587:A70
Sánchez-Menguiano L, Sánchez SF, Pérez I, et al. 2018. *Astron. Astrophys.* 609:A119
Sánchez-Menguiano L, Sánchez Almeida J, Muñoz-Tuñón C, et al. 2019. *Ap. J.* 882:9
Sanders DB, Mirabel IF. 1996. *Annu. Rev. Astron. Astrophys.* 34:749–92
Sarzi M, Falcón-Barroso J, Davies RL, et al. 2006. *MNRAS* 366:1151–200
Sarzi M, Shields JC, Schawinski K, et al. 2010. *MNRAS* 402:2187–210
Schawinski K, Urry CM, Simmons BD, et al. 2014. *MNRAS* 440:889–907
Schawinski K, Urry CM, Virani S, et al. 2010. *Ap. J.* 711:284–302
Schiminovich D, Wyder TK, Martin DC, et al. 2007. *Ap. J. Suppl.* 173:315–41
Schmidt M. 1959. *Ap. J.* 129:243–58
Schruba A, Kruijssen JMD, Leroy AK. 2019. *Ap. J.* 883:2
Schruba A, Leroy AK, Walter F, et al. 2011. *Astron. J.* 142:37
Searle L. 1971. *Ap. J.* 168:327–41
Sérsic JL. 1968. *Atlas de Galaxias Australes*. Córdoba, Argent.: Univ. Nac. Córdoba
Sharp RG, Bland-Hawthorn J. 2010. *Ap. J.* 711:818–52
Shlosman I, Frank J, Begelman MC. 1989. *Nature* 338:45–47
Silk J. 1997. *Ap. J.* 481:703–9
Singh R, van de Ven G, Jahnke K, et al. 2013. *Astron. Astrophys.* 558:A43
Speagle JS, Steinhardt CL, Capak PL, Silverman JD. 2014. *Ap. J. Suppl.* 214:15
Spolaor M, Kobayashi C, Forbes DA, Couch WJ, Hau GKT. 2010. *MNRAS* 408:272–92
Stark DV, Bundy KA, Orr ME, et al. 2018. *MNRAS* 474:2323–33
Stasińska G, Vale Asari N, Cid Fernandes R, et al. 2008. *MNRAS* 391:L29–33
Strateva I, Ivezić Ž, Knapp GR, et al. 2001. *Astron. J.* 122:1861–74
Strömgren B. 1939. *Ap. J.* 89:526–47
Thilker DA, Bianchi L, Meurer G, et al. 2007. *Ap. J. Suppl.* 173:538–71
Thomas D, Maraston C, Bender R, Mendes de Oliveira C. 2005. *Ap. J.* 621:673–94
Thomas D, Maraston C, Schawinski K, Sarzi M, Silk J. 2010. *MNRAS* 404:1775–89
Tissera PB, Scannapieco C, Beers TC, Carollo D. 2013. *MNRAS* 432:3391–400
Torres-Papaqui JP, Coziol R, Andernach H, et al. 2012. *Rev. Mex. Astron. Astrophys.* 48:275–91
Tortora C, Napolitano NR, Cardone VF, et al. 2010. *MNRAS* 407:144–62
Trayford JW, Schaye J. 2019. *MNRAS* 485:5715–32

Tremonti CA, Heckman TM, Kauffmann G, et al. 2004. *Ap. J.* 613:898–913
Tumlinson J, Peeples MS, Werk JK. 2017. *Annu. Rev. Astron. Astrophys.* 55:389–432
Utomo D, Bolatto AD, Wong T, et al. 2017. *Ap. J.* 849:26
Vale Asari N, Stasińska G, Cid Fernandes R, et al. 2009. *MNRAS* 396:L71–75
van de Sande J, Lagos CDP, Welker C, et al. 2019. *MNRAS* 484:869–91
van Dokkum PG, Leja J, Nelson EJ, et al. 2013. *Ap. J. Lett.* 771:L35
Vanderriest C, Haddad B, Lemonnier JP. 1987. In *L'Activite dans les Galaxies*, ed. S Collin, pp. 207. Paris: Ed. Phys.
Veilleux S, Cecil G, Bland-Hawthorn J. 2005. *Annu. Rev. Astron. Astrophys.* 43:769–826
Veilleux S, Osterbrock DE. 1987. *Ap. J. Suppl.* 63:295–310
Vila-Costas MB, Edmunds MG. 1992. *MNRAS* 259:121–45
Vilchez JM, Esteban C. 1996. *MNRAS* 280:720–34
Vogt FPA, Pérez E, Dopita MA, Verdes-Montenegro L, Borthakur S. 2017. *Astron. Astrophys.* 601:A61
Vulcani B, Poggianti BM, Moretti A, et al. 2019. *MNRAS* 488:1597–617
Walcher CJ, Wisotzki L, Bekeraité S, et al. 2014. *Astron. Astrophys.* 569:A1
Walcher J, Groves B, Budavári T, Dale D. 2011. *Ap. Space Sci.* 331:1–52
Weinberg DH, Andrews BH, Freudenburg J. 2017. *Ap. J.* 837:183
Wong T, Blitz L. 2002. *Ap. J.* 569:157–83
Worthey G. 1994. *Ap. J. Suppl.* 95:107–49
Wuyts S, Förster Schreiber NM, Nelson EJ, et al. 2013. *Ap. J.* 779:135
Yates RM, Kauffmann G, Guo Q. 2012. *MNRAS* 422:215–31
York DG, Adelman J, Anderson JE Jr., et al. 2000. *Astron. J.* 120:1579–87
Young LM, Bureau M, Davis TA, et al. 2011. *MNRAS* 414:940–67
Zaritsky D, Kennicutt RC Jr., Huchra JP. 1994. *Ap. J.* 420:87–109
Zheng Z, Wang H, Ge J, et al. 2017. *MNRAS* 465:4572–88
Zibetti S, Charlot S, Rix H. 2009. *MNRAS* 400:1181–98
Zibetti S, Gallazzi AR, Ascasibar Y, et al. 2017. *MNRAS* 468:1902–16
Zibetti S, Gallazzi AR, Hirschmann M, et al. 2019. *MNRAS* 491:3562–85
Zinchenko IA, Pilyugin LS, Grebel EK, Sánchez SF, Vílchez JM. 2016. *MNRAS* 462:2715–33